

**EDDY CURRENT METHODOLOGIES FOR RELIABLE DETECTION
AND RAPID IMAGING OF SUB-SURFACE FLAWS
IN STAINLESS STEEL**

By

**ANIL KUMAR SONI
(Enrollment No: ENGG02201104009)**

Indira Gandhi Centre for Atomic Research, Kalpakkam

*A thesis submitted to the
Board of Studies in Engineering Sciences*

*In partial fulfillment of requirements
for the Degree of*

DOCTOR OF PHILOSOPHY

of

HOMI BHABHA NATIONAL INSTITUTE



August, 2016

Homi Bhabha National Institute

Recommendations of the Viva Voce Committee

As members of the Viva Voce Board, we certify that we have read the dissertation prepared by **Anil Kumar Soni** entitled “**Eddy current methodologies for reliable detection and rapid imaging of sub-surface flaws in stainless steel**” and recommend that it may be accepted as fulfilling the dissertation requirement for the Degree of Doctor of Philosophy.

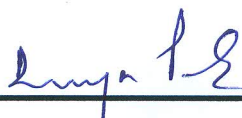
 Chairman- Dr. K. Velusamy	Date: 5/8/2016
 Guide / Convener- Dr. B. Purna Chandra Rao	Date: 5/8/2016
 Co-guide / Member 1- Dr. B.K. Panigrahi	Date: 5/8/16
 Member 2- Dr. M. Sai Baba	Date: 5/8/16
 External Examiner- Dr. V. Rajbabu	

Final approval and acceptance of this dissertation is contingent upon the candidate's submission of the final copies of the dissertation to HBNI.

We hereby certify that we have read this dissertation prepared under our direction and recommend that it may be accepted as fulfilling the dissertation requirement.

Date: 05/08/2016

Place: Kalpakkam



(Dr. B.K. Panigrahi)

Co-Guide



(Dr. B. Purna Chandra Rao)

Guide / Convener

STATEMENT BY GUIDE

I hereby certify that I have read this dissertation prepared under my direction and recommend that it may be accepted as fulfilling the dissertation requirement.

Date: 05/08/2016

Place: Kalpakkam



(Dr. B. Purna Chandra Rao)

Guide / Convener

STATEMENT BY AUTHOR

This dissertation has been submitted in partial fulfillment of requirements for an advanced degree at Homi Bhabha National Institute (HBNI) and is deposited in the library to be made available to borrowers under rules of the HBNI.

Brief quotations from this dissertation are allowable without special permission, provided that accurate acknowledgement of source is made. Requests for permission for extended quotation from or reproduction of this manuscript in whole or in part may be granted by the Competent Authority of HBNI when in his or her judgment the proposed use of the material is in the interests of scholarship. In all other instances, however, permission must be obtained from the author.

Date : 05/08/2016

Place : Kalpakkam



(Anil Kumar Soni)

DECLARATION

I, hereby declare that the investigation presented in the thesis entitled “**Eddy current methodologies for reliable detection and rapid imaging of sub-surface flaws in stainless steel**” submitted to Homi Bhabha National Institute (HBNI), Mumbai, India, for the award of **Doctor of Philosophy in Engineering Sciences**, is the record of work carried out by me under the guidance of **Dr. B. Purna Chandra Rao**, Head, Non-Destructive Evaluation Division, Metallurgy and Materials Group, Indira Gandhi Centre for Atomic Research, Kalpakkam. The work is original and has not been submitted earlier as a whole or in part for a degree / diploma at this or any other Institution/University.

Date : 05/08/2016

Place : Kalpakkam



(Anil Kumar Soni)

LIST OF PUBLICATIONS ARISING FROM THE THESIS

JOURNALS

1. Anil Kumar Soni, S. Thirunavukkarasu and B. Purna Chandra Rao, 'Bayes principle based multi-resolution wavelet transform image processing method for enhancement of sub-surface defect images ', Sensor Review (Under preparation).
2. Anil Kumar. Soni, B. Purna Chandra Rao, S. Mahadevan and S. Thirunavukkarasu, 'A study on the scan plans for rapid eddy current non-destructive evaluation', Journal of Nondestructive Evaluation (Under Review).
3. Anil Kumar Soni, B. Sasi, S. Thirunavukkarasu and B. Purna Chandra Rao 'Development of eddy current probe for detection of deep sub-surface defects', IETE Technical Review, November 2015, DOI: 10.1080/02564602.2015.1113145.
4. Anil Kumar. Soni, S. Thirunavukkarasu, B. Sasi, B. Purna Chandra Rao, T. Jayakumar, 'Development of a high sensitive eddy current instrument for detection of sub-surface defects in stainless steel plates', Insight-Non-Destructive Testing & Condition Monitoring Vol. 57, No. 9, September 2015, pp. 508-512, DOI: 10.1784/insi.2015.57.9.508.
5. S. Thirunavukkarasu, B. Purna Chandra Rao, Anil Kumar Soni, S. Shuaib Ahmed, T. Jayakumar, 'Comparative performance of image fusion methodologies in eddy current testing', Research Journal of Applied Sciences, Engineering and Technology, Vol. 4, No. 24, 2012, pp. 5548-5551.

CONFERENCES

1. Anil Kumar Soni, S Shuaib Ahmed, S. Thirunavukkarasu, B. Purna Chandra Rao and T Jayakumar, 'Multi-Sensor Image Fusion for Enhanced Detection of Sub-Surface Defects by Eddy Current Testing', Presented during the 14th Asia Pacific Conference on Non-destructive Testing, Mumbai, 2013.
2. Anil Kumar Soni, B. Purna Chandra Rao, B. Sasi, Saji Jacob George, T Jayakumar, 'Development of a Low Frequency Eddy Current Instrument for Non-destructive Evaluation', Presented during the National Symposium on Instrumentation (NSI-38), Hubli, 2013.

OTHERS

1. C.S. Angani, Anil Kumar Soni, K. Sambasiva Rao, Jaskaran Singh Grover, S. Thirunavukkarasu, B. Purna Chandra Rao, T. Jayakumar, 'Development of Pulsed Eddy Current System and Model Based Optimization', Presented during the National Seminar on NDE-2012, New Delhi, 2012.

(Anil Kumar Soni)

DEDICATED TO MY BELOVED

PARENTS

ACKNOWLEDGEMENTS

This thesis would not have been possible without the support and encouragement of many people who contributed and extended their valuable co-operation in the completion of the research work. I feel short of words in expressing my appreciation for their help at various stages of this work.

First and foremost, I would like to express my sincere gratitude to my thesis advisor Dr. B. Purna Chandra Rao Head, Non-destructive Evaluation Division (NDED), Indira Gandhi Centre for Atomic Research (IGCAR) for his continuous support to my work, his patience, encouragement, enthusiasm and immense knowledge. His intellectual ideas and guidance helped me in my research work and writing this thesis. He has always been a source of motivation for me in difficult times in research or otherwise. I express my deep sense of appreciation for his support and for energizing me to overcome all the hurdles. I take this opportunity to thank my Co-Guide Dr. B. K. Panigrahi for regular appraisal, kind advice and suggestions to improve the quality of my work.

I thank my doctoral committee; Chairman Dr. K. Velusamy and member Dr. M. Sai Baba for their encouragement, insightful comments and fruitful ideas during the course of the thesis work which have been useful for the progress of my work. I express my sincere gratitude to Dr. T. Jayakumar, former Director, Metallurgy and Materials Group (MMG), IGCAR for the inspiration and encouragement. I extend my heartfelt thanks to the former directors of IGCAR, Shri S. C. Chetal and Dr. P. R. Vasudeva Rao and to the present Director, Dr. S.A.V. Satya Murty for permitting me to pursue research in this reputed centre. I wish to acknowledge Dr. C. K. Mukhopadhyay, Head EMSI Section, NDED, IGCAR, for providing his valuable suggestions at various occasions.

I express my gratitude to Dr. S. Thirunavukkarasu, Smt B. Sasi, and Shri S. Mahadevan, NDED, IGCAR for helping me in learning the instrumentation and experimental techniques and providing me technical support and guidance during the entire research work. I share the credit of my work with them for helping me in carrying out the experiments round the clock and enriching my ideas.

I thank my lab mates Dr. G. K. Sharma, Dr. C. S. Angani, Dr. W. Sharatchandra Singh, Shri S.

Ponseenivasan, Shri V. Arjun, Shri K. Samba Siva Rao, Dr. S. Shuaib Ahmed, Shri K. Arunmuthu, Shri A. Viswanath and other NDED staff members for their timely help, useful technical discussions, suggestions, and moral support.

Apart from the intellectual support, an emotional support is always needed to conquer the hardships. For this, I would like to thank, from the bottom of my heart, my friends Ashutosh Mishra, M. Kalyan Phani, B. Rakesh, K. Siva Srinivas, Chandan Kumar Bhagat, B. K. Srihari, Deepak CH., Arun Babu, Paawan Sharma, M. Bubathi, Sharath D, M. S. K. Chaitanya, G.V.K. Kishore and S. Naveen for their warm friendship.

Last but not the least, my deepest gratitude is to my family for their warm support which brings belief and hope into my life; to my beloved parents Shri Ram Kumar Soni and Smt. Krishna Soni, who have been so caring and supportive of me all the time; to my wife Smt Aradhana Soni, who has been always with me as my strength for up and down moments during my research work; and my grandparents, who have always been a source of inspiration towards achieving the goals in life. Immense love and affection of my sister Radhika Soni and brother Vikas Soni have been invaluable in the journey towards my goal.

Apart from all the people mentioned in this acknowledgment, there are many others who have helped me in various ways during the course of this thesis work. My sincere thanks and apologies to all those I may have forgotten to mention.

(Anil Kumar Soni)

TABLE OF CONTENTS

TABLE OF CONTENTS	i
Abstract	v
List of Figures	vii
List of Tables	xiii
Nomenclature	xv
1 Introduction	1
1.1 NON-DESTRUCTIVE EVALUATION	1
1.2 EDDY CURRENT TESTING	5
1.2.1 Principle of eddy current testing	5
1.2.2 Detection of surface flaws	8
1.2.3 Detection of sub-surface flaws	12
1.3 CONSIDARATIONS FOR DETECTION OF SUB-SURFACE FLAWS.....	12
1.3.1 Excitation frequency.....	13
1.3.2 Electromagnetic coupling	14
1.3.3 Eddy current probe	14
1.3.4 Excitation field strength.....	16
1.3.5 Reception unit.....	17
1.3.6 Processing of Signals and images.....	18
1.3.7 Fusion of images	18
1.4 LITERATURE REVIEW	24
1.4.1 Eddy current probe	24
1.4.2 Eddy current instrumentation.....	29
1.4.3 Signal and image processing.....	32
1.4.4 Rapid detection and imaging.....	34
1.5 SUMMARY	39
2 Motivation and Objective	41

2.1	PREAMBLE	41
2.2	MOTIVATION FOR RESEARCH	41
2.3	OBJECTIVE OF RESEARCH	43
2.4	ORGANIZATION OF THE THESIS	44
3	Design and development of eddy current probe.....	46
3.1	PREAMBLE	46
3.2	FINITE ELEMENT MODELLING	46
3.3	GOVERNING EQUATIONS FOR EDDY CURRENT TESTING.....	47
3.4	FINITE ELEMENT MODEL FOR EDDY CURRENT TESTING	48
	3.4.1 Construction of model geometry.....	48
	3.4.2 Meshing.....	50
	3.4.3 Equation solving	50
	3.4.4 Post-processing	51
3.5	MODEL BASED OPTIMISATION OF PROBE CONFIGURATION	51
3.6	RESULTS AND DISCUSSION	54
	3.6.1 Model predicted magnetic field and flux density	54
	3.6.2 Model predicted eddy current density	55
	3.6.3 Model predicted change in phase angle ($\Delta\theta$)	58
	3.6.4 Optimisation of outer diameter of cup-core probe configuration	60
	3.6.5 Selection of excitation frequency of cup-core probe	62
3.7	EXPERIMENTAL STUDIES USING OPTIMISED CUP-CORE PROBE	64
3.8	SUMMARY	65
4	Development of high sensitive eddy current instrument.....	67
4.1	PREAMBLE	67
4.2	DESIGN OF EDDY CURRENT INSTRUMENT	67
	4.2.1 Excitation unit.....	69
	4.2.2 Reception unit.....	71
	4.2.3 Data acquisition and probe scanning.....	73
4.3	TEST SPECIMENS FOR EXPERIMENTS	76
4.4	PERFORMANCE ASSESSMENT OF EDDY CURRENT INSTRUMENT	78

4.4.1 Influence of excitation current	78
4.4.2 Phase angle resolution	80
4.4.3 Drift.....	81
4.4.4 Response of eddy current instrument.....	82
4.5 RESULTS AND DISCUSSION	85
4.5.1 Sub-surface flat bottom holes.....	86
4.5.2 Sub-surface notches.....	86
4.5.3 Surface flaws.....	87
4.6 IMAGING OF SUB-SURFACE FLAWS	89
4.7 SUMMARY	90
5 Development of image fusion methodology	91
5.1 PREAMBLE	91
5.2 IMAGE FUSION	91
5.3 PROPOSED BAYWT BASED IMAGE FUSION METHODOLOGY.....	92
5.4 INPUT EDDY CURRENT IMAGES	94
5.5 PERFORMANCE EVALUATION OF BAYWT IMAGE FUSION.....	94
5.5.1 Standard deviation.....	95
5.5.2 Entropy.....	95
5.5.3 Signal-to-noise ratio	96
5.5.4 Fusion mutual information.....	96
5.5.5 Results and discussion.....	97
5.6 COMPARISON OF PERFORMANCE OF DIFFERENT FUSION METHODOLOGIES	100
5.7 SUMMARY	102
6 Novel scan methodology for rapid detection and imaging of flaws	105
6.1 PREAMBLE	105
6.2 PARAMETERS FOR RAPID SCAN PLANS.....	105
6.3 DESCRIPTION OF THE SCAN PLANS	106
6.3.1 Raster scan.....	106
6.3.2 Diagonal raster scan	107

6.3.3	Spiral scan	107
6.3.4	Lissajous scan	109
6.3.5	Billiard scan.....	109
6.4	IMPLEMENTATION OF SCAN PLANS	111
6.4.1	Numerical investigations	111
6.4.2	Experimental verification	112
6.5	ASSESSMENT OF RAPID SCAN PLANS	114
6.5.1	Rapid detection of a flaw	114
6.5.2	Complete coverage of scanning area.....	117
6.5.3	Step size for detection of flaw.....	120
6.6	BILLIARD SCAN PLAN.....	122
6.6.1	Influence of notch location	122
6.6.2	Influence of notch dimensions	122
6.6.3	Influence of angle of incidence.....	123
6.6.4	Step size for the billiard scan plan.....	124
6.7	EXPERIMENTAL VERIFICATION OF THE BILLIARD SCAN PLAN	126
6.8	SUMMARY	128
7	Conclusion and Future works	130
7.1	CONCLUSION	130
7.1.1	Technical and scientific contributions	132
7.2	FUTURE WORKS	133
	References	136
	Appendix A: The measurement function algorithm.....	143

ABSTRACT

The conventional eddy current testing is confined to detection of sub-surface flaws within a depth of 5.0 mm in an austenitic stainless steel plate due to the skin-effect phenomenon. Many engineering components are made by austenitic thick stainless steel plates in the range of 8.0 mm to 12.0 mm, such as storage tanks. Due to the presence of hostile corrosive environment, the steel undergoes uniform corrosion, localized pitting and stress corrosion cracking on the inner surface. Inspection of the component surface for corrosion is essential to ensure the structural integrity of the storage tanks. Due to the radiation environment, inspection from inner surface is not possible and detection of inside (deep sub-surface) flaws from outer surface is a challenging application of eddy current testing. Further, rapid automated flaw detection is essential in nuclear industry for ensuring high probability of detection as well as minimal dose of radiation for the inspection personnel. Hence, for reliable detection and rapid imaging of sub-surface flaws in austenitic stainless steel components, development of effective eddy current methodologies is required.

This thesis focuses on the design and development of high throughput probes which enable higher strength of the primary magnetic field for deeper penetration of eddy currents into the steel. Finite element modelling based comparative studies have been carried out using COMSOL multi-physics software for selection of optimum coil probe configuration among the send-receive type air core, ferrite core, ferrite core with outer shielding and cup-core probes. This thesis also involves development of a high sensitive eddy current instrument for reliable detection of deep sub-surface flaws. The excitation unit is specially designed to drive a higher excitation current upto 1A into the probe coil and digital lock-in amplifier is designed and implemented using LabVIEW software for precisely measuring the phase lag of the sinusoid from flaws.

To further enhance the detectability of sub-surface flaws with higher signal to noise ratio, this thesis proposes a novel BayWT based image fusion methodology that combines the wavelet transform and Bayesian methodologies. Performance of the proposed fusion methodology is compared with the widely used image fusion methodologies e.g. Laplacian pyramid, wavelet transform, principal component and Bayesian based image fusion. This thesis also proposes a novel scan plan for rapid detection and imaging of flaws which is essential for radioactive environment. For development of the novel scan plan, detailed systematic studies have been carried out for different scan plans viz. raster, diagonal raster, spiral, Lissajous and billiard scan plans.

These developed methodologies are applied to 12.0 mm thick AISI type 304L stainless steel plates for detection of flat bottom holes (simulating sub-surface localized corrosion) and EDM notches (simulating sub-surface cracks). The methodologies presented in this thesis demonstrate the synergistic combination of cup-core coil probe and high sensitive instrument for detection of flaws located 8.0 mm below the surface and imaging of flaws using the novel BayWT based image fusion methodology. This study establishes, for the first time, that the billiard scan plan is an attractive scan plan for rapid and reliable eddy current imaging of flaws in large surfaces of electrically conducting materials.

LIST OF FIGURES

Figure 1.1: A generic non-destructive evaluation system.....	3
Figure 1.2: Basic principle of the ECT technique.....	6
Figure 1.3: Applications of the ECT technique.....	9
Figure 1.4: (a) Cross section of test plate with four surface flaws of different length (b) test plate with a flaw for EC imaging.	9
Figure 1.5: Typical EC signals for four surface flaws in (a) time-domain signal (b) impedance-plane signal.	10
Figure 1.6: Typical raster scan EC images of a flaw (a) real, (b) imaginary, (c) amplitude and (d) phase angle.	11
Figure 1.7: Standard depth of penetration and effective depth of penetration.	13
Figure 1.8: Standard and effective depth of penetration with varying frequency.	14
Figure 1.9: The typical EC probes used in various applications (a) surface (b) pencil (c) encircling and (d) bobbin.	15
Figure 1.10: Mode of operation of EC probes (a) absolute (b) send-receive (c) differential (d) magnetic sensor.....	16
Figure 1.11: Effective depth of penetration for varying excitation current.....	17
Figure 1.12: Schematic diagram of Laplacian transform based image fusion.	20
Figure 1.13: Schematic diagram of wavelet transform based image fusion.....	21
Figure 1.14: Schematic diagram for image fusion using principal component analysis.	23
Figure 1.15: Cross section of surface probe over a conducting surface (a) small diameter single coil (b) large diameter single coil and (c) double coil probe [40].....	25
Figure 1.16: Predicted change rates of impedance and induced voltage due to (a) lift off change (b) flat bottom hole depth change [40].....	25
Figure 1.17: Response of integrated EC GMR sensor and pancake type absolute EC sensor signal from (a) EDM notches (b) the sensor output for flat bottom hole located at different depths [42].	27

Figure 1.18: Differential Hall sensor probe response for sample having EDM notches at different depths [43].....	27
Figure 1.19: The architecture of the developed system A [53].....	29
Figure 1.20: Signature EC signals obtained by the system A for a flaw at three excitation frequencies [53].....	30
Figure 1.21: (a) Schematic of I/Q detection scheme. EC images obtained using (b) the I/Q scheme (c) traditional sample-stop-sample scheme [55].....	31
Figure 1.22: (a) Array probe with 32 absolute coils and (b) array probe 64 send-receive mode coils.	37
Figure 1.23: The intelligent eddy current imaging scheme developed for quick and automated detection and characterization of flaws [82].	39
Figure 1.24: Three dimension image obtained by the intelligent imaging for a stainless steel plate consisting of a notch (length 3.0 mm, width 0.3 mm and depth 0.8 mm) and a flat bottom hole (diameter 1.5 mm and depth 0.5 mm) [82].	39
Figure 3.1: The typical geometry of model with a boundary region.	49
Figure 3.2: Discretisation of triangular mesh in the modelled geometry.	50
Figure 3.3: Typical surface and contour plot of magnetic flux density and induced current density.	51
Figure 3.4: Cross-section of send-receive probe configurations studied through FE model (a) air core (b) ferrite core (c) ferrite core with outer shielding (d) cup-core.....	52
Figure 3.5: Specimen with surface and sub-surface flaw of same depth d in 12.0 mm thick austenitic stainless steel plate.	53
Figure 3.6: Surface log plot of magnetic flux density and arrow plot of the magnetic field for send-receive type (a) air core, (b) ferrite core, (c) ferrite core with outer shielding and (d) cup-core eddy current probes.	55
Figure 3.7: Surface plot of eddy current density for a sub-surface flaw located at 8.0 mm below the surface for (a) air core, (b) ferrite core, (c) ferrite core with outer shielding and (d) cup-core eddy current probes.	57

Figure 3.8: Model predicted eddy current density for sub-surface flaws located at different depths (D) below the surface for all the four type of probes.	58
Figure 3.9: Model predicted eddy current density for surface flaws of varying depths ($d = 5.0, 6.0, 7.0$ and 8.0 mm) for all the four type of probes.	59
Figure 3.10: The normalised change in phase angle ($\Delta\theta$) for sub-surface flaws located at different depths (D) below the surface.	59
Figure 3.11: The normalised change in phase angle ($\Delta\theta$) for surface flaws of varying depths ($d = 5.0, 6.0, 7.0$ and 8.0 mm).	60
Figure 3.12: Model predicted normalised change in phase angle ($\Delta\theta$) of the cup-core probe at 5 kHz for various outer diameters for flaw located at 8 mm below the surface.	61
Figure 3.13: Model predicted induced voltage of the cup-core probe at 5 kHz for various outer diameters for flaw located at 8 mm below the surface.	61
Figure 3.14: Model predicted eddy current density for (a) sub-surface flaw (b) surface flaw and the normalised change in phase angle ($\Delta\theta$) for (c) sub-surface flaw (d) surface flaw of 22.0 mm diameter probes.	63
Figure 3.15: FE model predicted induced current density at different depth below the surface at frequency 3 kHz, 5 kHz and 7 kHz for the 22.0 mm diameter cup-core probe.	64
Figure 3.16: (a) Cross section of the cup-core probe and (b) photograph of the fabricated ECT probe.	65
Figure 4.1: Main modules of an eddy current instrument.	67
Figure 4.2: Schematic block diagram of the ECT Instrument.	69
Figure 4.3: Circuit diagram of developed excitation unit.	70
Figure 4.4: Schematic diagram of implementation of lock-in amplifier in LABVIEW development environment.	73
Figure 4.5: Block diagram of the lock-in amplifier based phase measurement.	74
Figure 4.6: Front panel GUI of the lock-in amplifier based phase measurement.	75

Figure 4.7: Schematic of stainless steel plates with machined (a) flat bottom holes (b) notches (width 2.5 mm) and (c) notches (width 1.0 mm)..... 77

Figure 4.8: Photograph of the developed ECT instrument..... 78

Figure 4.9: Measured coil temperature as function of the excitation current in ECT probe. 79

Figure 4.10: (a) Magnitude (b) change in phase angle response of the cup-core probe at different excitation currents for sub-surface notches D3 and D4..... 80

Figure 4.11: (a) Temperature of the excitation coil and (b) change in phase angle as function of time. 81

Figure 4.12: Time domain (a) in-phase and (b) quadrature components signals obtained for sub-surface notches. 82

Figure 4.13: Impedance plane signals obtained for sub-surface notches..... 83

Figure 4.14: (a) Peak magnitude and (b) peak of change in phase angle of sub-surface notches. 84

Figure 4.15: Linear behavior of notch location below the surface (D) as function of change in phase angle ($\Delta\theta$). 84

Figure 4.16: Comparison of detection performance of the proposed EC instrument with a commercial instrument..... 85

Figure 4.17: EC signal obtained for 3.0 mm diameter FBHs located at different depths (D) below the surface in a 12.0 mm thick SS plate. 86

Figure 4.18: The EC signal obtained for sub-surface notches located at different depths (D) below the surface..... 87

Figure 4.19: The EC signal is obtained for surface notches of varying depths (d = 4.0, 6.0 and 8.0 mm) notches. 88

Figure 4.20: EC image of 4 sub-surface notches in SS plate (a) change in phase angle (b) magnitude. 89

Figure 5.1: Block diagram of the proposed BayWT based image fusion methodology..... 93

Figure 5.2: CIVA model predicted phase angle images of a sub-surface flaw located at 8.0 mm below the surface at frequency (a) 5 kHz and (b) 7 kHz with additive noise of 30% of maximum phase and SNR of 5 dB.	97
Figure 5.3: Experimentally obtained phase angle images of a sub-surface notch located at 8.0 mm below the surface at frequency (a) 5 kHz and (b) 7 kHz.	98
Figure 5.4: Fused phase angle images of sub-surface flaw located at 8.0 mm below the surface of (a) model predicted and (b) experimentally generated.	99
Figure 5.5: Fused phase angle images of different fusion methodologies (a) Laplacian pyramid (b) wavelet transform (c) principal component analysis (d) Bayesian method (e) BayWT method.	101
Figure 5.6: Fused phase angle images of different fusion methodologies (a) Laplacian pyramid (b) wavelet transform (c) principal component analysis (d) Bayesian method (e) Proposed BayWT method.	103
Figure 6.1: Raster scan pattern on the surface of a plate.	107
Figure 6.2: Diagonal raster scan plan on the surface of a plate.	108
Figure 6.3: Spiral scan plan on the surface of a plate.	108
Figure 6.4: Lissajous scan plan on the surface of a plate.	110
Figure 6.5: Billiard scan plan on the surface of a plate.	110
Figure 6.6: (a) Point spread function of eddy current probe and (b) image of a notch in test specimen.	111
Figure 6.7: Scan region showing 1000 random locations of image of a modelled notch in SS plate.	112
Figure 6.8: Flow graph of automated scanning program for detection of flaw.	113
Figure 6.9: Schematic of the test specimen with notches for (a) rapidness analysis (b) imaging.	114
Figure 6.10: Scattering point of the number of steps required to detect all 1000 modelled notches using (a) raster (b) diagonal zigzag (c) spiral (d) Lissajous (e) billiard scan plans.	115

Figure 6.11: Box plot of the number of steps required to detect all 1000 modelled notches using all the five scan plans.....	117
Figure 6.12: Number of notch detections by (a) raster (b) diagonal zigzag (c) spiral (d) Lissajous and (e) billiard scan plans.	118
Figure 6.13: Percentage of notches detected by different scan plans.	119
Figure 6.14: Box plot of the number of steps required to detect all the 1000 modelled notches by different scan plans at a step size of (a) 3.0 mm (b) 5.0 mm (c) 7.0 mm and (c) 10.0 mm.	121
Figure 6.15: Missing location of notches in modelled test specimen and coverage of the scan plans (a) Lissajous (b) billiard.	122
Figure 6.16: Detection of notches with different length of notches for (a) Lissajous scan plan (b) billiard scan plan.....	123
Figure 6.17: Percentage of notch detection for the billiard scan plan at different angles of incidence.	124
Figure 6.18: Bar plot for distance travelled to detect the notch at a step size of (a) 5.0 mm (b) 7.0 mm (c) 10.0 mm for the billiard scan plan.....	125
Figure 6.19: The box plot for distance travelled to detect the notch at different step sizes by the billiard scan plan.	126
Figure 6.20: Number of steps required to detects all the 13 notches by different scan plans.	127
Figure 6.21: Amplitude image of notch D14 resulted by billiard scan plan.	128

LIST OF TABLES

Table 1.1: NDE fusion methodologies.....	35
Table 3.1: Details of the sub-domain parameters used in the FE model.....	49
Table 3.2: Slope of eddy current density for four type of probes for detection of sub-surface flaws.....	56
Table 3.3: Slope of eddy current density for the four types of probes for detection of surface flaws.....	58
Table 3.4 Dimensions of the cup-core EC probe.....	64
Table 4.1: Dimensions of machined notches in SS 304L plate.....	76
Table 4.2: Dimensions of flat bottom holes in SS 304L plate.....	77
Table 4.3: Change in phase angle for five line scan points (step size 2.0 mm).....	81
Table 5.1: Steps involved in the implementation of the BayWT based fusion methodology.....	93
Table 5.2: Assessment metrics of fused model predicted phase angle image.....	99
Table 5.3: Assessment metrics of fused experimental generated phase angle image.....	99
Table 5.4: Comparative performance of different fusion methodologies using model predicted phase angle images of a sub-surface flaw located 8.0 mm below the surface.....	100
Table 5.5: Comparative performance of different fusion methodologies using experimental generated phase angle images of a sub-surface flaw located 8.0 mm below the surface.....	102
Table 6.1: Maximum and mean number of steps required by different scan plans for the first-time detection of 1000 notches at 5.0 mm step size.....	116
Table 6.2: Mean value of the number of steps required for first time detection of notches at different step sizes.....	120
Table 6.3: Standard deviation value of the number of steps required for first time detection of notches at different step sizes.....	121

Table 6.4: Number of steps required for first time detection of all the 13 notches. 127

NOMENCLATURE

LIST OF SYMBOLS

kHz	Kilo Hertz
MHz	Mega Hertz
mm	millimeter
m/s	meter per second
J	Current density
B	Magnetic field vector
E	Electric field
μ	Magnetic permeability
μ_r	Relative magnetic permeability
σ	Electrical conductivity
ω	Angular frequency
f	Frequency
β	Phase lag
Z	Impedance
δ	Standard depth of penetration
δ_E	Effective depth of penetration
Δ	Step size
kA/m^2	Kilo ampere per meter square
D	Flaw location below the surface
d	Flaw depth
θ	Phase angle
$\Delta\theta$	Change in phase angle
A	Ampere
V	Electric scalar potential or volts
mA	milli ampere
mV	milli volts
GND	Ground
mHz	Milli Hertz
dB	deciBel

LIST OF ABBREVIATIONS

AC	Alternating current
ADC	Analogue-digital converter
AISI	American Iron and Steel Institute
BayWT	Bayesian and wavelet transformed
DAQ	Data acquisition
EC	Eddy current
ECT	Eddy current testing
EDM	Electric discharge machining
ENDE	Electromagnetic non-destructive evaluation
FBH	Flat bottomed holes
FE	Finite element
FMI	Fusion mutual information
GMR	Giant-magneto resistive
GUI	Graphical user interface
IACS	International Annealed Copper Standard
ICA	Independent component analysis
ID	Inner diameter
I/Q	In-phase/quadrature
NDE	Non-destructive evaluation
OD	Outer diameter
PCA	principal components analysis
PDE	Partial differential equation
PEC	Pulsed eddy current
POD	Probability of detection
PSF	Point spread function
SNR	Signal to noise ratio
SS	Stainless steel
THD	Total harmonic distortion
WT	Wavelet transform

Introduction

The scope of this chapter is to introduce the context of detection of sub-surface flaws in austenitic stainless steel using eddy current testing (ECT) and to discuss the methodologies reported so far for detection of sub-surface flaws. The chapter starts with a brief introduction to non-destructive evaluation. The principle of ECT technique along with the characteristics of eddy current signals and images from flaws are discussed. The applications of ECT technique for detection of sub-surface flaws in thick components are discussed in detail. The important factors to be considered for detection of sub-surface flaws in stainless steel are also discussed.

1.1 Non-destructive evaluation

Non-destructive evaluation (NDE) is essential for ensuring quality, safety and reliability of engineering components. As the name implies, NDE assesses the immaculacy and adequacy of materials, structures and fabricated components without disturbing the functional properties and worth[1,2]. NDE provides information about discontinuities that affect the availability, productivity, and profitability of operating components in nuclear, transportation, aerospace, petrochemical and other industries. A discontinuity that creates a substantial chance of material failure in service is commonly called a *flaw*. Flaws in a component can arise due to any one of the following reasons [3]:

1. Improper manufacturing processes such as casting, welding, rolling, forging and machining and component assembly.
2. Environmental and loading conditions during transport, storage and service e.g. stress corrosion crack, fatigue, creep, thinning and hydrogen or helium embrittlement.

A flaw detected by an NDE technique has to be evaluated before taking a decision on replacement or repair of a component. Flaw detection and sizing are essential to ensure safety and reliability of components.

Stainless steels (SS) are one of the major structural materials used in various industries, in view of their good corrosion resistance and better high temperature mechanical properties (yield, ductility, and toughness). SS are classified into four different grades viz. austenitic, ferritic, martensitic and duplex (austenitic-ferritic) according to the microstructure. Austenitic steels are derived from 18% Cr – 8% Ni composition and mostly used in nuclear industries because of austenitic steels work best in hot environments [4]. In austenitic SS components flaws are formed due to exposure to high temperatures, pressures, irradiation, and hostile corrosive media. Austenitic SS is non ferromagnetic (relative magnetic permeability is 1). NDE of austenitic stainless steels for detection of flaws is challenging because of lower conductivity (1.38×10^6 S/m).

A numbers of NDE techniques are available to detect flaws in austenitic SS. The most widely used NDE techniques are ultrasonic, radiography, eddy current, acoustic emission technique [5]. All these NDE techniques are based on different physical principles. A schematic block diagram of a generic NDE system is shown in Figure 1.1. In general, an NDE system consists of three basic units i.e. excitation unit, reception unit and post processing unit. In the excitation unit, particular form of energy, e.g. electromagnetic energy in ECT, is used as an input for the exciter coil so that the coil sends this energy into the object under test. The energy applied into the object is transformed (e.g. in ECT transformation is in the form of induced eddy currents and their secondary magnetic fields) depending on the object material properties and flaws present in the object. The transformed energy is picked by a receiver coil or sensor in the reception unit. Finally, this receiver response is processed and displayed in the form of a signal to extract information about the flaws present in the object under test [6].

The NDE techniques can be broadly classified into two categories i.e. active and passive techniques. In active techniques, some form of energy is introduced into the object under test and the change in the input energy or reception unit is monitored if there is any flaw present in the object. Eddy current, ultrasonic, and radiographic techniques are the active NDE techniques. In the case of passive techniques, flaws are detected by some response or reaction from the object without any excitation. Visual technique and acoustic emission technique belong to the passive techniques category [5].

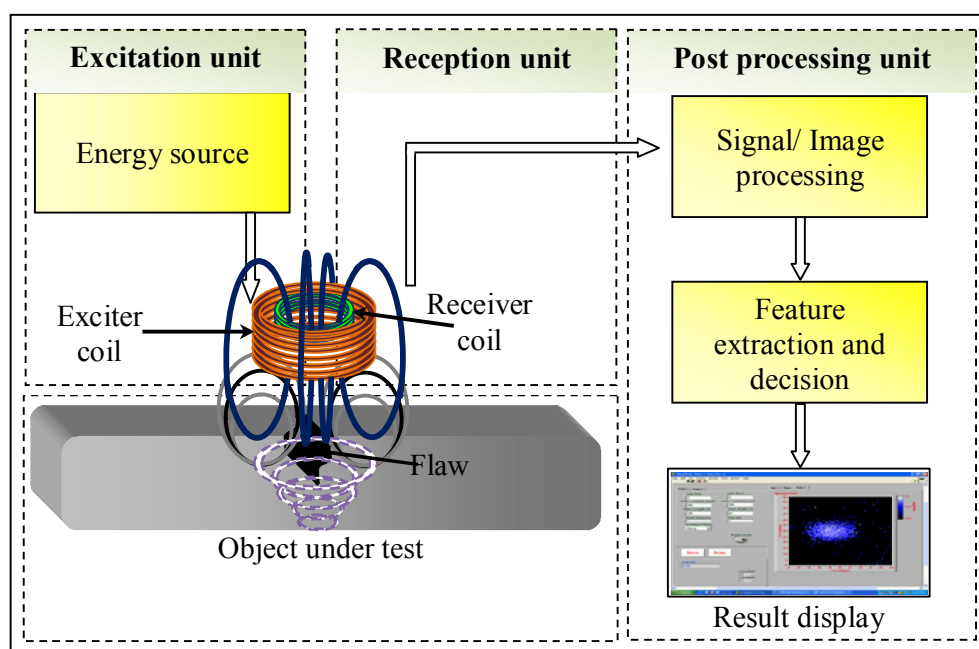


Figure 1.1: A generic non-destructive evaluation system.

Among the NDE techniques, visual technique is the oldest and the least expensive NDE technique. This is used as a first step to assess the health of an object by using magnifying glasses, digital cameras and video equipments. Visual technique is not suitable for detection of shallow/tight surface flaws and cannot detect sub-surface flaws. Liquid penetrant technique is useful for detection of surface cracks in any kind of material as long as the material is non-porous. Magnetic particle technique is applicable for detection of surface and sub-surface flaws in ferromagnetic objects. Even though the principle of magnetic particle technique is simple, but this technique only indicates the

presence of a flaw and cannot give any quantitative information. Acoustic emission and infrared thermography techniques are dynamic techniques and are used for detection of growing cracks, leaks and hot spots respectively. Radiography technique is widely used for volumetric inspection of castings, welds, bonded structures, electronic components and composite materials. This technique requires access from both sides. Compared to other NDE techniques radiography technique is expensive and proper safety, precautions are required for inspection because of the use of X-rays or γ -rays. Ultrasonic technique is the most versatile active NDE technique. This technique uses high frequency (0.5 to 25 MHz) ultrasound energy for dimensional measurements, flaw detection and microstructure characterisation. This technique requires coupling medium to introduce the sound energy into the material and cannot be used for laminated or layered structures. Skilled operators are required to perform ultrasonic inspections. ECT is a widely used electromagnetic NDE (ENDE) technique for detection and sizing of surface as well as near sub-surface flaws in electrically conducting materials. In this technique, detection of flaws is confirmed by measuring the changes in impedance of a coil excited with an alternating current. This is a simple and portable NDE technique used for inspection of components made of metallic materials.

A single NDE technique cannot detect all types of flaws. Each of the NDE techniques has its own advantages and limitations as compared to other NDE techniques. For selection of a suitable NDE technique, the material properties, details of the expected flaws, manufacturing process, environment surrounding of the components, accessibility, and cost as well as capability of the selected technique are to be considered.

Among the NDE techniques, ENDE techniques are mostly used for detection of flaws in thin (thickness ≤ 5.0 mm) electrical conducting materials, such as stainless steel, aluminum, inconel, brass and copper, etc. [7]. ECT is the extensively used in aerospace, nuclear, petrochemical, and automobile industries. The main reasons behind the numerous and widespread use of ECT is:

- The excellent detection sensitivity for surface as well as near sub-surface flaws (≤ 5.0 mm)
- Ease of operation
- Versatility
- Extremely high testing speeds (up to 10 m/s)
- Data storage possibility and
- Repeatability.

This technique can detect wall thinning, cracks, pitting, stress corrosion cracking, hydrogen embrittlement, denting and deposits [8].

1.2 Eddy current testing

Research in eddy currents started with the discovery of electromagnetic induction by Michael Faraday's in 1831. Faraday's stated that the electromagnetic force is generated in a conducting material if placed in a time varying magnetic field. In 1851 Leon Foucault discovered the phenomena of eddy currents and showed that eddy currents are generated when a copper disk moves within an applied magnetic field. The understanding entered into another stage with the discovery of change in coil properties for different conductivity and permeability metals by David Hughes in 1879. Use of ECT in industries was pioneered by Prof. Friedrich Forster in 1940's [9].

1.2.1 Principle of eddy current testing

Eddy current technique works on the principle of electromagnetic induction. A schematic of the working principle of ECT technique is shown in Figure 1.2. When an alternating current (AC) is applied to a coil (also called probe), primary magnetic field gets generated near the coil following the Ampere's law. Due to the primary magnetic field, magnetic flux (ϕ_p) exists and this is proportional to the number of turns in the coil (N_p) and the current I_p according to Oersted's (i.e. $\phi_p \propto N_p I_p$). When an electrically conducting material, e.g. stainless steel, aluminum, etc. is

placed near the coil, eddy currents are induced in the material according to the Faraday's law. The governing differential equation for an eddy current probe excited with alternating current producing an eddy current density J in a homogeneous isotropic electrically conducting material shown in Figure 1.2 is derived from the following Maxwell's curl equations [7]:

$$\nabla \times E = - \frac{dB}{dt} \quad (1.1)$$

$$\nabla \times B = - \mu J \quad (1.2)$$

where E is the electric field, B is the magnetic field vector, J is the current density and μ is the magnetic permeability of the material. The governing partial differential equation describing the ECT technique is given as

$$\nabla^2 J = j\omega\mu\sigma J \quad (1.3)$$

where ω is the angular excitation frequency and σ is the electrical conductivity.

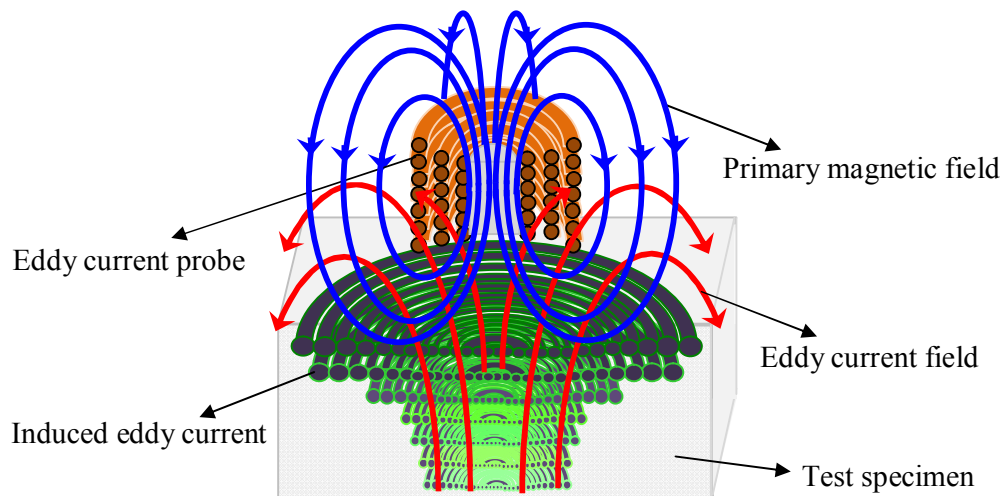


Figure 1.2: Basic principle of the ECT technique.

Solving equation 1.3 provides the distribution of the eddy current density (J) in the thickness direction [10]:

$$J_z = J_0 e^{-\beta} \sin(\omega t - \beta) \quad (1.4)$$

where J_z is the induced current density along the thickness of the material (z-axis) and J_0 is the induced current density at the surface of the material. β is the phase lag at depth, z and is defined as:

$$\beta = z\sqrt{\pi f \mu \sigma} \quad (1.5)$$

The induced current density contains the magnitude and phase lag information which represents the flow of eddy currents in the material. The flow of eddy currents is not uniform in the thickness direction. In the induced current density equation 1.4, the magnitude decays exponentially and the phase lag, β varies linearly with the thickness. The eddy currents is maximum at the surface of the material and decreases continuously with depth, this phenomenon is called *skin effect*. The depth at which the current density decreases by the factor $1/e$ or 36.8% from the surface current density (J_0) in a material is called standard depth of penetration (δ) and this is defined as [7]:

$$\delta = \frac{1}{\sqrt{\pi f \mu \sigma}} \quad (1.6)$$

where δ is the standard depth of penetration, f is the excitation frequency and σ is the electrical conductivity. As can be seen from equation 1.6, the standard depth of penetration depends on f , σ and μ . Any increase in the values of these parameters decreases δ .

The induced eddy currents in the test object generate a secondary magnetic field in the material that opposes the primary magnetic field according to the Lenz's law (i.e. $\varphi_s \propto -N_p I_s$). The total magnetic field (difference between primary and secondary magnetic fields) is linked to the coil causing a change in the impedance (Z) of the coil. The impedance is a complex quantity with the resistance, R (real) and the inductive reactance, X_L (imaginary) components as:

$$Z = R + jX_L \quad (1.7)$$

where magnitude and phase angle of the coil impedance is expressed as:

$$Z = \sqrt{R^2 + X_L^2} \quad (1.8)$$

$$\theta = \tan^{-1}\left(\frac{X_L}{R}\right) \quad (1.9)$$

The presence of a flaw in the object under test or change in the material properties causes a discontinuity in the eddy current flow and results in change in coil impedance. The change in impedance indicates the presence of a flaw or discontinuity in the object [3]. The response of eddy currents can also be detected using a separate receiver coil or solid state sensor e.g. Hall, GMR.

ECT technique is employed in chemical, nuclear, petroleum and aerospace industries. The applications may be grouped into the following four broad categories viz. flaw detection, dimensional measurement, proximity sensing and material sorting [3] as illustrated in Figure 1.3. From these applications, early detection of flaws is paramount since presence of the flaws in a component can cause catastrophic failure of the component. In a component two types of flaws are possible. First type is a surface flaw which is accessible during the component inspection. Second type is a sub-surface flaw which is embedded and inaccessible and inspection of the component is possible from one of the surfaces.

1.2.2 Detection of surface flaws

ECT is an excellent technique for detection of surface flaws. This technique can detect 0.1 mm wide shallow surface flaws with high sensitivity. Like many signals in communication systems, impedance change signal is not generally usable in the form in which it is received from the test coil. Signal analysis techniques are applied to interpret the received signal and display in the form of amplitude, phase angle, real and imaginary components in impedance plane or in time-domain.

The locus of changes in impedance of an EC probe, during the movement of the probe over a test object as illustrated in Figure 1.4 (a) is called an EC signal. The signal consists of two components viz. resistance and inductive reactance as a function of distance or time, as shown in Figure 1.5 (a).

The EC signal is also visualized as a Lissajous figure on the complex (impedance) plane as shown in Figure 1.5 (b) with resistance, as abscissa and inductive reactance, as ordinate. Figure 1.5 typically shows the time-domain real and imaginary components as well as the impedance-plane of the EC signal for four surface flaws D1 (20.0 mm length), D2 (25.0 mm length) and D3 and D4 (30.0 mm length). Depth of the flaws D1, D2 and D3 is 3.0 mm, while depth of the flaw D4 is 5.0 mm.

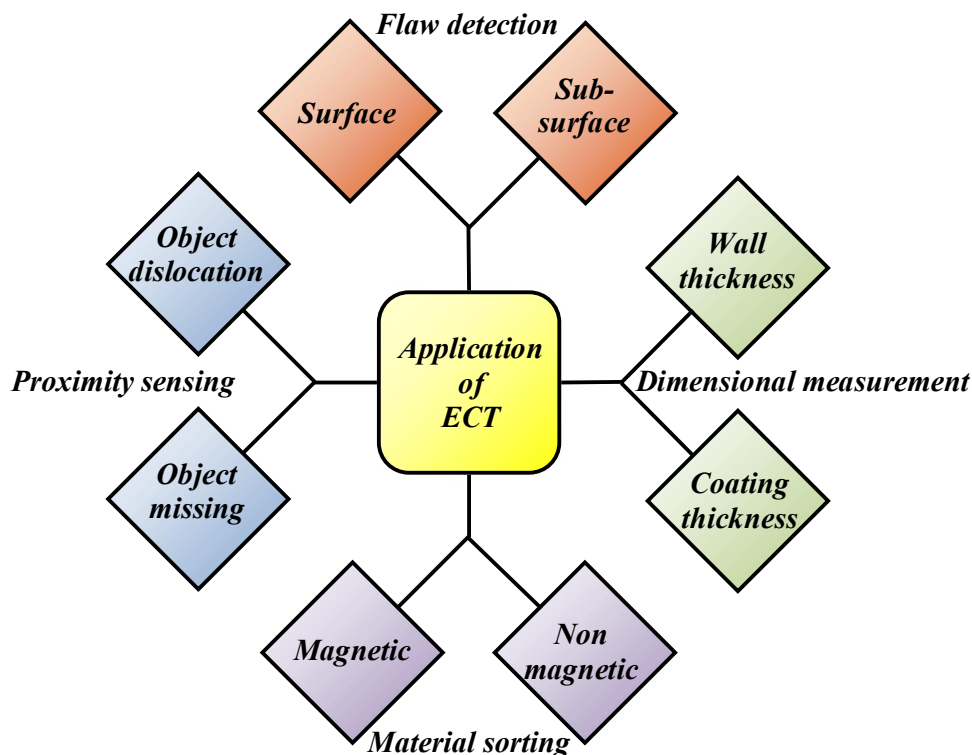


Figure 1.3: Applications of the ECT technique.

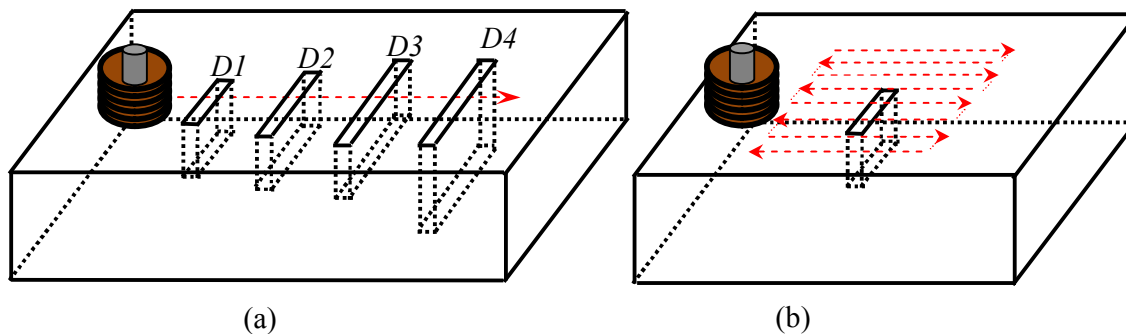


Figure 1.4: (a) Cross section of test plate with four surface flaws of different length (b) test plate with a flaw for EC imaging.

The maximum amplitude in Figure 1.5 of the flaws signals correspond to the maximum interaction region of the probe with the flaws [7]. In the impedance plane, the amplitude is square root sum of real and imaginary components of the EC signal and this provides the information about the flaw volume. The phase angle of the signals in Figure 1.5 (b) provides the information about the flaw's depth or location. From the time-domain and impedance plane signals, magnitude and phase of the signals can be measured.

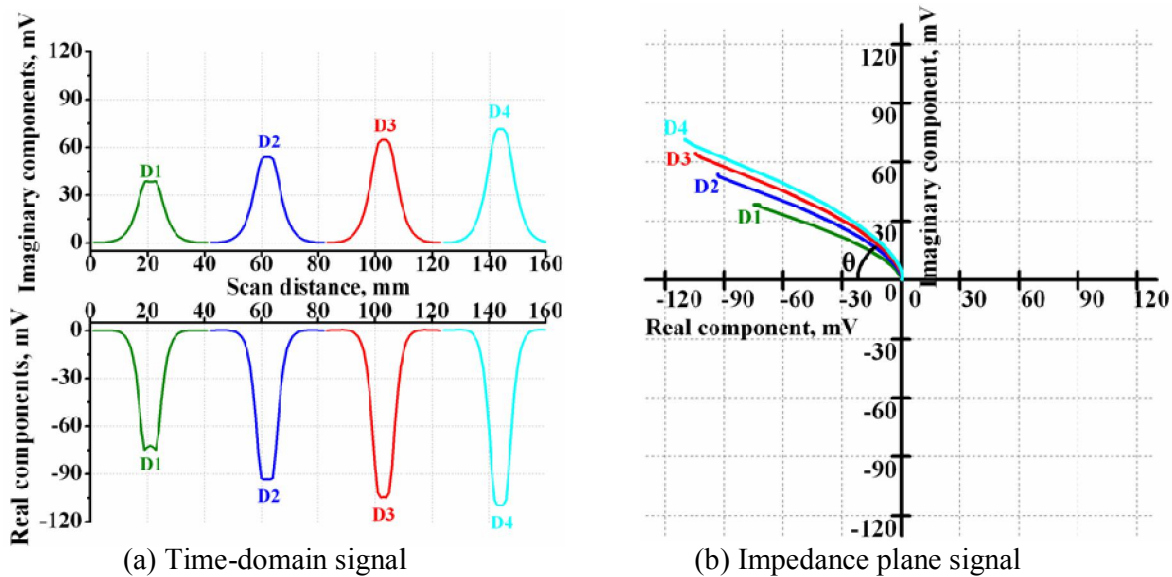


Figure 1.5: Typical EC signals for four surface flaws in (a) time-domain signal (b) impedance-plane signal.

Using the EC signals, one can detect flaws e.g. by employing thresholding and can get information about the height of flaws by employing signal processing method that remove noise. However, flaws which are described as three-dimensional functions of the space co-ordinates cannot be completely reconstructed by merely scanning an EC probe over a flaw in one direction, even using sophisticated signal processing method.

A definite benefit exists if a series of parallel line scans (raster scan) are made and the resulting eddy current data viz. resistance, inductive reactance, magnitude and phase are presented in the form of a pseudo color or a gray level image [11,12,13]. This, often referred as eddy current imaging,

automates the measurement process. The typical EC images (resistance, inductive reactance, amplitude and phase images) for a flaw of length 15.0 mm, depth 6.0 mm and width 1.0 mm, shown in Figure 1.4 (b) using an absolute EC probe (diameter 20.0 mm) are shown in Figure 1.6. EC imaging can be done using a single sensor or by using an array of sensors (one-dimensional or 2-dimensional arrays).

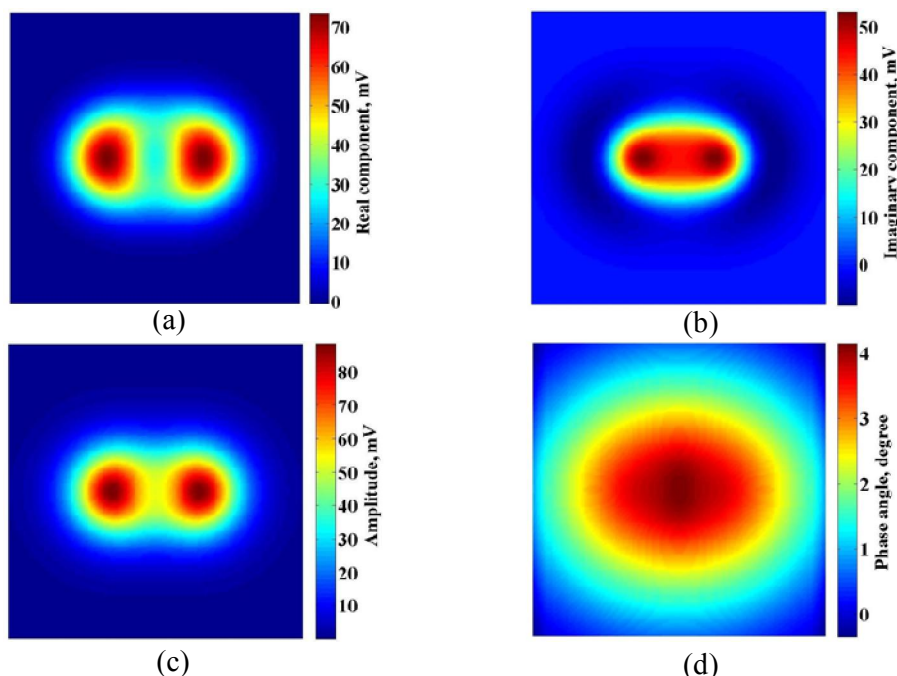


Figure 1.6: Typical raster scan EC images of a flaw (a) real, (b) imaginary, (c) amplitude and (d) phase angle.

EC imaging large areas of austenitic stainless steel surface is a time consuming process. EC imaging in radioactive environment, demands rapid detection and imaging of flaws to reduce the radiation dose to the inspection personnel. At the same time, ensuring 100% coverage of the component surface without compromising the detection sensitivity is also desired. Thus, evolving scan plans for fast and reliable detection and imaging of flaws is essential. Because of the ease of instrumentation and cost, use of single probe covering the total surface by raster scan or other possible scan plans is attractive as compared to line scans by array probes.

1.2.3 Detection of sub-surface flaws

The ECT technique is in general, confined to detection of sub-surface flaws within a depth of 5.0 mm in austenitic stainless steels. Components such as storage tanks, dissolver vessels etc. are made with thick stainless steel plates in the range of 8.0 mm to 12.0 mm. This type of components is used in petrochemical industries and nuclear reprocessing plants for storage and transportation of different chemicals. In nuclear reprocessing plants, storage tanks are used to store the radioactive liquid waste in nitric acid medium arising from the reprocessing operations. These tanks are made of AISI type 304L austenitic stainless steel. This steel undergoes several types of corrosion namely end-grain attack, uniform corrosion, tunnelling corrosion, transpassive dissolution [14,15]. Periodic non-destructive inspection of these components for detection of corrosion is required to ensure the structural integrity and to continue to use. Due to the radiation environment, inspection of the tanks from inner surface is not possible and detection of inside (deep sub-surface) flaws and corrosion damage from the outer surface is challenging for the ECT technique.

1.3 Considerations for detection of sub-surface flaws

There are some factors which influence the capability of ECT technique for detection of sub-surface flaws. Penetration of eddy currents into the material upto the flaw location is essential, since the change in impedance occurs only when eddy currents are disturbed by the flaw. As the standard depth of penetration is limited by the material properties and excitation frequency, this behavior cannot be changed fundamentally. But by the optimization of ECT probes and testing parameters, enhanced penetration can be achieved and this penetration is called the effective depth of penetration, (δ_E). This is the depth at which eddy current density decreases to $1/e^3$ or 4.9% of the surface current density. Beyond this depth change in coil impedance is negligible [16,17]. The effective depth of penetration is also the depth upto which eddy current signals are received with sufficient signal to noise ratio (SNR) [18] which depends on the test material, instrument, probe,

operator and test condition. Figure 1.7 shows the standard depth of penetration and effective depth of penetration for a SNR of 6 dB. As can be seen in figure effective depth penetration for a SNR 6 dB is equal to 1.5 times of the standard depth of penetration.

Apart from the effective depth of penetration, measuring instruments and post processing techniques are also important for detection of sub-surface flaws. A few important considerations for achieving higher sensitivity for detection of sub-surface flaws are described in this section:

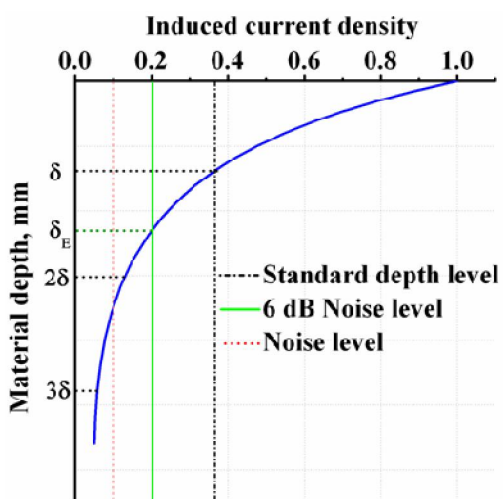


Figure 1.7: Standard depth of penetration and effective depth of penetration.

1.3.1 Excitation frequency

The excitation frequency determines the depth of penetration of eddy currents into the test object. For detection of deep sub-surface flaws lower excitation frequency level is preferred as illustrated in Figure 1.8. From the figure it is clear that as decreasing the excitation frequency, effective depth of penetration for a SNR of 6 dB increases. Although lowering the excitation frequency appears beneficial for detecting the sub-surface flaws, it reduces the sensitivity, SNR, and resolution due to the divergence of magnetic fields and poor coupling energy between the test material and test coil. Hence, for detection of sub-surface flaws selection of excitation frequency is important.

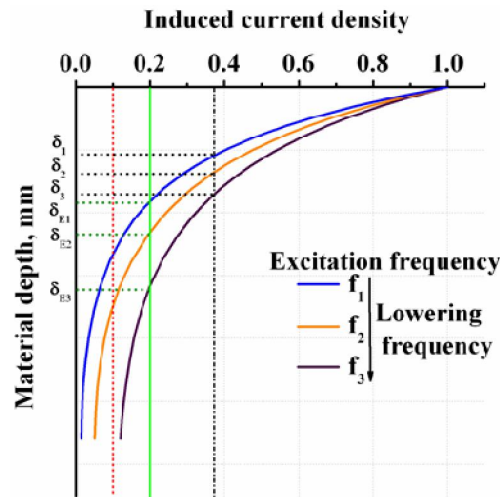


Figure 1.8: Standard and effective depth of penetration with varying frequency.

1.3.2 Electromagnetic coupling

Electromagnetic coupling between the test coil and the object under test is very important during inspection, because it decides the interaction between the test coil and the object. Lift-off, fill-factor, edge-effect and end-effect describe the electromagnetic coupling. The coupling between the test coil and object under test varies with the spacing between the test coil and the test object and this spacing is called ‘lift-off’ for inspections using the pancake probes and called ‘fill-factor’ for inspections using the bobbin probes [3]. Variation in coupling due to change in lift-off results in noisy signal, generally termed as lift-off signal or wobble signal that disturbs the inspection. During ECT, zero lift-off or uniform lift-off is preferred and usually, the lift-off signal is made parallel to the X-axis on the impedance plane display for reference as well as for phase discrimination purpose. The use of spring loaded surface probes ensure good electromagnetic coupling and this reduces disturbing signals from variations in lift-off.

1.3.3 Eddy current probe

Probe is the main link between the EC instrument and the test object and it has two main functions. First, the EC probe establishes varying electromagnetic fields that induce eddy currents in the object

under test. Second, the probe senses the change in impedance due to the presence of flaws in the test object. Eddy current probes are classified by the configuration and mode of operation of the test coils. The configuration of the probe generally refers to the way the coil or coils are packaged to best "couple" to the test area of interest. The typical EC probes are shown in Figure 1.9. Different types of probe configurations widely used for different applications include the following:

- ◆ Surface or pancake or pencil type probes (with the probe axis normal to the object surface), used for testing plates and bolt-holes.
- ◆ Encircling probes used for inspection of rods, bars and tubes with outside access.
- ◆ Bobbin probes used for inspection of tubes with inside access e.g. heat exchanger tubes.

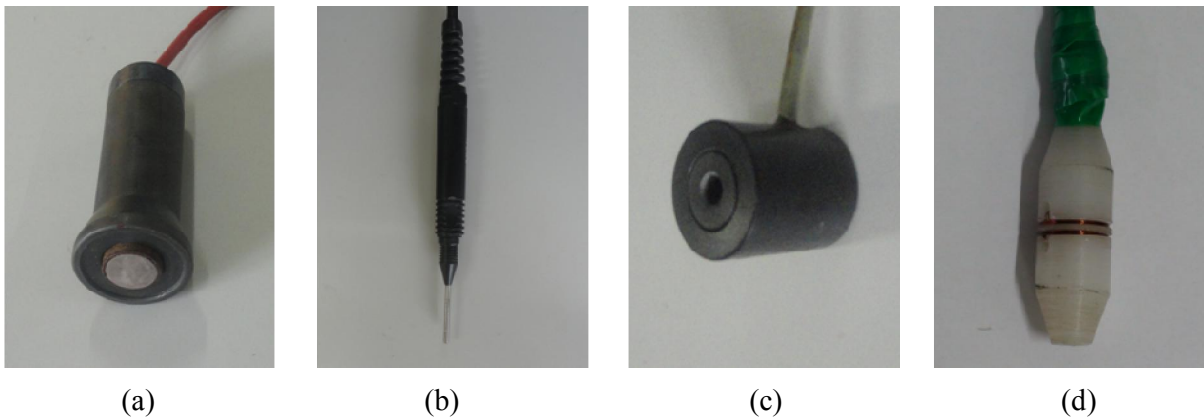


Figure 1.9: The typical EC probes used in various applications (a) surface (b) pencil (c) encircling and (d) bobbin.

The mode of operation refers to the way the test coil or coils are wired and interfaced with the ECT equipment. The mode of operation of a probe generally falls into four categories: absolute (single coil), differential (two coils wound in opposite direction), send-receive (separate coils for excitation and detection) and magnetic sensor as shown in Figure 1.10 [19].

For detection of sub-surface flaws, probe configuration, mode of operation and dimensions of probe play an important role. For different probe configurations and probe dimensions, the strength of

primary magnetic field is different. As a result they provide different effective depths of penetration of eddy currents into the test object.

In order to detect sub-surface flaws, large diameter and high throughput probes are required. In general, the probe diameter should be less than or equal to the expected length of the flaws in the material [3]. The sensing area of large diameter air core probes is very high due to the field spread. Hence, ferrite cored and shielded probes are preferred for focusing the fields for enhancing the detection sensitivity especially, for sub-surface flaws. The effective depth of penetration is not same for all types of probes. Hence, selection of suitable probe that ensures higher effective depth of penetration is important for detection of sub-surface flaws.

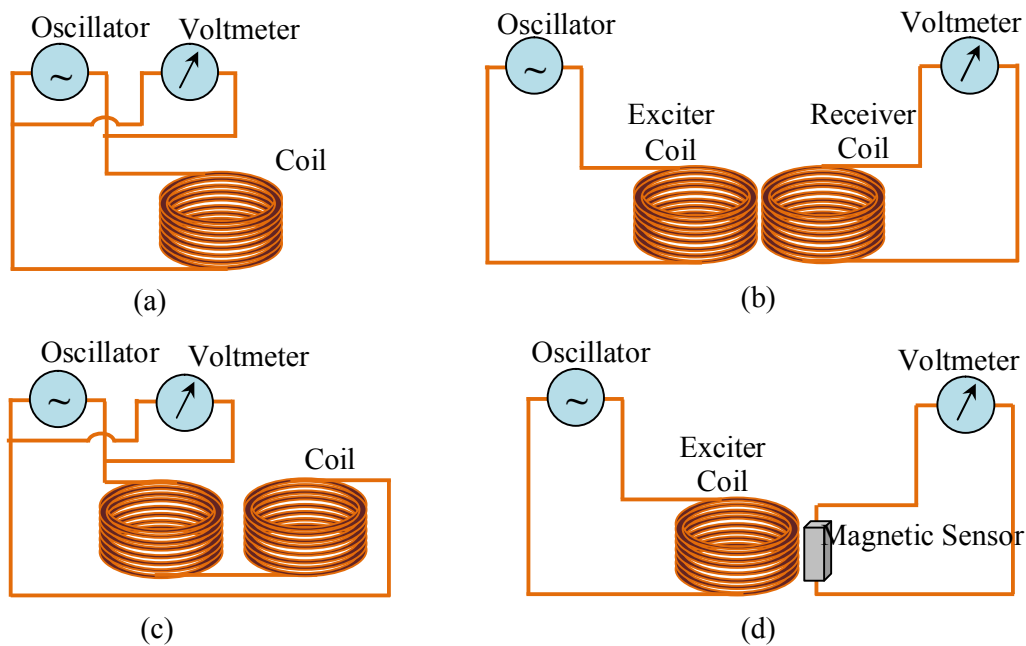


Figure 1.10: Mode of operation of EC probes (a) absolute (b) send-receive (c) differential (d) magnetic sensor.

1.3.4 Excitation field strength

The strength of the induced eddy currents is weak at higher depths, due to the exponential attenuation of the eddy currents. Hence, a very small change in impedance is produced from sub-surface flaws and this is difficult to be picked up by the EC probe. To overcome this, strengthening

of the primary magnetic field from the EC probe is beneficial and this can be achieved by increasing the excitation current as shown in Figure 1.11. By increasing the excitation current, the strength of the primary magnetic field at higher depths can be increased and this improves the effective depth of penetration as well as the coupling energy between the probe and test object. However, by increasing the excitation current, detection sensitivity increases, but it also causes heating of the EC probe. Hence, selection of suitable excitation current in the probe is important for detection of sub-surface flaws.

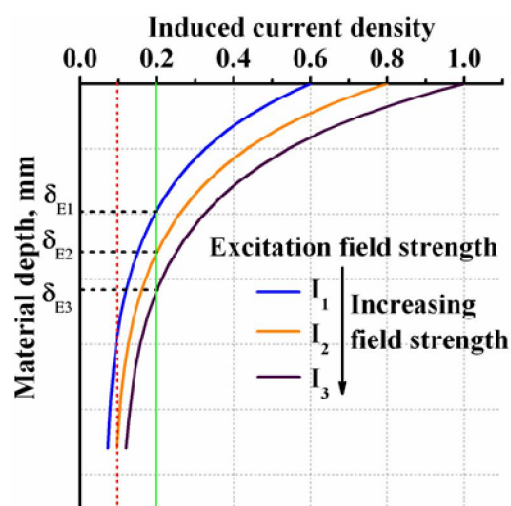


Figure 1.11: Effective depth of penetration for varying excitation current.

1.3.5 Reception unit

The reception unit consists of balancing circuit, amplifiers, filters and data acquisition card to prepare the signal for analysis and interpretation. The strength of the received signal from sub-surface flaws is usually feeble and dominated by the material, instrument or environment noise. Because of this, it is difficult to extract the information of flaws. In order to reduce this noise and to obtain the information of sub-surface flaws, design and use of high sensitive reception unit is important.

1.3.6 Processing of Signals and images

In order to minimise noise introduced in the EC signals due to surface roughness, probe tilt, variation in lift-off and instrumentation noise and also to extract useful information of flaws, various signal processing techniques are employed. These include use of filters, artificial neural networks, Fourier analysis, wavelet analysis, principal component analysis (PCA), multi-frequency analysis etc. [20,21,22,23].

The information obtained from a single line-scan of an EC probe is limited. In order to extract quantitative information of flaws imaging is essential and processing of eddy current images is important for removing noise, identification of regions of flaws and characterization of flaws. Use of several image processing methods time-based, frequency-based, wavelet based is common in ECT. For detection of sub-surface flaws, use of larger diameter probe excited with lower frequency is required. EC images of large diameter probes at lower frequency suffer from blurring or over sizing due to the large foot print or point spread function (*psf*) of the EC probe which decreases the resolution and SNR [3].

1.3.7 Fusion of images

NDE is an application field that lends itself naturally to data fusion largely because it involves the use of multiple sensors by different NDE techniques. NDE data fusion methods utilize the redundancy and complementary information from different sensors, frequency and techniques to enhance the resulting image. Image fusion is a process of combining relevant information from two or more images into a single image and the fused image is expected to be more informative than any of the input images. The reliability of ECT technique can be improved through the combination of redundant information, as well as through the fusion of complementary information. The redundant information is used to improve the SNR of the images and the complementary information is used to augment the overall information content, which in turn, increases the accuracy of sizing. NDE fusion

methods using a variety of signal and image processing techniques are useful to enhance the quality of images for detection and sizing of flaws.

Images generated by using different frequencies and probes have redundant and complementary information about a flaw. In this context, fusion of EC images obtained from different frequencies and probes is beneficial and is expected to enhance the detection sensitivity as well as SNR of images. Hence, fusion of flaw images is gaining importance in NDE domain. In various fusion methods available for fusion of eddy current images include multi-resolution based Laplacian pyramid, wavelet transform, statistical inferences based Bayesian, and linear transformation based principal components analysis (PCA) [24,25,26].

1.3.7.1 Laplacian pyramid based fusion

Burt and Adelson proposed Laplacian pyramid in 1983 [27]. Laplacian pyramid is a multi-resolution based image fusion method. Laplacian pyramid sub-samples the image into different resolution levels and for generation of this sub-sample images two operations viz. EXPAND and REDUCE are used.

REDUCE is used to construct the level 1 image I_1 by using a low-pass filter and decimation by 2 with $i = 0$ as the original image, I_0 . Higher level image I_i can be constructed using I_{i-1} as:

$$I_i = REDUCE(I_{i-1}) \quad (1.10)$$

This sequence of the images I_0, I_1, I_2, \dots is called the Gaussian pyramid. The function EXPAND is nothing but a reverse of the function, REDUCE and used for interpolation to expand the image size by twice as:

$$I_i = EXPAND(I_{i+1}) \quad (1.11)$$

Laplacian pyramid is a sequence of the residual images which is a difference of the expanded I_{i+1} image and image I_i as define by:

$$Residual_{i-1} = I_{i-1} - EXPAND(I_i) \quad (1.12)$$

The Laplacian pyramid images contain the information regarding the edges of the images and in case of ECT, the knowledge about the total area of flaws is important for flaw sizing [28]. Hence, Laplacian pyramid based image fusion is attractive for detection of sub-surface flaws. For fusion of images, Laplacian pyramid of two images can be fused by the pixel-based method and typical schematic diagram is shown in Figure 1.12. Reconstruction of the fused Laplacian pyramid images can be obtained by the combination of the expanded images and residual images as:

$$I_i = EXPAND(I_{i+1}) + Residual_i \quad (1.13)$$

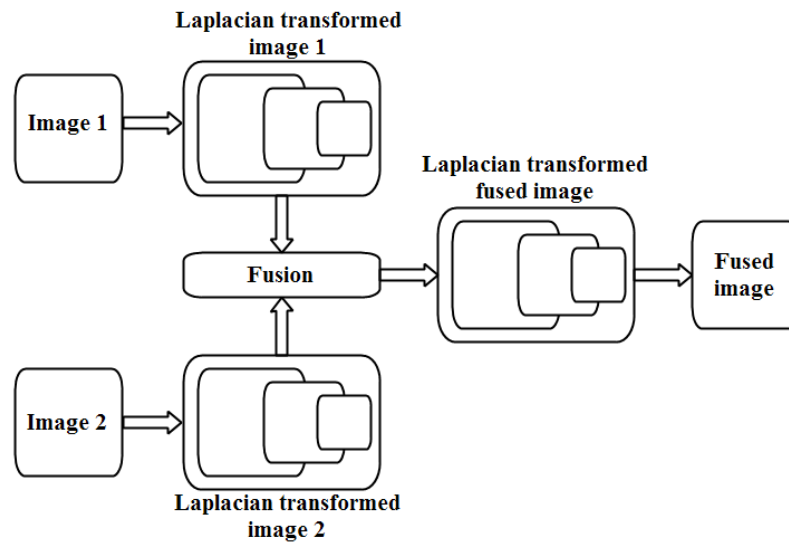


Figure 1.12: Schematic diagram of Laplacian transform based image fusion.

1.3.7.2 Wavelet transform based fusion

Wavelet transform decomposes an image into four coefficients namely, low-low (LL), low-high (LH), high-low (HL) and high-high (HH) by separately filtering and down sampling using the low

pass filter (L) and high pass filter (H) [29,24]. LL coefficient is a low frequency approximation (A) of image which contains less redundant information, while LH, HL and HH is high-frequency detail of image which represent horizontal (H_r), vertical (V_r) and diagonal (D) directional information due to the spatial resolution. Decomposition of an image I_i is performed by

$$T_i = W \times I_i \times W^T = \begin{bmatrix} A & V_r \\ H_r & D \end{bmatrix} \quad (1.14)$$

where I_i is the input image, W is the transformation matrix which is generated by the combination of the two convolution filter (L) and (H) as given by $W = [L \ : \ H]$ [30] and T_i is a wavelet transformed domain image.

Wavelet transform based fusion is widely used in NDE since it helps in capturing all the features in an image not only at different resolutions but also at different orientations. Fusion of input images is performed in wavelet transformed domain are shown in Figure 1.13. Coefficients of the images after transformation are fused together and inverse wavelet transform is used for reconstruction of the fused image by:

$$I_i = W^T \times T_i \times W \quad (1.15)$$

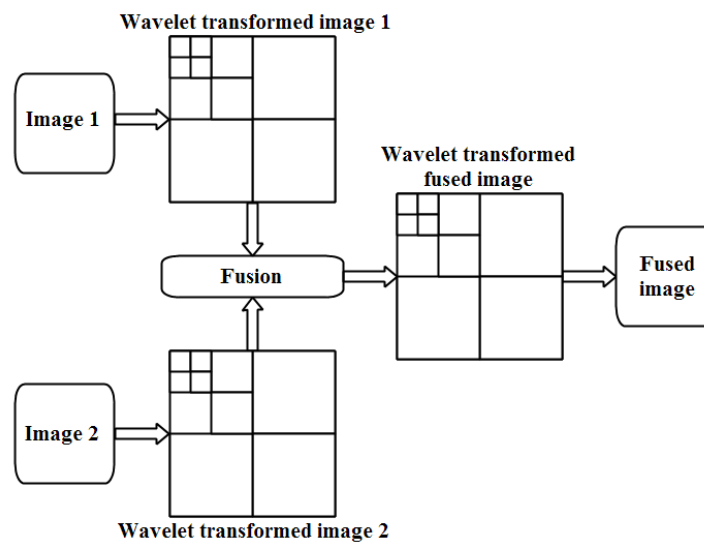


Figure 1.13: Schematic diagram of wavelet transform based image fusion.

1.3.7.3 Bayesian based fusion

Bayesian fusion works on the principle Bayes rule which is based on the statistical inferences and probability theory. Bayes rule divides the statisticians over the idea of how best to estimate an unknown parameter from a set of data [31]. For example, if it is desired to identify a flaw based on a set of measurements of useful parameters, from this data set one must extract the best value of some quantity. In order to achieve the best value, fusion method involves formulating the fusion problem in probabilities [32] and for this, the input images are assumed to be independent events with the likelihood of images $I_1 \dots I_N$ is given by

$$p(I_1, \dots, I_N | \theta) = \prod_{n=1}^N p(I_n | \theta) \quad (1.16)$$

where $p(\theta)$ is the prior and known knowledge about occurrence of flaw. The posterior distribution according to the Bayes principle, is given by

$$p(\hat{\theta} | I_1, \dots, I_N) \propto p(\theta) \prod_{n=1}^N p(I_n | \theta) \quad (1.17)$$

It is well know that in ECT, the image of flaw appears in the form of Gaussian function, as eddy current probe and point spread function are circular. Hence, formulation of the prior probability for Bayesian fusion normal Gaussian distribution with zero mean and unit standard deviation is moved over the input images to find the best fit Gaussian distribution matrix. The individual pixel values of the input images are taken as the likelihood and the posterior distribution gives the information about the features in the fused images.

1.3.7.4 Principal components analysis based fusion

Principal component analysis (PCA) is a linear transformation method which involves a mathematical procedure that transforms a number of correlated variables into a number of uncorrelated variables called principal components [29]. In general, the first principal component

collects the information that is common to all the frequencies used by input image in the PCA, i.e., the spatial information, while the spectral information that is specific to each frequency is picked up in the other principal components. In PCA, the covariance of an image matrix is computed and a subspace with larger Eigen values of covariance is retained. Covariance matrix (C_x) of the input image X can be calculated by:

$$C_x = \frac{1}{p-1} \sum_{i=1}^p \{(X_i - \mu_x)(X_i - \mu_x)^T\} \quad (1.18)$$

where μ_x is mean value of the input image X_i and define by:

$$\mu_x = \frac{1}{p} \sum_{i=1}^p X_i \quad (1.19)$$

The Eigen vectors of this matrix, if sorted, in descending order of Eigen values, the results will reveal the orthogonal basis with first Eigen vector having the direction of largest variance of the data and the matrix is called the orthogonal matrix A . The PCA transformation can be expressed as

$$Y = A(X - \mu_x) \quad (1.20)$$

Fusion of images is performed in this projected domain with fewer Eigen vectors are shown in Figure 1.14. In Figure 1.14 fusion block indicates the average of the PCA transformed images (Y_1 and Y_2). Finally, the inverse transformation is applied to get the fused image [33].

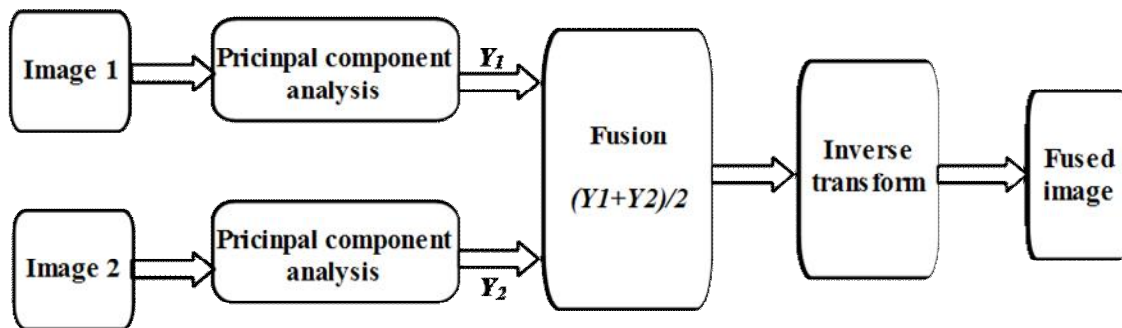


Figure 1.14: Schematic diagram for image fusion using principal component analysis [33].

$$X = A^T Y + \mu_x \quad (1.21)$$

1.4 Literature review

As discussed in Section 1.3, enhancement in detection of sub-surface flaws is possible by selection of suitable EC probes and optimization of test parameters. Several approaches including development of high throughput probes, better instruments and processing of eddy current signals and images have been attempted by many researchers earlier for enhanced detection of sub-surface flaws.

1.4.1 Eddy current probe

For detection of sub-surface flaws using ECT, it is important to design an optimum probe configuration. In this context, there is a strong need to study the different probe configurations to design a suitable probe for detection of sub-surface flaws. This could be accomplished either by experimentation or by numerical modelling. Various researchers studied different probe configurations and mode of operation for detection of flaws, flaw orientation, wall thickness etc [34,35,36,37,38,39]. ECT is used extensively for inspection of steam generator tubes in nuclear power plants. For inspection of steam generator tubes, different types of probes were used [40,41]. In the literature, use of air core, ferrite core, inductive, E-core, Double-D, cup-core type probe configurations was represented.

Palanisamy *et al* (1983) studied the influence of absolute EC coil with and without ferrite core (i.e. cup-core and air core) using finite element (FE) model for detection and characterisation of flaws in a disk bolt holes under a 1.27 mm SS sleeve. In this study, change in impedance of probe coil and distribution of eddy currents around a flaw in the second layer (1.27 mm below) of aluminium lap joint were predicted. They noted that the detection sensitivity of air core coil is higher for smaller coils (i.e. mean radius, $r_0 < 1.0 \text{ mm}$) and for larger mean radius ($r_0 > 1.0 \text{ mm}$), cup-core coil is

more sensitive than air core coil. They also reported that cup-core coil provides better signal resolution than air core coil due to the focused flux interaction [42].

Hoshikawa *et al* (1984) compared the performance of absolute and send-receive mode probes using FE model. For these studies 4.0, 10.0 and 30.0 mm diameter absolute single coil probe and send-receive mode double coil probe with 30.0 mm excitation coil and 4.0 mm pick-up coil were used. Cross section of these coils is shown in Figure 1.15. The change of impedance and induced voltage response of the probes were calculated as a function of lift-off variation and flat bottom hole depth as shown in Figure 1.16. It was found that for double coil probe the change of impedance and induced voltage due to lift-off and flat bottom hole depth was far larger than that of the absolute coil probe and send-receive mode double coil probe [43].

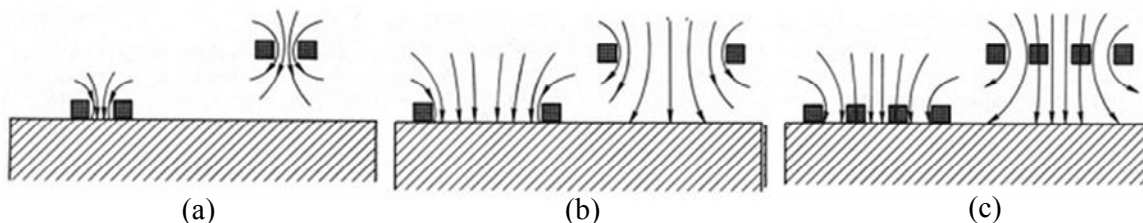


Figure 1.15: Cross section of surface probe over a conducting surface (a) small diameter single coil (b) large diameter single coil and (c) double coil probe [43].

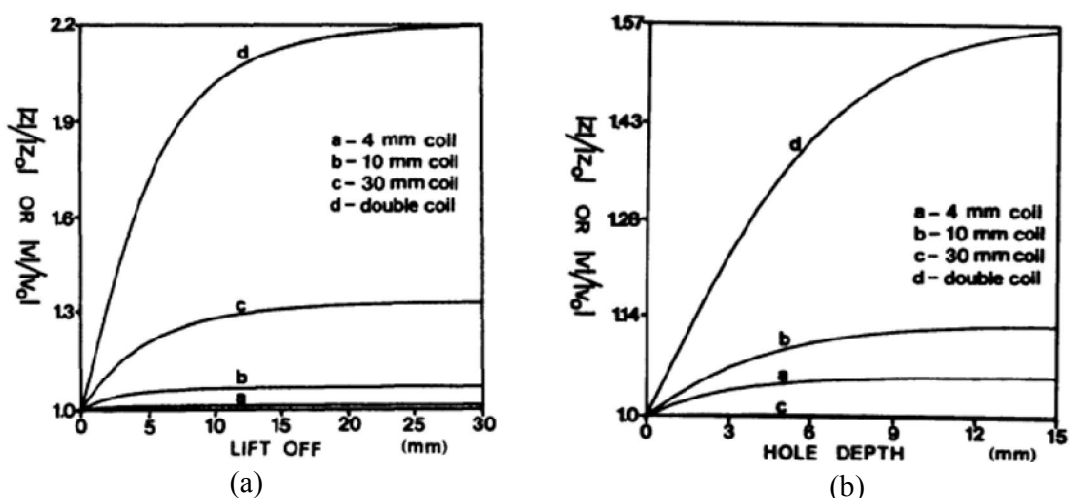


Figure 1.16: Predicted change rates of impedance and induced voltage due to (a) lift off change (b) flat bottom hole depth change [43].

Young *et al* (2009) studied the performance of four types of probes i.e. absolute air core, send-receive, shielded send-receive, and differential probe for detection of wall thickness variation using FE model. For this study, change in amplitude for thickness variation in the range of 1.0 mm to 5.0 mm for copper, tungsten and inconel 600 was predicted and found that all four types of probes showed similar characteristics. However, the shielded send-receive probe showed better sensitivity for wall thickness reduction as compared to other probes [44]. Hence, by using the send-receive mode probe, detection of sub-surface flaws can be enhanced.

Further, for detection of sub-surface flaws it is necessary to avoid direct coupling of the excitation field with the receiver coil. In the case of absolute type probe, avoiding direct coupling of the excitation field is not possible as the coil is same for exciter and receiver. But in the case of send-receive type probe, exciter and receiver coils are different and this will result in a very small output signal, thus maintaining high sensitivity to flaws in the object under test [18]. Hence, for detection of sub-surface flaws send-receive mode is more attractive than the absolute probe.

Sasi *et al* (2007) developed an integrated probe comprising of an exciter coil and a giant-magneto resistive (GMR) sensor for detection as well as imaging of deep surface flaws and far side corrosion in austenitic stainless steel. For these studies, EDM notches (length 8.0 mm, width 0.75 mm) located at 4.0, 5.0 and 5.25 mm below the surface in 6.0 mm thick austenitic SS plate and 24.0 mm diameter flat bottom holes of 2.0, 4.0, 6.0, 8.0 and 10.0 mm deep from far-side of 12.0 mm thick SS plate were used. EC response of the flaws was determined for the integrated probe and compared with that of the conventional EC probe (absolute). It was found that integrated probe showed better detection sensitivity than the conventional EC probe. The integrated probe could detect the notch located at 5.25 mm and a surface flat bottom hole located at 8.0 mm below the surface. The commercial EC probe detected only upto 5.0 mm below the surface as shown in Figure 1.17 [45].

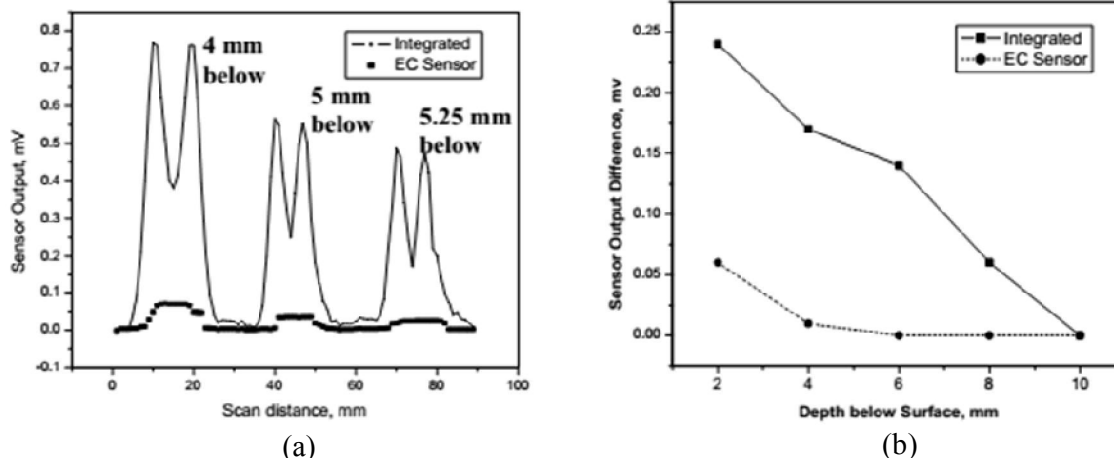


Figure 1.17: Response of integrated EC GMR sensor and pancake type absolute EC sensor signal from (a) EDM notches (b) the sensor output for flat bottom hole located at different depths [45].

Angani *et al* (2011) developed a differential Hall sensor based ferrite core probe for detection of sub-surface flaws in insulated thick SS pipes. In the differential probe, two Hall sensors were placed at top and bottom axial center of the excitation coil. For this study, SS plate of thickness 8.0 mm with artificial notches located at 1.0 mm to 5.0 mm below the surface was used. A plastic sheet with thickness of 4.0 mm was placed over the surface of the plate to simulate the thermal insulation of the pipeline [46]. A real time LabVIEW based scanning was used at 500 mA excitation current and response of the probe was acquired as shown in Figure 1.18. They reported that the differential probe had the potential to detect sub-surface flaws in insulated pipelines.

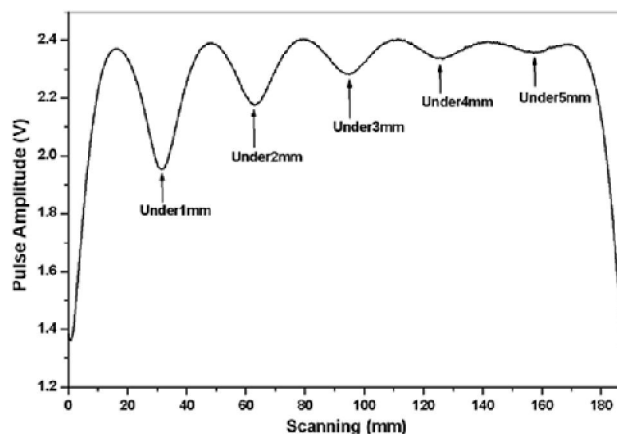


Figure 1.18: Differential Hall sensor probe response for sample having EDM notches at different depths [46].

It is noticed that solid state sensors are useful to improve the detection sensitivity. However, for use in radioactive conditions, solid state sensors such as Hall and GMR are not suitable, as they undergo radiation damage [47]. On the other hand, the traditional coil based eddy current probes are well suited, in view of their large dynamic range, good radiation resistance, slow degradation, better stability, and low-cost, despite their lower sensitivity as compared to the solid state sensors. Attempts have been made earlier by many researchers towards improving the sensitivity of the coil based probes by employing magnetic shielding and circuits. For analysis of ferrite core probes, FE model was used and induced current density and probe impedance were evaluated for performance assessment [48,49,50].

Vernon *et al* (1987) studied the influence of shielding on detection sensitivity by using self-shielding (by coil shielding) and imposed shielding (by ferrite core) configurations in absolute mode. Sensitivity of the probe was predicted in term of coupling coefficient between the probe and the material (aluminium and carbon/carbon). The coupling coefficient was calculated for lift-off variation and by changing the coil winding. It was found that the imposed shielding increases the sensitivity of the probe [51].

Joubert *et al* (2010) developed a cup-core probe with four flat pick-up array coils for detection of sub-surface flaws in rivets located 4.0 mm below the surface in a 10.0 mm thick aluminium plate [52]. The pick-up coils comprise of 32 turns distributed in 8 layers of printed circuit board (PCB) and cover an angular sector of 90 degrees. Differential trans-impedance of the probe due to sub-surface flaws was measured and it was noted that the cup-core array probe showed good sensitivity for flaws oriented at different angles.

From the literature, it is learnt that the send-receive mode probe coil appears good for detection of sub-surface flaws in austenitic SS. Shielding of the probe is expected to provide better coupling between the probe and test object.

1.4.2 Eddy current instrumentation

In addition to the development of high throughput probes, enhanced detection of sub-surface flaws is possible by using high sensitive instruments. Several researchers reported development and use of improved EC instruments to increase the detection sensitivity to surface and sub-surface flaws [53,54,55].

Dario *et al* (2012) developed two low-cost EC instruments for detection of sub-surface flaws. In the first system (system A), they used GMR planer probe with sine-fitting algorithm based positioning system as shown in Figure 1.19 and in the second system (system B) GMR vertical probe with microcontroller based analog processing block was proposed to retrieve the amplitude and phase shift of the probe response. Flaws (1.0 mm wide and 20.0 mm long) located at 1.0, 1.8 and 3.0 mm below the surface in aluminium plate were used. Performance of the developed systems was compared with that of a commercial system (ELOTTEST B300 produced by Rohmann GmbH). They reported that the signatures obtained from both the developed systems showed the same flaw pattern as produced by the commercial system. Figure 1.20 shows the typical signature obtained by the system A for a flaw placed 3.0 mm deep below the surface at three excitation frequencies. They also noted that the developed systems have the ability to detect sub-surface flaws as compared to the commercial system [56].

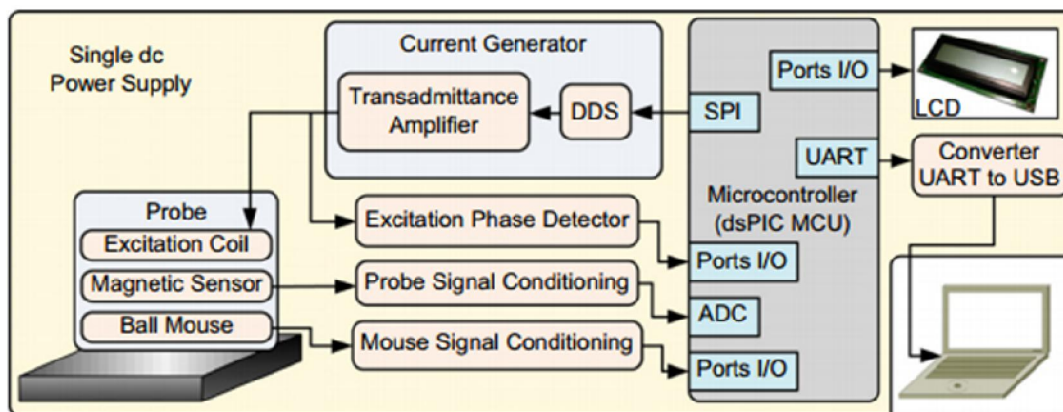


Figure 1.19: The architecture of the developed system A [56].

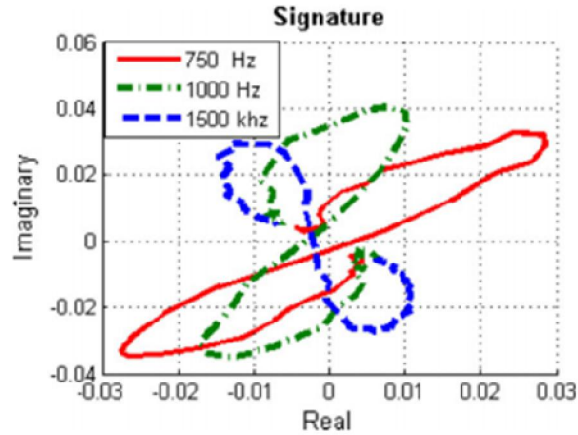


Figure 1.20: Signature EC signals obtained by the system A for a flaw at three excitation frequencies [56].

Wang *et al* (2013) developed a field programmable gate array (FPGA) based EC system for detection of flaws through measurement of phase and amplitude information. The FPGA chip is used for coil excitation as well as for demodulation of the response of the EC probe. Using the FPGA based demodulation, amplitude and phase response of the EC signal could be realized at the same time for high speed performance. In order to check the performance of the developed system, experiments were carried out on flaws (20.0 mm long and 7.0 mm deep and 6.0, 8.0 and 10.0 mm wide) using a GMR based probe at frequency 1 kHz. It was found that the phase information correlated well with the flaw size than that of the amplitude [57].

Naveen *et al* (2006) developed GMR based eddy current system for detection of flaws in aircraft structures. They used an analog in-phase/quadrature (I/Q) detection scheme to determine the amplitude and phase of the probe response. Figure 1.21 (a) shows the schematic of the I/Q detection scheme. It was shown that the I/Q detection based system obtained the quantitative information about the magnetic field of the flaws with high sensitivity. They compared the I/Q detection scheme with sample-stop-sample scheme and reported that I/Q detection scheme provides better resolution images with fast scanning speed as compared to the traditional sample-stop-sample scheme as shown in Figure 1.21 (b-c). This is because of I/Q detection scheme used input data collection in analog

manner. On the contrary, the sample-stop-sample scheme required the scanner to stop at each sample point. They also reported that by using the I/Q detection scheme sampling at higher rate was not necessary [58].

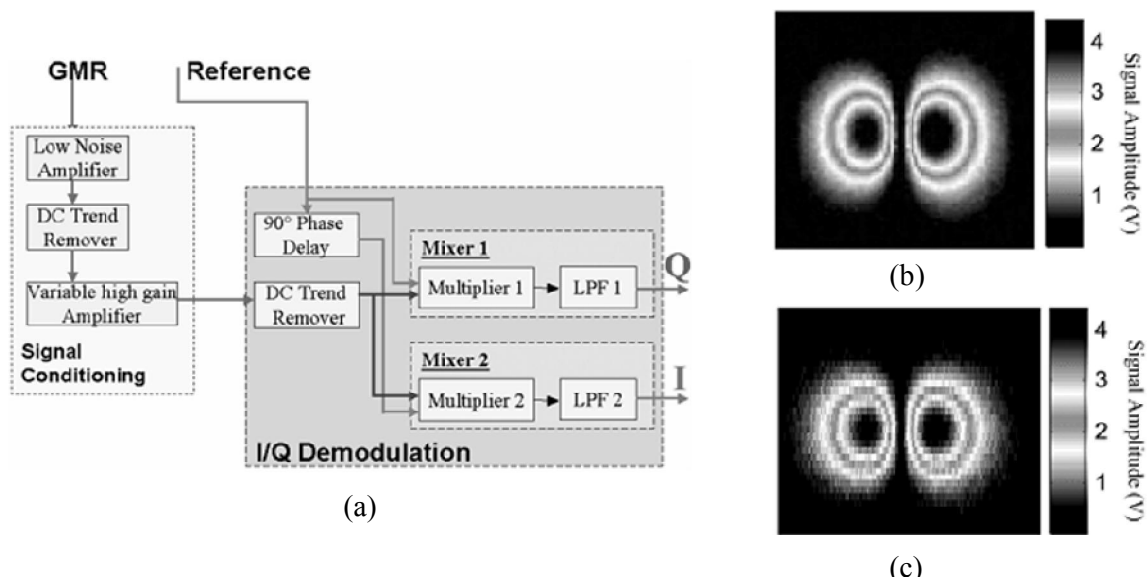


Figure 1.21: (a) Schematic of I/Q detection scheme. EC images obtained using (b) the I/Q scheme (c) traditional sample-stop-sample scheme [58].

Clarkson *et al* (2010) implemented I/Q detection based digital lock-in amplifier using LabVIEW software to examine the sine wave component from a noisy signal, to investigate simulated signal faster and repeatable and finally, to implement a generalised approach to use directly other measuring system. Using the digital lock-in amplifier, information about the phase and amplitude of the sine wave signal could be determined without any assumption. It was found that the use of lock-in amplifier permitted the dependence of accuracy of the results on quantization (N_b), sampling frequency (f_s) and the duration of the signal (T) which result in high resolution output signal [59].

From the literature, it is inferred that phase measurement is important in ECT for detection of flaws, because it gives useful and important information about the shallow surface flaws as well as deep sub-surface flaws. In the case of sub-surface flaws, the strength of the EC signal is feeble and hence, for enhancing this feeble signal, development of high sensitive measuring instrument is essential.

1.4.3 Signal and image processing

1.4.3.1 Signal processing

Doctor *et al.* proposed non-parametric classification methods based on feature-extraction techniques, which first create a feature vector containing elements drawn from time, frequency and spatial domain and then apply pattern recognition methods for classification of flaws [60]. Udpa *et al.* used a few invariant Fourier descriptors to estimate depth of flaws in heat exchanger tubes and under support plates with reasonable success [61]. Shyamsunder *et al.* used the time-domain and the frequency-domain parameter of signals from line scans in different orientations for classification of surface flaws. The best parameters were chosen by using a Fischer statistical ranking and classification was carried out using an artificial neural network [62]. Joubert *et al.* proposed principal component analysis and independent component analysis based signal processing approaches for improvement in detection of sub-surface flaws [52]. Thirunavukkarasu *et al.* used Fourier filtering, cross-correlation, and continuous wavelet transform based techniques for detection of flaws in expansion bend regions of modified 9Cr–1Mo steam generator tubes of sodium cooled fast breeder reactor. They found that Fourier filtering, cross-correlation techniques can reduce the noise and detect 20% wall thickness grooves in tube. They reported that continuous wavelet transform based technique unambiguously detected 10% WT deep grooves present anywhere in the bend regions with a SNR better than 7 dB [20].

1.4.3.2 Image processing

Xiang *et al.* implemented an automated signal analysis algorithm for eddy current data from steam generator tubes. The algorithm converts the data into a visually appealing format and analyses it to determine the presence or absence of flaws. They also proposed a blind deconvolution algorithm to detect and accurately size flaws [21]. Kalyansundaram *et al.* proposed an Eigen value based approach for enhancement of eddy current images. In this approach, Eigen pairs having maximum

information of the impedance change due to the flaws are determined using image covariance matrix and utilized to reconstruct noise-free images [63]. Chady *et al* reported a multi-frequency excitation and spectrogram (MFES) eddy current system and an inversion model to detect flaws in a 1.23 mm thick Inconel 600 plate [64]. Cacciola *et al* proposed a hybrid wavelet transform and independent component analysis based approaches to reduce the lift-off noise in eddy current images. They reported that the hybrid approach ensures SNR enhancement of 0.063dB and 2.238 dB as compared to WT and ICA respectively [65].

1.4.3.3 Image fusion

Mina *et al.*(1996) proposed a fusion method that uses the real and imaginary component images of artificial cracks around rivet holes in an aluminum specimen. Multi-frequency ECT was applied to inspect surface and sub-surface flaws on aluminum specimen and fusion was implemented in the frequency domain with the discrete Fourier transform. The fusion process was based on the spectrum of the acquired images, where the linear minimum mean square error (LMMSE) approach was adopted to fuse the images using a weighting scheme to achieve a better SNR [66,67].

Gros *et al* (2000) used Bayesian analysis, Daubechie wavelet, steerable pyramid transform and multi-resolution mosaic based image fusion methods to combine eddy current and infrared thermographic images from carbon fiber reinforced plastic (CFRP) composite panels. They observed that data fusion increased the knowledge about flaw location and size. They also reported that more advanced fusion techniques may be developed for a specific NDE application to reduce the uncertainty and increase the overall performance of NDE [68].

Zheng *et al.* (2007) reviewed the progress in NDE data fusion techniques and examined the different mathematical fusion algorithms such as multi-resolution approaches, heuristic methods, probabilistic methods, and scientific visualization. They reported that with the evolution of advanced sensor technologies, there is a need to fuse the sensor and inspection data for in-situ monitoring of the

performance of structures and materials in real time. They also reported that development of efficient algorithms is essential for dealing the large amount of data from sensory, measurements, and stored data [69].

Ayed (2009) studied different fusion techniques for enhancement of electromagnetic NDE images. Ayed proposed the intensity hue saturation (IHS) and improved IHS with principal component analysis and wavelet decomposition based image fusion methods. For evaluation of the proposed fusion method, Ayed generated images from conventional EC, pulsed EC and optical NDE techniques by using FE modelling and experiments. Various quality metrics i.e. SNR, standard deviation, entropy etc. were used for assessing the fusion performance [70].

Sasi *et al.* (2012) proposed a fusion method based on discrete wavelet transform for eddy current images of simulated notches obtained at 325 kHz and 75 kHz frequencies from stainless steel cladding tube. They reported that proper selection of wavelet and decomposition level ensures removal of disturbing (noise) signal from periodic wall thickness variation and retains the flaw information [24]. They also proposed two new parameters viz. energy risk factor and weighted risk factor for fusion of the eddy current images.

Details of NDE fusion methodologies developed earlier are summarized in Table 1.1.

1.4.4 Rapid detection and imaging

ECT of plates is performed by scanning an EC probe over surface of the plate and observing the resulting impedance changes of the probe coil. ECT of large size components and structures in radioactive environment, demands rapid scanning to reduce the radiation dose to the inspection personnel, at the same time, ensuring 100% coverage of the component surface without compromising the detection sensitivity. For systematic coverage of the entire surface of the plate, raster scanning is usually performed with specified step size and area coverage.

Table 1.1: NDE fusion methodologies.

NDE techniques	Input image type	Fusion methods	Achievements and contribution	References
ECT	Real and imaginary component of surface flaws using multiple frequency	Discrete fourier transform	Image enhancement	Mina <i>et al.</i> 1996, 1997 [66,67]
		Discrete cosine transform		
		Linear minimum least mean square error		
	Multiple eddy current images	Dempster-Shafer	Improvement in signal interpretation and flaw detection	Gros <i>et al.</i> , 1994, [25]
ECT	Multiple frequency cladding tube surface flaws	Wavelet transform	Image enhancement	Sasi <i>et al.</i> , 2012 [24]
		Spatial frequency	SNR enhancement	Prachetaa <i>et al.</i> , 2010 [26]
		Wavelet transform		
ECT and ultrasonic testing	Surface flaw images using eddy current and ultrasonic testing	Bayesian method	Image enhancement	Udpa <i>et al.</i> , 2006 [71]
		Dempster-Shafer		
		Q-transform		
ECT and ultrasonic testing	Surface flaw images using eddy current and ultrasonic testing	Neural network	Preprocessing data from multiple sensors	Udpa <i>et al.</i> , 2006 [71]
		Morphological image processing	Classification of images for flaw and flaw-free case	

		Bayesian method		
ECT and infrared thermography	Images of carbon fiber reinforced plastic (CFRP) composite panel	Dempster-Shafer Wavelet transform Steerable pyramid	Knowledge about flaw location and characterization	Gros et al., 1996 [72]
X-ray and ultrasonic testing	Image of fiber reinforced composite materials	Image segmentation and analysis	Information about flaw size	Jain et al., 1991 [73]
		Intensity hue saturation		
Conventional ECT and pulse ECT	Image of surface and sub-surface flaws	Improved IHS with principal component analysis Improved IHS with and wavelet decomposition	Image enhancement	Ayed, 2009[70]
	Surface images of lap Joints corrosion	Dempster-Shafer	Estimation of the remaining thickness	Z. Liu et al., 2006 [74]
X ray radiography	X ray radiographic images at different view angle	Bayesian method	Image enhancement	Djafari et al., 2003 [32]
Radiography and ultrasonic testing	Images of weld flaws	Dempster-Shafer	Flaw detection and sizing	Dupuis et al., 1999 [75]
GPR and Infrared thermography	Near surface flaw image in concrete	Clustering-based	Flaws classification	Patricia et al., 2014 [76]
Pulsed ECT and Ultrasonic testing	Pulsed eddy current and Ultrasonic signals from aluminum alloy 2024 specimen	Fuzzy logic	Stress measurement	Habibalahi et al., 2014 [77]

Rao *et al.*, (2013) explored scanning techniques for enhanced imaging using different NDE techniques (ultrasonic, eddy current, magnetic flux leakage and microwave). They compared the performance of raster scanning using single absolute EC probe and line scanning using 8 coil based array type EC probe imaging of flaws. They reported that, array type probes are advantageous for faster detection of flaws. However, raster scanning should be performed for accurate sizing of flaws [78].

Mook *et al.*, (2011) developed a modular probe array for eddy current imaging of flaws. They studied the point spread function of absolute and send-receive mode array probes and noted that send-receive mode type of array probe results in high spatial resolution. For experimental studies, array probe with 32 absolute and 64 send-receive mode coils was fabricated for detection of the hidden flaws (varies from 0.1 to 0.5 mm below the surface) in aluminium plate and are shown in Figure 1.22. It was reported that the array sensor enhanced the visualization of hidden flaws in aluminum sheet with less inspection time [79].



(a)

(b)

Figure 1.22: (a) Array probe with 32 absolute coils and (b) array probe 64 send-receive mode coils [79].

Although there are a few advantages of using array type probes for imaging, there exist certain drawbacks which limits their wide spread use. The drawbacks of the array probes are [80]:

1. Difficulty in manufacturing identical probes for effective imaging
2. Requirement of large number of probes to cover the scanning area
3. Lower sampling rate due to multiplexing
4. Software complexity for initial setup
5. Higher cost

This calls for the development of rapid scan plans to cover 100% surface area with less time using a single EC probe without compromising the probability of detection and sizing accuracy. Hence, it is attractive to study various scan plans using single coil probe for rapid and reliable imaging of flaws. As raster scanning is time consuming to cover 100% surface area and tedious, studies have been carried out by researchers to reduce the scanning time without compromising the probability of flaw detection.

It is interesting to observe from literature that rapid detection and imaging of flaws is possible by scanning with single EC probe using different scan plans followed in other imaging domains such as microscopy, and astronomy [81,82,83,84].

Rao *et al* (2001) proposed an intelligent imaging scheme shown in Figure 1.23 using artificial neural network for fast and automated detection, imaging and characterization of surface-flaws in 3.0 mm thick stainless steel plates using a single coil probe. Binary images were obtained at coarse step size of 1.0 mm and flaw region were localized and this localized region was subjected to fine scan with a step size of 0.3 mm to obtain high resolution images by using separate artificial neural networks for linear and circular flaws. Typical result of this intelligent imaging scheme is shown in Figure 1.24. They reported an approximately ten-fold reduction in inspection time [85,23].

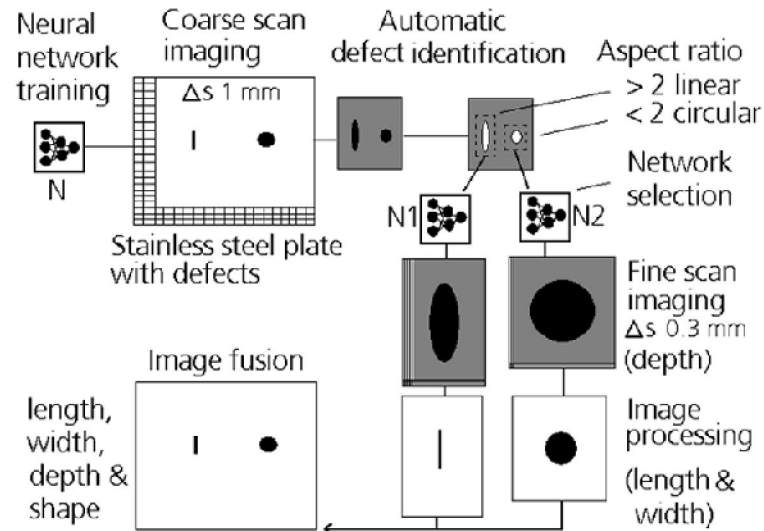


Figure 1.23: The intelligent eddy current imaging scheme developed for quick and automated detection and characterization of flaws [85].

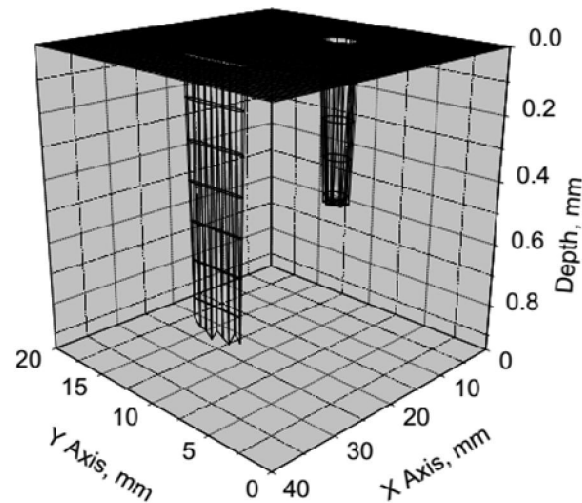


Figure 1.24: Three dimension image obtained by the intelligent imaging for a stainless steel plate consisting of a notch (length 3.0 mm, width 0.3 mm and depth 0.8 mm) and a flat bottom hole (diameter 1.5 mm and depth 0.5 mm) [85].

1.5 Summary

Eddy current testing technique is used in aerospace, nuclear, petrochemical and other industries in view its excellent detection sensitivity for surface as well as near sub-surface flaws. ECT is, in general, confined to detection of sub-surface flaws within a depth of 5.0 mm in austenitic stainless

steel plates. Since, many components used in nuclear industries made of thicker stainless steels in the range of 8.0 mm to 12.0 mm, such as a storage tank and dissolver vessels, ECT of these components from outside is desired due to the radioactive environment. Rapid detection and imaging of inside surface flaws (deep sub-surface) from the outer surface is a challenge. For detection of sub-surface flaws by ECT technique, it is essential to give due consideration to excitation frequency, excitation current, probe configuration, measurement instrument, and electromagnetic coupling imaging and image processing.

Motivation and Objective

2.1 Preamble

This chapter identifies the gap areas based on the literature, which have helped in setting the motivation and in identifying the objectives of the research work. This chapter also outlines the organization of the thesis.

2.2 Motivation for research

Austenitic stainless steel is one of the important core structural materials used in nuclear, chemical and petrochemical industries. These steels are subjected to eddy current testing for quality assessment and in-service inspection requirements. This technique is efficient in detecting surface as well as near sub-surface flaws reliably. Due to the *skin-effect*, induced current density in the material attenuates exponentially and this limits the sensitivity to detect flaws located upto 5.0 mm below the surface. Detection of deep sub-surface flaws in austenitic stainless steels by ECT technique is challenging. Research efforts towards enhancement of sensitivity to detect deep sub-surface flaws in thick stainless steel plates using the ECT technique are worth focusing and exploring.

By changing the test parameters and conditions, the detection sensitivity of ECT technique can be increased. The possible ways for enhancement of detection sensitivity are:

- Increasing the depth of penetration (strengthening the primary magnetic field)
- Development and use of high sensitive instrument and probes
- Development and use of signal and image processing methodologies

As observed from the literature, by using high throughput probes and using higher excitation current, effective depth of penetration into stainless steel can be increased. Inspired by the encouraging performance of the send-receive probe in the literature over the absolute probe, studies can be focused on exploring the send-receive mode EC probes. It is also interesting to observe from the literature that performance improvement of the EC probes is possible with the use of ferrite core and shielding, especially send-receive type cup-core probes. In radioactive environments, the coil based probe seems to be attractive for ECT of thick SS because solid state sensors undergo the radiation damage. The existing literatures do not address detection of sub-surface flaws located beyond 5.0 mm in stainless steel components. Hence, there is strong need to optimize and design send-receive type ferrite cored coil probes for detection of sub-surface flaws and corrosion damage in austenitic stainless steel components.

Commercially available EC instruments have limitation for detection of flaws due to lower excitation current levels and lack of precise measuring instruments for detection of feeble response from sub-surface flaws. As observed from the literature, excitation current is important for strengthening the primary field. Hence, development of a higher variable excitation current source based excitation unit is attractive. To receive the feeble response from sub-surface flaws, development of a high sensitive measurement system (of the order of μV) is essential. Although it is known that phase measurement gives information about the depth of flaws, use of phase measurement in ECT is very limited for sub-surface flaw detection. Hence, for detection of deep sub-surface flaws in thick austenitic stainless steel development of a high power and high sensitive precise phase measurement instrument is an attractive option.

EC imaging is essential for automated detection of flaws. EC images of large diameter probes suffer from blurring due to the large foot print or point spread function (*psf*) of the EC probe. In this context, it may be beneficial to adopt image processing techniques to improve the detection sensitivity of sub-surface flaws. In the open literature, a variety of image processing methods viz.

image denoising, filtering, pattern recognition, etc. have been reported. Inspired by the encouraging performance of fusion of eddy current images in the literature, along with the recent developments in the field of enhancement and denoising the EC images of surface flaws, studies can be focused on exploring the image fusion methods for the enhancement of EC images of sub-surface flaws. The image fusion methods reported in the literature, however, are limited to detection of surface flaws. Details of image fusion methodologies for detection of sub-surface flaws in austenitic stainless steel are not found in the open literature. Hence, development of image fusion methodologies can be explored for detection of sub-surface flaws and improve the SNR.

For automated EC imaging of components for detection of flaws using a single sensor, raster scan plan is used and it is time consuming. Alternative methods proposed in the literature use array probes. Although, array probes are preferred for faster imaging, they require multi-channel systems and data acquisition modules and are expensive. For detection and imaging of the flaws fast scanning using single probe is still attractive. Development of efficient alternate fast scan plans to reduce the time required for EC imaging without compromising the flaw detection performance is worth exploring, specifically to use in radioactive conditions.

2.3 Objective of research

The primary objective of the thesis is detection of deep sub-surface flaws in thick austenitic stainless steel plates. Based on the inputs gained from the literature, the following objectives have been arrived for automated rapid detection of deep sub-surface flaws:

1. To design and develop a high throughput eddy current coil based probe for detection of deep sub-surface flaws in thick AISI 304L austenitic stainless steel plates (thickness of 12.0 mm).
2. To develop high sensitive eddy current instrument for detection of deep sub-surface flaws.

3. To develop image fusion methodologies for improvement of SNR and probability of detection of surface as well as deep sub-surface flaws and study the comparative performance of different image fusion methods towards selection of an optimal methodology.
4. To explore possible alternative fast scan plans for a single coil based probe for rapid and automated detection and imaging of sub-surface as well as surface flaws.

2.4 Organization of the thesis

The thesis has been organized in four major chapters addressing the set objectives, towards establishing methodologies for detection of sub-surface flaws in austenitic stainless steels, as given below:

Chapter 3 presents the finite element model based probe optimisation methodology for designing a high throughput probe for detection of sub-surface flaws. For this study, four possible different probe configurations have been analysed for selection of the optimum configuration. This chapter also discusses a study on the dimensions of the optimum probe configuration and frequency selection.

Chapter 4 explains the design and development of a high sensitive eddy current instrument for detection of sub-surface flaws. This chapter also discusses the performance assessment of the developed EC instrument for detection of sub-surface as well as surface flaws in 12.0 mm thick austenitic stainless steel plates.

Chapter 5 discusses the development of a novel image fusion methodology for enhanced detection of sub-surface flaws. The comparison of the proposed image fusion methodology with existing image fusion methodologies in ECT based on the different quality assessment parameters is undertaken in this chapter.

Chapter 6 explains the importance of rapid detection and imaging of flaws in ECT. This chapter presents the simulation results of different scan plans and compares their performance with the conventional raster scan plan. This chapter also discusses the experimental investigations carried out to study the influence of flaw dimensions and scan step size on flaw detection.

Chapter 7 summarises the major conclusions drawn from the research work and provides the scope for future research.

Design and development of eddy current probe

3

3.1 Preamble

The scope of this chapter is to study the design optimisation of eddy current probes for detection of deep sub-surface flaws in thick austenitic stainless steel plates. The chapter discusses different types of send-receive type probe viz. air core, ferrite core, ferrite core with outer shielding and cup-core probes and comparison of performance of these probes using model predicted parameters viz., magnetic flux density, eddy current density and change in phase angle. Subsequently, for detection of sub-surface flaws, selection of optimum probe diameter and excitation frequency is discussed in this chapter.

For detection of deep sub-surface flaws, optimisation of probe configuration that strengthens the primary magnetic field for higher penetration into the material is essential. Practically, fabrication of different types of probes for selection of optimum probe by experimentation is time consuming and expensive. In view of this, finite element (FE) modelling is used in this study.

3.2 Finite element modelling

FE modelling was first proposed in the 1940s [86] and its use began in the 1960s for structural and continuum mechanics and later found a wide variety of applications in electromagnetic field problems [87]. Subsequently, FE Modelling has also been exploited well by NDE research community [10,88,89]. Today, the FE Modelling has become a powerful tool for designing eddy current probes for varied test situations.

In a FE model, the governing partial differential equation is solved in the problem domain. The problem domain is discretised into a number of composite sub-domain called elements which make up a mesh. In 2D axi-symmetry models triangular elements are widely used. The interconnecting points of elements are called nodes. The exact variation of the unknown function (e.g. potential) is approximated by a simple interpolation functions with unknown coefficients at each nodes associated with the elements. In other words, the original boundary value problem with infinite degrees of freedom is transformed into a problem with finite degrees of freedom. Then, a system of algebraic equations is obtained by applying the Ritz variational or Galerkin procedure and solution of the boundary value problem is obtained by solving the system of equations. Finally, the desired parameters such as potential, field, current density etc. are computed at the nodes situated within the region of interest [10,90].

For FE model based optimisation of eddy current probe configuration, COMSOL multi-physics 4.4 software is used in 2D axi-symmetry environment. State-of-the-art solvers are embedded in the package for the user to address complicated problems quickly and accurately [91]. For numerical simulation of model in COMSOL, suitable governing partial differential equations are formed and used.

3.3 Governing equations for eddy current testing

The governing partial differential equation of the ECT technique is derived from the Maxwell's equations given below [7,10,86]

$$\nabla \times E = - \frac{dB}{dt} \quad (3.1)$$

$$\nabla \times H = J + \frac{\partial D}{\partial t} \quad (3.2)$$

$$\nabla \cdot B = 0 \quad (3.3)$$

$$\nabla \cdot D = 0 \quad (3.4)$$

where E is electric field, B is magnetic flux density, H is magnetic field intensity, J is current density and D is the displacement current. In equation 3.2 the displacement current term can be ignored as it is insignificant in quasi static cases (equation 3.4). From the equation 3.3 the divergence of B is zero, so B can be expressed as the curl of another vector called the magnetic vector potential, A defined as:

$$B = \nabla \times A \quad (3.5)$$

The governing partial differential equation which is used for solution of eddy current FE model is derived by using Maxwell's equations and the constitutive relation $B = \mu H$ and $J = \sigma E$ and given as:

$$\nabla \times (\nabla \times A) = j\sigma\omega A - \sigma\nabla V + J_s \quad (3.6)$$

where V is the electric scalar potential, σ is the electrical conductivity, μ is magnetic permeability, ω is angular frequency of the sinusoidal excitation and J_s is the applied source current density.

3.4 Finite element model for eddy current testing

In COMSOL software by using the 2D axi-symmetry model, solution will be fast and accurate as finer mesh density is possible and propagation errors are less. Therefore, for the chosen EC probe type with cylindrical symmetry, 2D axi-symmetry model is selected for optimization of the EC probe configuration and dimension. The FE modelling steps involved using COMSOL are discussed in this section.

3.4.1 Construction of model geometry

In 2D axi-symmetry models a quarter of the problem domain is projected onto a 2D plane. Modelled geometry consists of EC probe and austenitic stainless steel plate enclosed in an

outer boundary. The model is truncated into a finite region by defining an external boundary model which limits the solutions to be calculated inside the assigned region. Dirichlet boundary condition ($A=0$) has been applied at the line of symmetry and at the outer boundary. Table 3.1 gives the details of sub-domain parameters values i.e. μ and σ used in the model. The conductivity of air sub-domain is set to a non-zero value to avoid computational problems typically encountered during FE solution, when dependent variable vanishes [92]. The typical geometry of model with a boundary region is shown in Figure 3.1

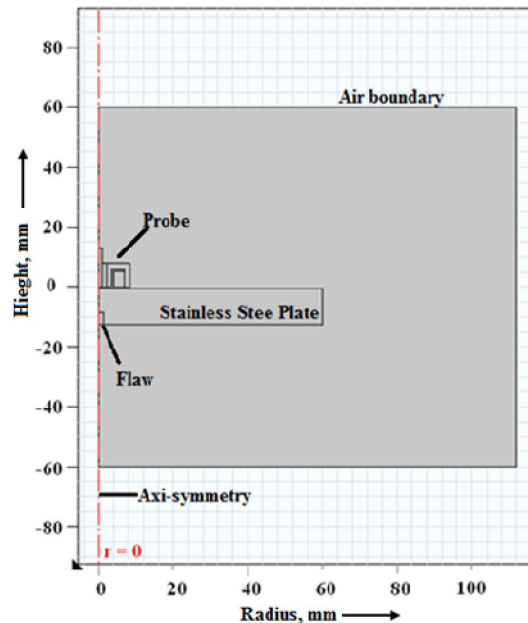


Figure 3.1: The typical geometry of model with a boundary region.

Table 3.1: Details of the sub-domain parameters used in the FE model.

S. No.	Material	Conductivity (σ), S/m	Relative magnetic permeability (μ_r)
1.	Air	10	1
2.	Copper	5.88×10^7	1
3.	Ferrite	100	1500
4.	Stainless steel	1.38×10^6	1

3.4.2 Meshing

In the model geometry, the region of interest is divided into a mesh of triangular-shaped elements. Higher accuracy is obtained by the generation of a fine mesh within the region of interest. SS plate with flaws and EC coil are the important regions to visualise the field distribution and hence, these regions are set at a more refined mesh. In the modelled geometry a total of 154378 triangular elements have been generated. 44 mesh layers have been chosen along the material thickness of 12.0 mm. This enhances the mesh quality around the flaw and the surrounding region where the direction or the magnitude of the magnetic field changes rapidly. Figure 3.2 shows discretisation of the mesh.

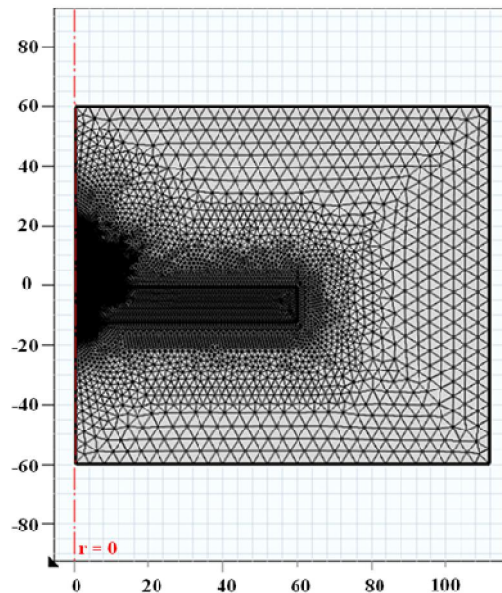


Figure 3.2: Discretisation of triangular mesh in the modelled geometry.

3.4.3 Equation solving

The generated geometry is solved by using the governing partial differential equation 3.6. This governing equation is complex and symmetric in nature. Hence, the complex symmetric version of the Multifrontal Massively Parallel sparse direct Solver (MUMPS) is used. MUMPS ensures faster computation with minimal storage. For solving a typical problem

having 154378 degrees of freedom, 8s time is required by the solver in work station (configuration are Pentium 4, 1.6 Ghz clock speed and 8 GB RAM).

3.4.4 Post-processing

Post processing is performed to calculate the magnetic flux density, induced current density, induced voltage in coil from the model predicted vector potential data [10]. The typical surface plot of magnetic flux density (B) with contour of induced current density (J_e) is shown in Figure 3.3. Data from the plots can be used for detailed analysis and understanding the field-flaw interactions.

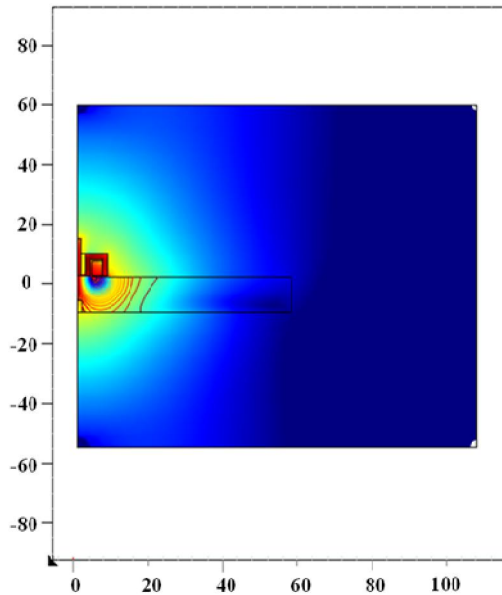


Figure 3.3: Typical surface and contour plot of magnetic flux density and induced current density.

3.5 Model based optimisation of probe configuration

As discussed in Section 1.3.3 and Section 1.4.1, a variety of probe configurations like absolute probe, differential probe, send-receive probe etc. are commonly used and optimisation of probe configuration is important. In this regard, send-receive type EC probes of different configurations viz. air core, ferrite core, ferrite core with outer shielding and cup-core have been

studied using the FE model. Figure 3.4 shows the cross-section of four different configurations of send-receive type EC probes considered in this study. They are

- (a) Air core probe with separate exciter coil and receiver coil,
- (b) Ferrite core probe with exciter coil and receiver coil without shielding,
- (c) Ferrite core probe with exciter coil and receiver coil with outer ferrite shielding and
- (d) Ferrite cup-core probe with separate exciter coil and receiver coil.

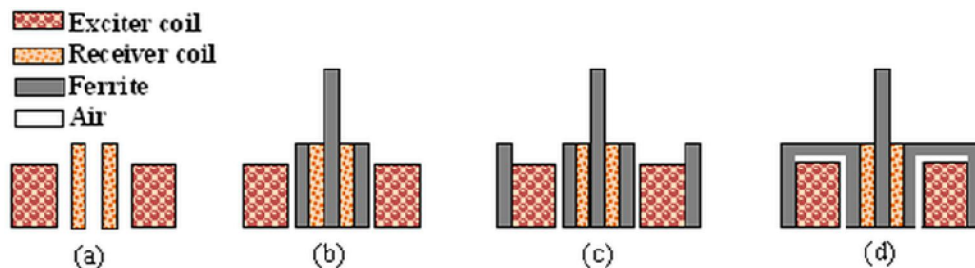


Figure 3.4: Cross-section of send-receive probe configurations studied through FE model (a) air core (b) ferrite core (c) ferrite core with outer shielding (d) cup-core.

In all the four configurations, receiver coils are kept inside the exciter coil. Selection of diameter of the exciter coil, excitation current and frequency are important and these are discussed in the following sections.

For detection of deep sub-surface flaws, lower excitation frequency and larger diameter probe is preferred. However, too large probe diameter would result in poor resolution and detection sensitivity. Hence, to optimise the probe diameter for detection of sub-surface flaws FE model based studies are carried out. For model based optimisation, minimum size of probe outer diameter (OD) is started from 15.0 mm, because of the geometrical constraints of the available minimum possible size of ferrite cores and exciter and receiver coils. Initially an excitation current of 500 mA is considered at an excitation frequency of 5 kHz (one depth of penetration ~

6.0 mm). For comparison purpose, the excitation current, probe dimensions and excitation frequency are kept same for all the four type of probe configurations.

For the study, an AISI type 304L stainless steel plate of 12.0 mm thickness having flat bottomed holes (FBH) of 3.0 mm diameter and located at various depths below the surface, D of 5.0, 6.0, 7.0 and 8.0 mm are considered in the model as shown in Figure 3.5. Flat bottomed holes are considered as simulate corrosion damage present in storage tanks in nuclear reprocessing plants. The eddy current responses of the flat bottom holes located at different depths by four different probe configurations are compared, apart from that of surface flaws of depth, d .

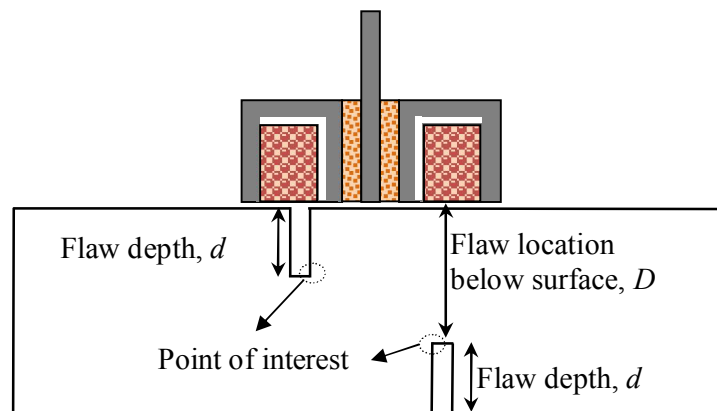


Figure 3.5: Specimen with surface and sub-surface flaw of same depth d in 12.0 mm thick austenitic stainless steel plate.

In order to compare the performance of probe configurations, the following model predicted parameters have been used:

i) Analysis of magnetic field contour: The minimum reluctance path of the magnitude of the flux density in SS plate has been predicted and analysed. A higher value of magnetic flux density at sub-surface flaw regions signifies deeper penetration of the field into the material.

ii) Eddy current density (J_e): Eddy current density at various depths (5.0 mm to 8.0 mm) below the surface has been predicted using the FE model and analysed. This parameter is an indicative

of the flux concentration around the flaw. A higher value of eddy current density around the flaw indicates better detection sensitivity.

iii) Change in phase angle ($\Delta\theta$): Change in phase angle ($\Delta\theta$) is the difference between the phase angle of induced voltage for flaw region and flaw-free region. The larger change in phase angle the better the detection sensitivity in the depth direction. For comparative analysis, model predicted change in phase angle of all four probe configurations is normalised with respect to the maximum change in phase angle ($\Delta\theta_{max}$) obtained for a sub-surface flaw by all four probe configurations as:

$$\text{Normalised } \Delta\theta = \frac{\Delta\theta}{\Delta\theta_{max}} \quad (3.7)$$

The above three parameters have been used for the selection of the optimum probe configuration.

After selecting the optimum probe configuration, the model based study is further extended towards optimisation of the probe dimensions and excitation frequency. This study mainly focuses on improving the detection sensitivity to sub-surface flaws located at more than 5.0 mm below the surface. For diameter selection, change in phase ($\Delta\theta$) at flaw location and induced voltage in receiver coil are predicted for FBH located at 8.0 mm below the surface and for selection of operating frequency, induced current density at flaw location is predicted for FBH located at range of 5.0 mm to 8.0 mm below the surface.

3.6 Results and discussion

3.6.1 Model predicted magnetic field and flux density

The surface log plots of magnetic flux density and normalised arrow plots of the magnetic field in the probe coil region are predicted for four types of probes and are shown in Figure 3.6 (a-d).

The magnitude and direction of the induced magnetic flux density are analysed. It is observed that among the four types of probe configurations, cup-core probe focuses more magnetic flux

into the material and this is due to the low reluctance path provided by the cup-core structure. Hence, it is expected that the cup-core probe would perform better for detection of deep sub-surface flaws than the other three types of probes considered in this study.

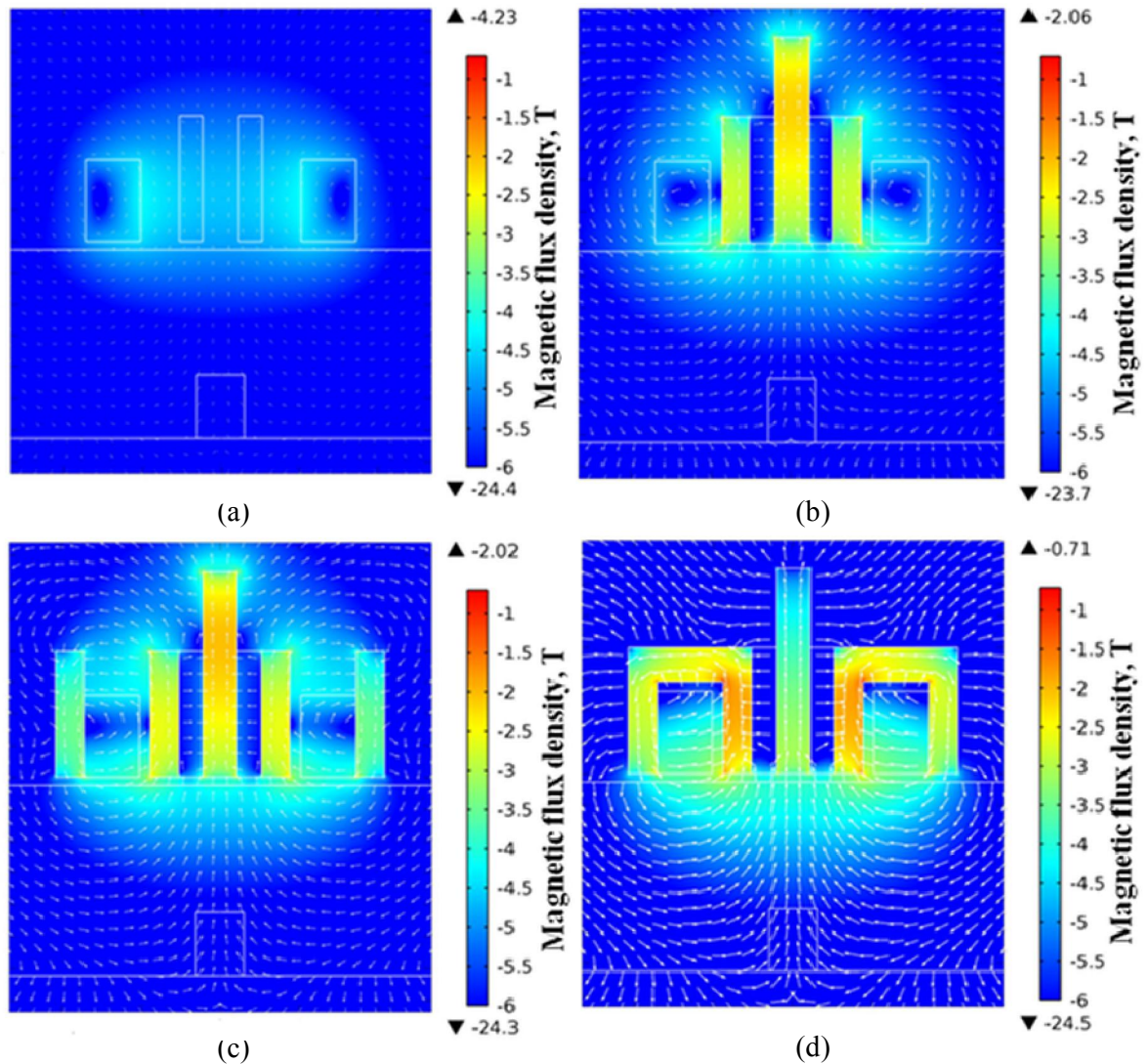


Figure 3.6: Surface log plot of magnetic flux density and arrow plot of the magnetic field for send-receive type (a) air core, (b) ferrite core, (c) ferrite core with outer shielding and (d) cup-core eddy current probes.

3.6.2 Model predicted eddy current density

Figure 3.7 (a-d) shows the predicted surface plot of eddy current density (J_e) for a sub-surface flaw located at 8.0 mm below the surface for all the four probe configurations. For easy

comparison, all the surface plots are drawn to the same contour code intensity. Higher value of eddy current density is induced by the cup-core probe configuration as compared to the other three types of probe configurations.

The eddy current density (at maximum perturbation points in the vicinity of the flaws) values computed for flaws located at different depths below the surface for all the four probe configurations are shown in Figure 3.8. The slope, i.e., change in eddy current density with change in flaws location (D) determined for the four types of probes is given in Table 3.2. The slope of eddy current density is found to be higher for the cup-core probe. This higher change of eddy current density indicates higher sensitivity, among all the probe configurations for sub-surface flaws. It must be noted that this slope is same whether one or more flaws present (same depth).

Table 3.2: Slope of eddy current density for four types of probes for detection of sub-surface flaws.

S. No.	Probe configuration	Slope of eddy current density for sub-surface flaws, kA/m ²
1.	Air core probe	-2.7
2.	Ferrite core probe	-5.0
3.	Ferrite core probe with outer shielding	-5.1
4.	Cup-core probe	-7.9

Similar analysis is also performed for the surface flaws of depths, d ranging from 5.0 mm to 8.0 mm. The model predicted eddy current density is shown in Figure 3.9 and the slope of eddy current density for the four types of probes is given in Table 3.3. As it is seen, for surface flaws also the cup-core probe shows higher sensitivity. These results clearly reveal that the cup-core probe ensures higher eddy current density as a result, higher sensitivity for detection of deep sub-surface as well as surface flaws.

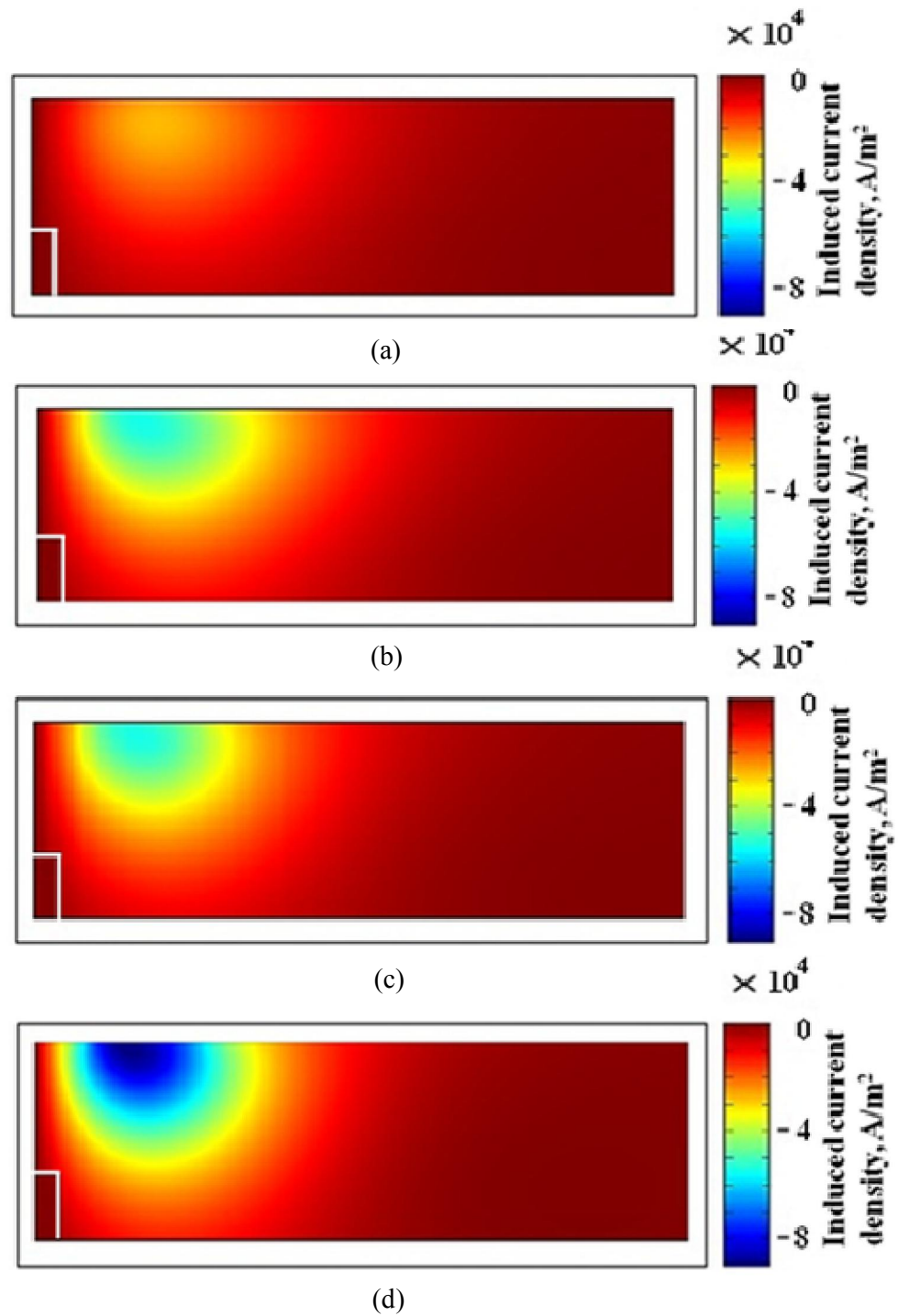


Figure 3.7: Surface plot of eddy current density for a sub-surface flaw located at 8.0 mm below the surface for (a) air core, (b) ferrite core, (c) ferrite core with outer shielding and (d) cup-core eddy current probes.

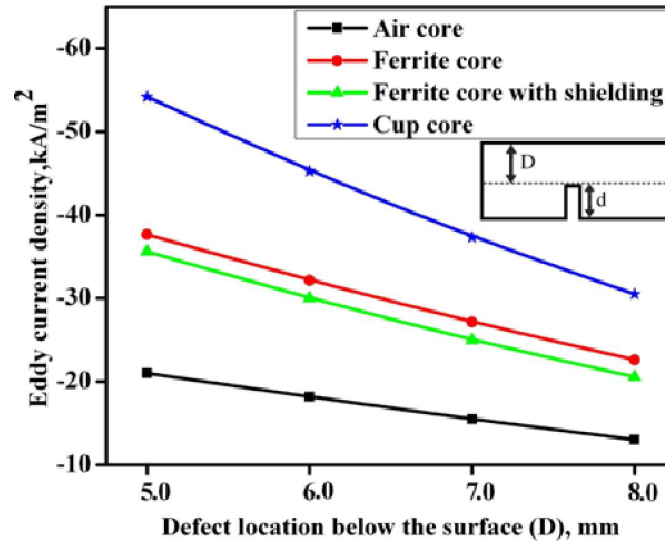


Figure 3.8: Model predicted eddy current density for sub-surface flaws located at different depths (D) below the surface for all the four type of probes.

Table 3.3: Slope of eddy current density for the four types of probes for detection of surface flaws.

S. No.	Probe configuration	Slope of eddy current density for surface flaws, kA/m^2
1.	Air core probe	-21.04
2.	Ferrite core probe	-39.70
3.	Ferrite core probe with outer shielding	-39.65
4.	Cup-core probe	-62.35

3.6.3 Model predicted change in phase angle ($\Delta\theta$)

Normalisation has been carried out using equation 3.7 to compare the performance of all four types of probes, as the signals for each probe are in different phase angle range. The normalised change in phase angle ($\Delta\theta$) for sub-surface flaws of all four type probes are given in Figure 3.10. As can be seen in Figure 3.10, a reduction in $\Delta\theta$ is observed with increasing flaw location below the surface, D . The appreciable change in $\Delta\theta$ is higher for the cup-core probe as compared to the

other three types of probes. Similarly, the response of normalised change in phase angle is calculated for surface flaws and is shown in Figure 3.11. A clear increase in $\Delta\theta$ is observed with increasing depth of the flaws, d .

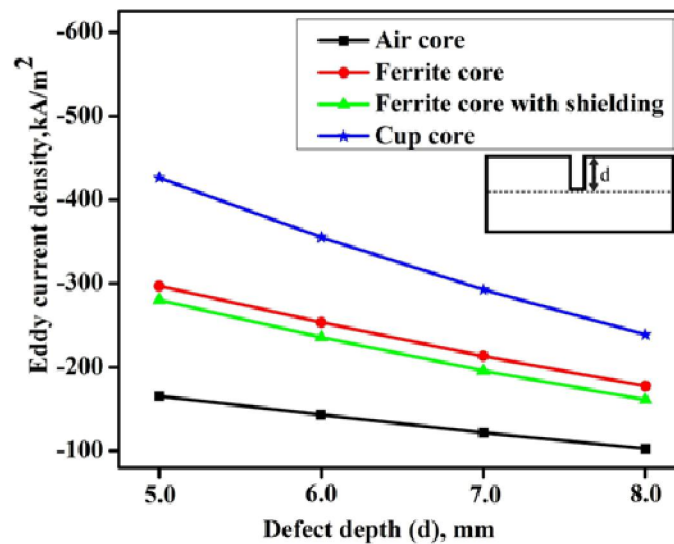


Figure 3.9: Model predicted eddy current density for surface flaws of varying depths ($d = 5.0, 6.0, 7.0$ and 8.0 mm) for all the four type of probes.

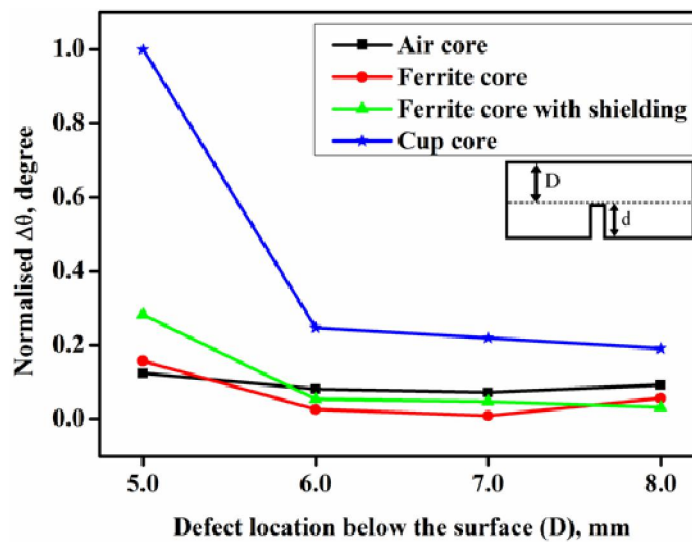


Figure 3.10: The normalised change in phase angle ($\Delta\theta$) for sub-surface flaws located at different depths (D) below the surface.

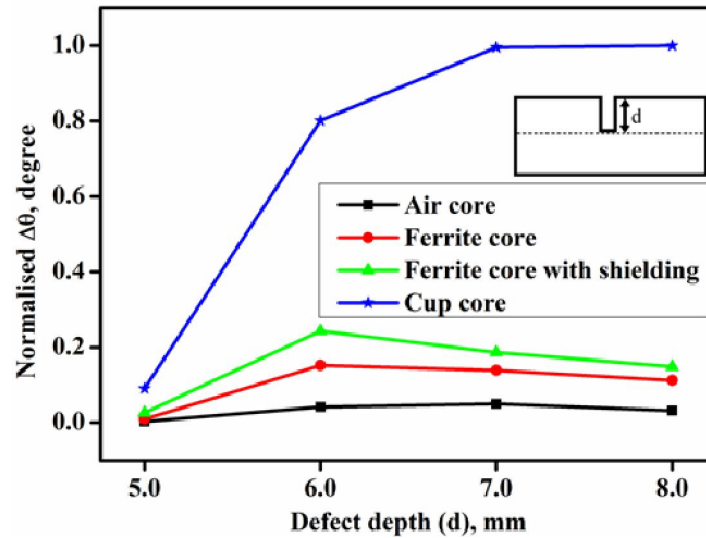


Figure 3.11: The normalised change in phase angle ($\Delta\theta$) for surface flaws of varying depths ($d = 5.0, 6.0, 7.0$ and 8.0 mm).

This capability of the cup-core probe will facilitate detection of surface and deep sub-surface flaws with better resolution in the depth direction. This detection sensitivity is attributed to the presence of top shielding in the cup-core configuration which ensures deeper penetration of primary magnetic field and as a result, increased sensitivity to deep sub-surface flaws. Based on these observations, cup-core type send-receive probe is considered as the optimum configuration for detection of deep sub-surface flaws as well as surface flaws in 12.0 mm thick austenitic stainless steel.

3.6.4 Optimisation of outer diameter of cup-core probe configuration

Optimisation of the outer diameter of the cup-core probe is important and for this model predicted change in phase angle ($\Delta\theta$) for a sub-surface flaw located at 8.0 mm below the surface is considered. Figure 3.12 shows the model predicted normalised $\Delta\theta$ for different diameters of the cup-core probe at 5 kHz. It is observed from Figure 3.12 that the $\Delta\theta$ increases with increase in probe diameter upto 22.0 mm and then decreases. This is essentially due to higher volume of interrogation and field divergence with increase in the probe diameter beyond 22.0 mm, resulting in the poor sensitivity for small flaws. Further, the induced voltage in receiver coil is predicted and

is shown in Figure 3.13. From Figure 3.13 it is evident that 22.0 mm diameter probe shows the highest value of induced voltage as compared to the other probe diameters.

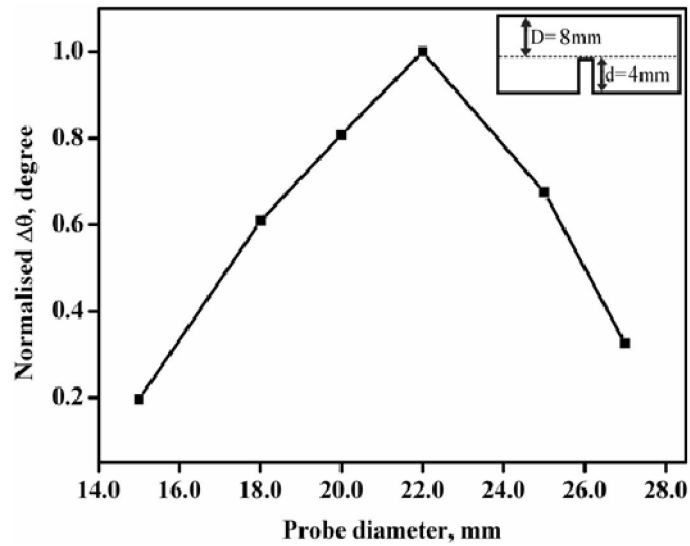


Figure 3.12: Model predicted normalised change in phase angle ($\Delta\theta$) of the cup-core probe at 5 kHz for various outer diameters for flaw located at 8 mm below the surface.

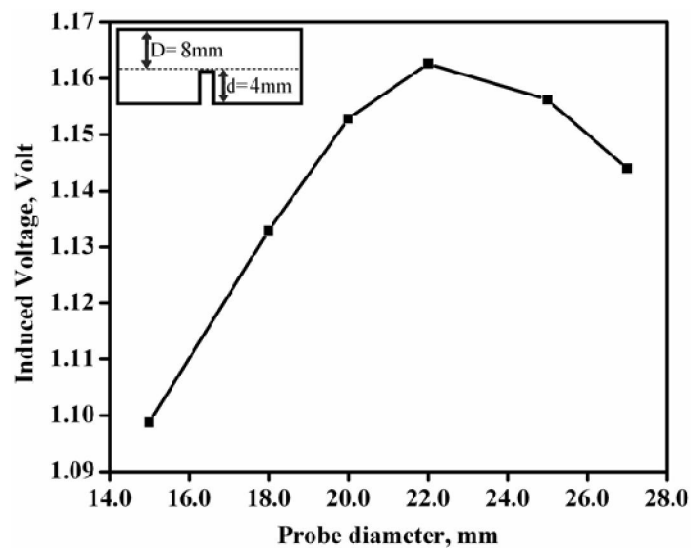


Figure 3.13: Model predicted induced voltage of the cup-core probe at 5 kHz for various outer diameters for flaw located at 8 mm below the surface.

In order to verify the performance of 22.0 mm optimised probe diameter, magnetic flux density, eddy current density and change in phase angle for 22.0 mm diameter have been predicted and shown in Figure 3.14. The results have compared with that of the 15.0 mm diameter probes and no changes in trends (Figure 3.8 to Figure 3.11) have been observed. However, the 22.0 mm diameter probes results have better detection sensitivity as compared to 15.0 mm diameter probes. Hence, the cup-core probe of 22.0 mm diameter is selected as the optimum for detection of deep sub-surface flaws in 12.0 mm thick SS plates and this is fabricated for experimental studies.

3.6.5 Selection of excitation frequency of cup-core probe

The performance of the optimised cup-core probe at different excitation frequencies is studied based on induced current density at flaw region. For this study, frequencies of 3 kHz, 5 kHz and 7 kHz are chosen. The induced current density at different depths ranging from 5.0 mm to 8.0 mm below surface in the specimen is predicted at 3 kHz, 5 kHz and 7 kHz and the result are shown in Figure 3.15. From the Figure 3.15, it is clearly seen that the induced current density of a sub-surface flaw located at 5.0 mm to 8.0 mm depths is higher for the excitation frequency of 5 kHz as compared to that of at 3 kHz and 7 kHz. It is also observed that the over all change in induced current density as function of flaw depth is higher at 7 kHz and at 3 kHz the change in induced current density is lower. However, the change in the induced current density and the amplitude of induced current density at 7.0 mm and 8.0 mm at 7 kHz is lower than that of at 5 kHz. The higher value of induced current density at 5 kHz is responsible for enhanced detection sensitivity. Hence, frequency 5 kHz is selected as the suitable frequency for detection of sub-surface flaws as it shows higher induced current density as well as higher change in induced current density as a function of the flaw depth below the surface.

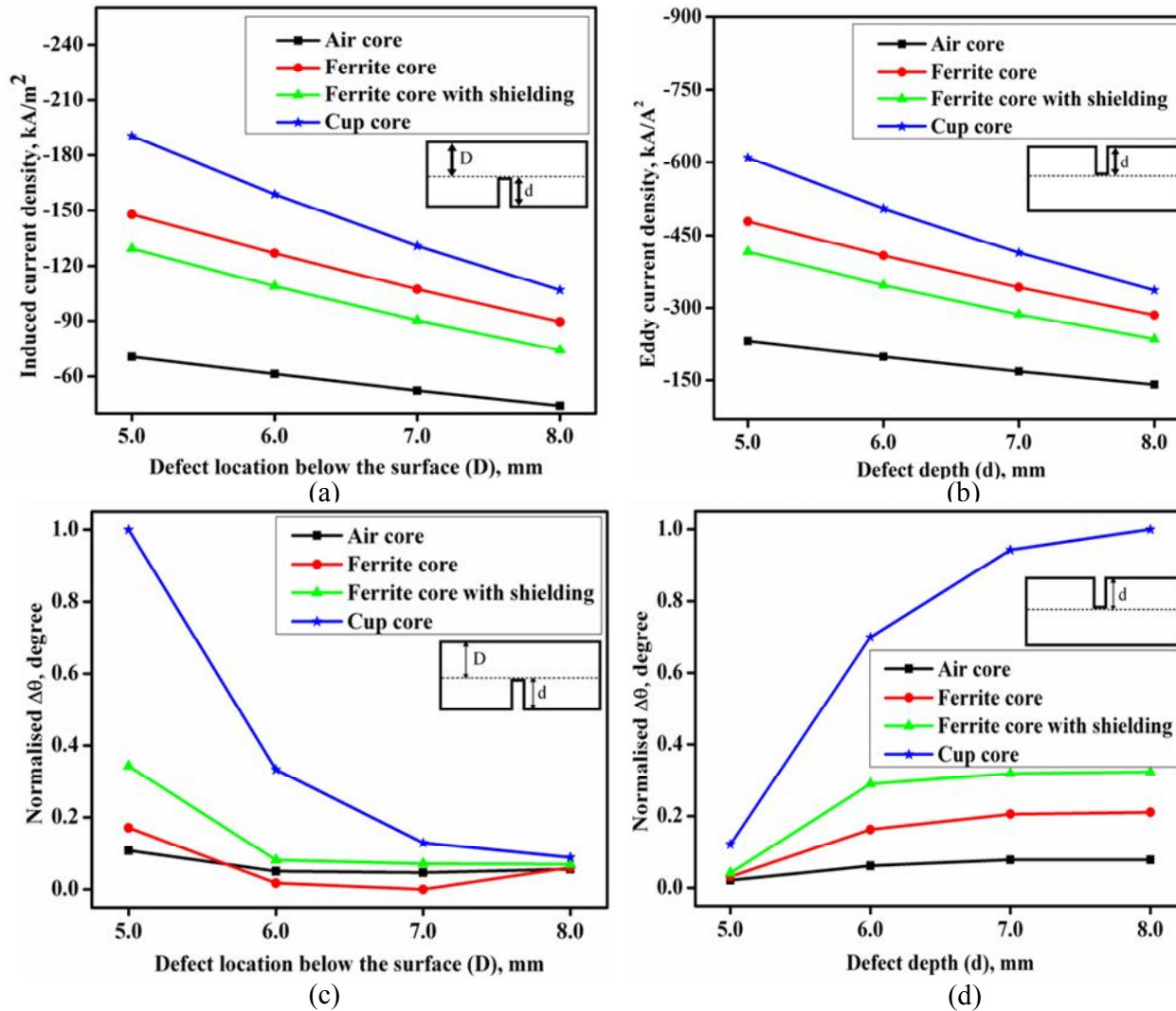


Figure 3.14: Model predicted eddy current density for (a) sub-surface flaw (b) surface flaw and the normalised change in phase angle ($\Delta\theta$) for (c) sub-surface flaw (d) surface flaw of 22.0 mm diameter probes.

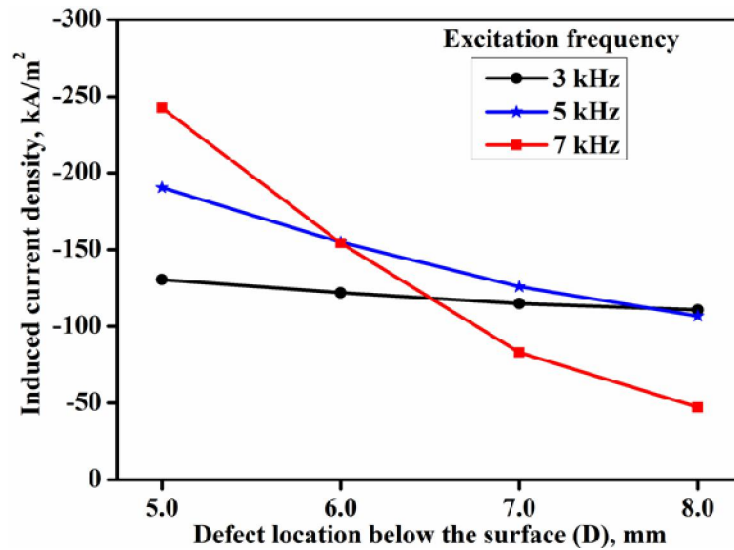


Figure 3.15: FE model predicted induced current density at different depth below the surface at frequency 3 kHz, 5 kHz and 7 kHz for the 22.0 mm diameter cup-core probe.

3.7 Experimental studies using optimised cup-core probe

Following the FE model based results a send-receive type cup-core EC probe has been designed and developed for detection of sub-surface flaws. The probe consists of an excitation coil, a ferrite core and a receiver coil. The receiver coil is centrally located within the exciter coil. Ferrite shielding is provided on entire side of the exciter coil. Figure 3.16 shows the cross section and photograph of the send-receive type cup-core probe. Table 3.4 provides the optimised dimensions and coil parameters of the EC probe.

Table 3.4 Dimensions of the cup-core EC probe

S. No.	Dimensions	Exciter coil	Receiver coil
1.	Inner Diameter (ID)	11.0 mm	2.0 mm
2.	Outer Diameter (OD)	22.0 mm	6.0 mm
3.	No. of turns	140	450
4.	Coil gauge (SWG)	30	40

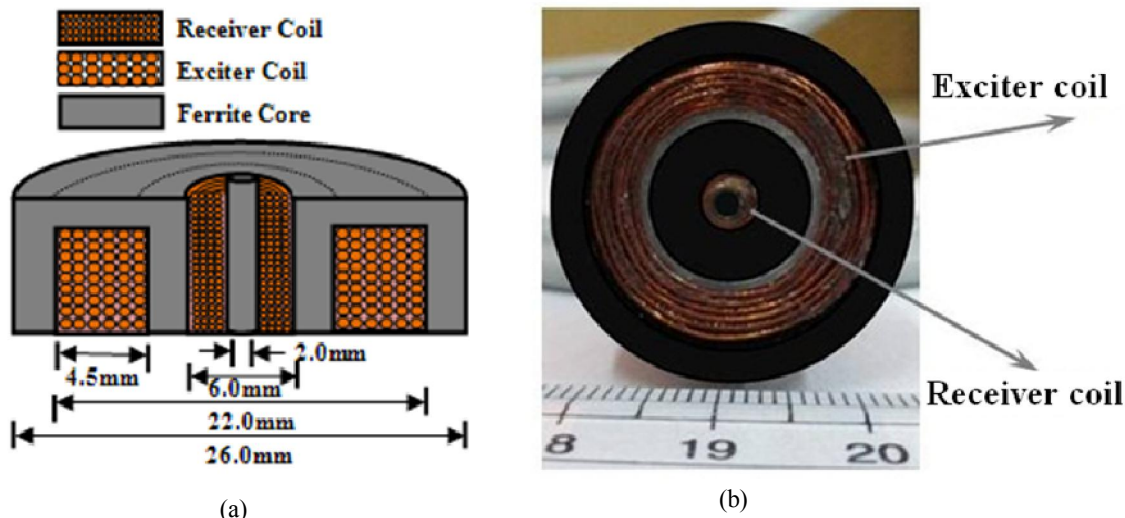


Figure 3.16: (a) Cross section of the cup-core probe and (b) photograph of the fabricated ECT probe.

3.8 Summary

For detection of sub-surface flaws in 12.0 mm thick stainless steel plates, studies have been carried out to optimize the probe configuration, dimensions and excitation frequency. FE modelling studies have been carried out for selection of optimum probe configuration among send-receive type air core, ferrite core, ferrite core with outer shielding and cup-core probes. The performance of these four types of probe has been analysed based on predicted parameters viz., magnetic flux density (indicative of low reluctance path), eddy current density (indicative of flux concentration at flaw location) and change in phase angle (indicative of detection sensitivity in depth direction). The following are the important results:

- Model predictions reveal that among all the four probe configurations, cup-core probe produces higher magnetic flux density and higher eddy current density at location more than 5.0 mm below the surface. This indicates its capability to focus higher flux at higher depths.

- The change in phase angle for flaws located at various depths is higher for the cup-core probe as compared to that of the air core, ferrite core and ferrite core probes with outer shielding. This promises better detection sensitivity in the depth direction by cup-core probe.
- For selection of optimum cup-core probe diameter for 12.0 mm thick stainless steel plate change in phase angle at flaw location and induced voltage in receiver coil have been predicted using the FE model for the first time. The cup-core probe of 22.0 mm outer diameter has shown larger change in phase angle as well as the magnitude of induced voltage. Hence, this probe is selected for detection of sub-surface flaws.
- The induced current density at different depths has been predicted for the cup-core probe at 3 kHz, 5 kHz and 7 kHz. Higher response for sub-surface flaws located at ranges of 5.0 mm to 8.0 mm below the surface has been observed at 5 kHz. Send-receive type cup-core probe has been fabricated for experimental studies on detection of sub-surface flaws.

Development of high sensitive eddy current instrument

4

4.1 Preamble

The scope of this chapter is to design and develop an eddy current instrument for detection of sub-surface flaws in 12.0 mm thick stainless steel plates. After a detailed discussion on the design considerations, the chapter presents the experimental results of the eddy current instrument for flat bottom holes and EDM notches. The performance of the developed instrument and cup-core probe is analysed and compared with that of a commercial ECT instrument.

4.2 Design of eddy current instrument

The five key modules that are to be considered while designing an EC instrument as illustrated in Figure 4.1 are excitation, modulation, signal preparation, signal demodulation and signal display.

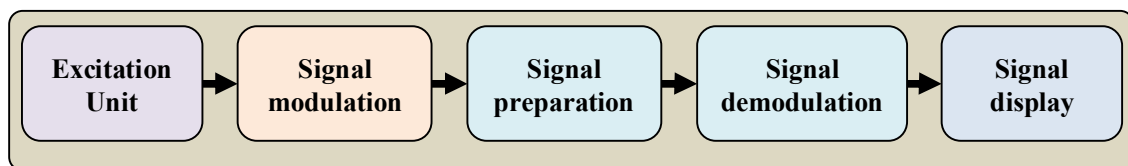


Figure 4.1: Main modules of an eddy current instrument.

The first module is the excitation unit which consists of signal generator and power amplifier. The signal generator provides a single or multiple frequency sine wave signal or pulse signal for excitation of the EC probe. A power amplifier is used to increase the signal strength. Signal modulation occurs in the presence of the electromagnetic fields of EC probe and test material.

Signal preparation and demodulation modules comprise of detector and analyzers. After demodulation, the output signal is displayed.

Commercially available ECT instruments have limitation for detection of flaws beyond 5.0 mm in stainless steel plates [56]. This is essentially due to lower excitation current levels (<300 mA) and lack of precise measurement of amplitude and phase of the eddy current sinusoids from sources such as sub-surface flaws. Hence, it is proposed to develop a portable high-power, high sensitive EC instrument with lock-in based I/Q detection method for detection of sub-surface flaws using cup-core type EC probe.

Detection of sub-surface flaws demands high sensitive measurement of low magnetic fields associated with them. One way to achieve this is by strengthening the primary magnetic field of the EC probe i.e. higher excitation current. Hence, the EC instrument has been designed to excite probe coils up to a current of 1A.

The measurement of low magnitude field associated from sub-surface flaws is generally influenced by material noise. For characterization of sub-surface flaws in the presence of noise, precise measurement of phase angle and amplitude is essential. Hence, a high precise lock-in based I/Q detection method is employed. Accordingly, the proposed EC instrument for detection of sub-surface flaws in stainless steel plates (thickness 12.0 mm) consists of the following:

1. User controlled signal generation unit with a power amplifier for high current excitation
2. High dynamic range 24-bit analog-digital converter card for data acquisition
3. Digital lock-in amplifier based in-phase, quadrature, amplitude and phase measurement
4. Motion control card for automated scanning of the cup-core type ECT probe

The schematic block diagram of the proposed EC instrument is shown in Figure 4.2.

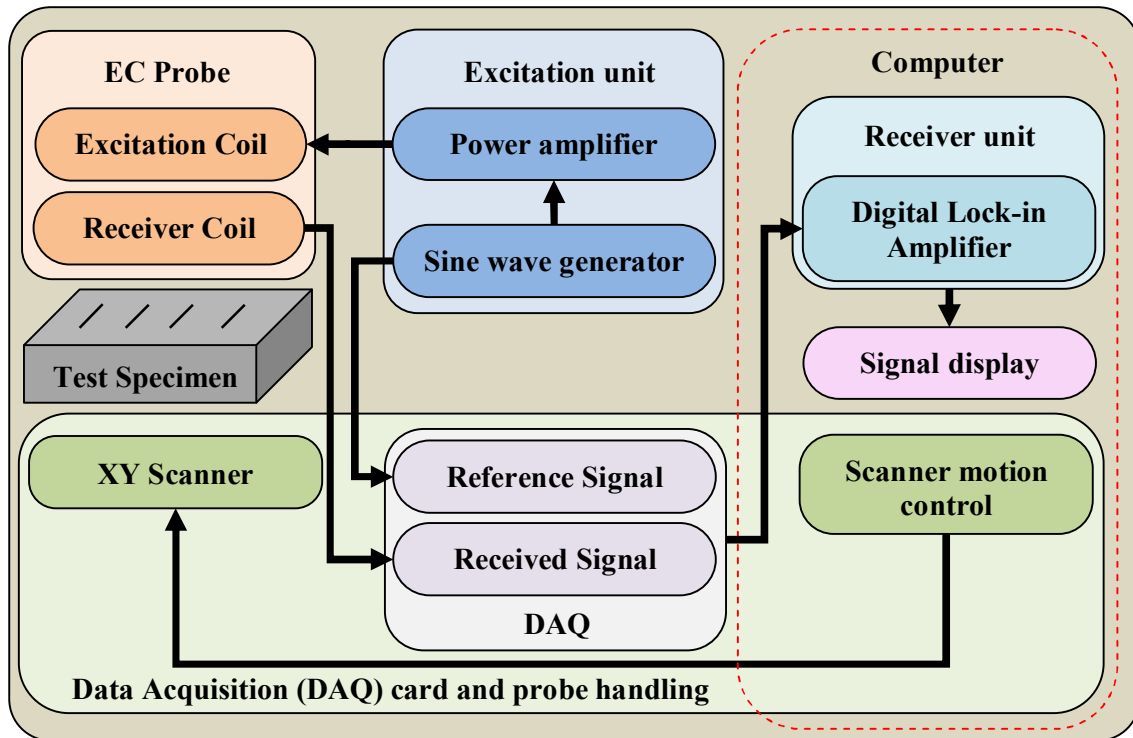


Figure 4.2: Schematic block diagram of the ECT Instrument.

4.2.1 Excitation unit

The excitation unit consists of a sine wave generator and a high current user-selectable power amplifier. The circuit diagram of the developed excitation unit is shown in Figure 4.3. The sine wave generator is made by XR-2206 monolithic function generator integrated circuit, which is capable to produce high quality sine waveforms with high-stability and accuracy. A high purity sine wave could be generated using the signal source in 500 Hz to 80 kHz range with peak to peak voltage up to 6 V and current 50 mA. The frequency (f) of signal is calculated by the capacitor C and resistor R connected in Figure 4.4. Desired excitation frequency is adjusted by the change the value of R and C and the excitation frequency given by:

$$f = \frac{1}{RC} \text{ Hz} \quad (4.1)$$

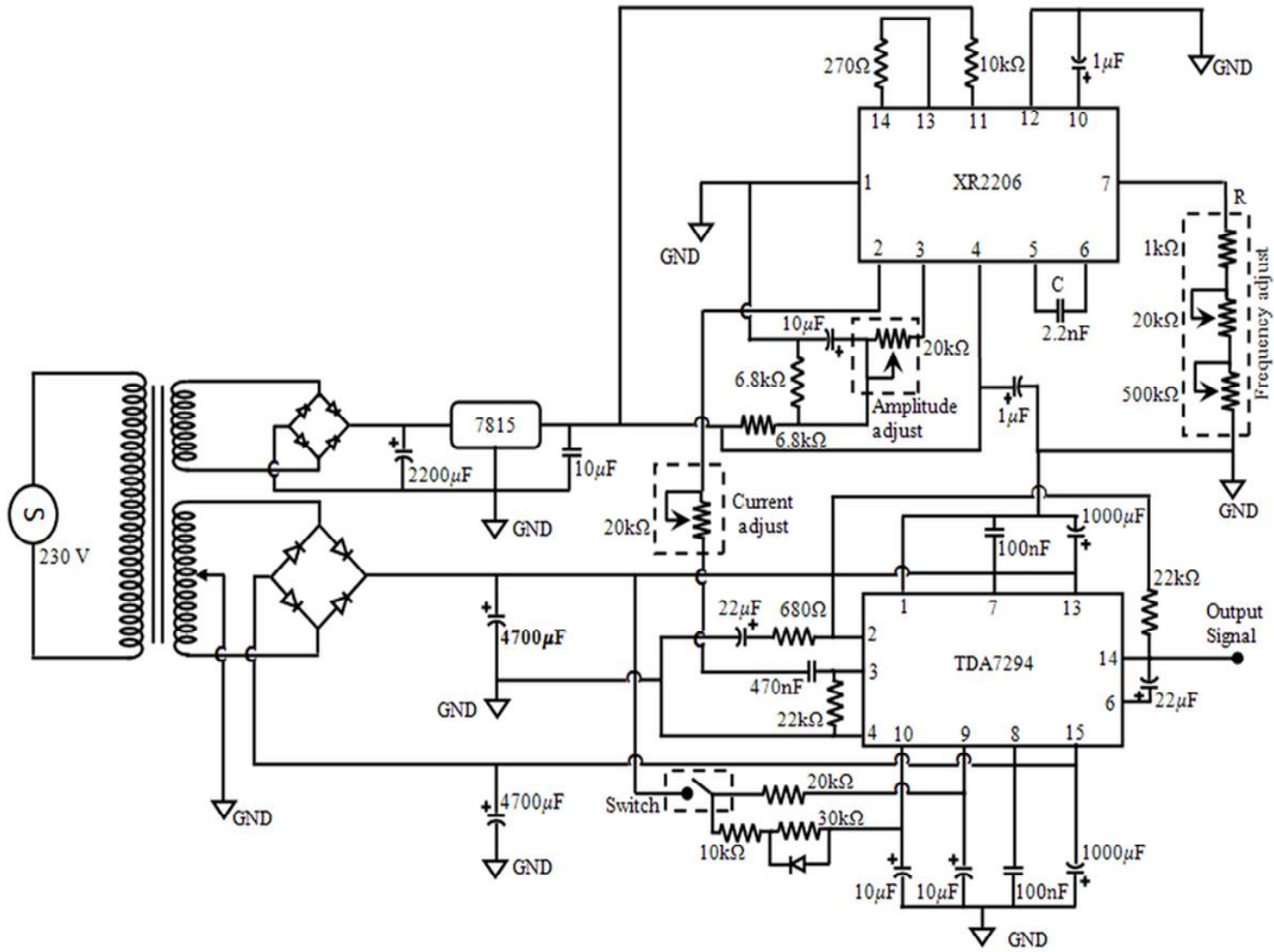


Figure 4.3: Circuit diagram of developed excitation unit.

The power amplifier used in the excitation unit is made by the TDA7294 monolithic integrated circuit. In the power amplifier, mixed bipolar-MOS and high-power DMOS buffer is used for handling the extremely high current and voltage levels while maintaining acceptably low harmonic distortion and good behavior over frequency response. The output voltage of the power amplifier is made variable by the voltage divided rule to change the excitation current. By this way, a sine wave signal of output current upto 1 A is obtained with low harmonic distortion and excellent frequency response

The signal generator and amplifier circuits are tested for stability, distortion, higher current and harmonic content free sine waves. In order to assess the purity of the sine wave, the total harmonic distortion (THD) has been measured. THD is defined as the ratio of the sum of the powers of all harmonic components to the power of the fundamental frequency as shown in the equation given below:

$$THD\% = \frac{P_2 + P_3 + P_4 + \dots + P_\infty}{P_1} \times 100 \quad (4.2)$$

The powers of the harmonic components of the waveform have been evaluated by computing the power spectral density using the fast Fourier transform. The sine wave after the power amplifier has been found to be pure with a THD of less than 1%, when the source has not been connected to any load. The THD has been found to be less than 2.5% when it is connected to a 50 Ω inductive load at an excitation frequency of 5 kHz.

4.2.2 Reception unit

EC probe signals are influenced by noise from various sources i.e material surface, instrument, environment etc. The induced eddy currents are attenuated with depth. Because of this, the amplitude of the received EC signal from sub-surface flaws is feeble. The detected signals are also influenced by the variations in material properties such as the permeability, surface

roughness and lift-off that produce high frequency noise. Hence, for extraction of the information from sub-surface flaws, a high sensitive precise phase measurement unit based on lock-in amplifier has been developed.

A digital lock-in amplifier has been implemented for measurement of in-phase, quadrature, magnitude and phase angle. The digital lock-in amplifier measures the phase and magnitude of the receiver coil sinusoid (input sine wave) with respect to reference sinusoid of the exciter coil. It locks the frequency of the sinusoids that matches the reference frequency, thereby acting as a narrow band pass filter with a bandwidth of the order of mHz.

A schematic working of the lock-in amplifier is shown in Figure 4.4. In this, the magnitude 'A' and the phase angle ' θ ' of an input sine wave of angular frequency ω_s , are measured with respect to a reference sine wave of angular frequency ω_R . The phase locked loop (PLL) block measures the frequency of the reference sine wave and generates orthogonal sine and cosine components. These two waves are individually multiplied with the input sine wave. The resulting components have additive and subtractive frequency terms in sine and cosine as shown in Figure 4.4. When there is a match between the reference frequency and the input sine wave frequency, the additive terms give the higher frequency components (ω) and the subtractive terms provide the DC components. The higher frequency components are filtered using a low-pass filter to obtain the DC components X and Y which are respectively the in-phase (X) and quadrature (Y) components of the receiver coil induced voltage. The magnitude (A) and the phase angle (θ) are calculated from the measured in-phase and quadrature components. This digital lock-in amplifier has been implemented in LabVIEW environment. In the digital lock-in amplifier, the resulting output is free from high as well as low frequency noise, as only the components corresponding to the reference sine wave are selectively chosen and handled. The digital lock-in amplifier provides the analog output of either X and Y or A and θ from the received EC signal.

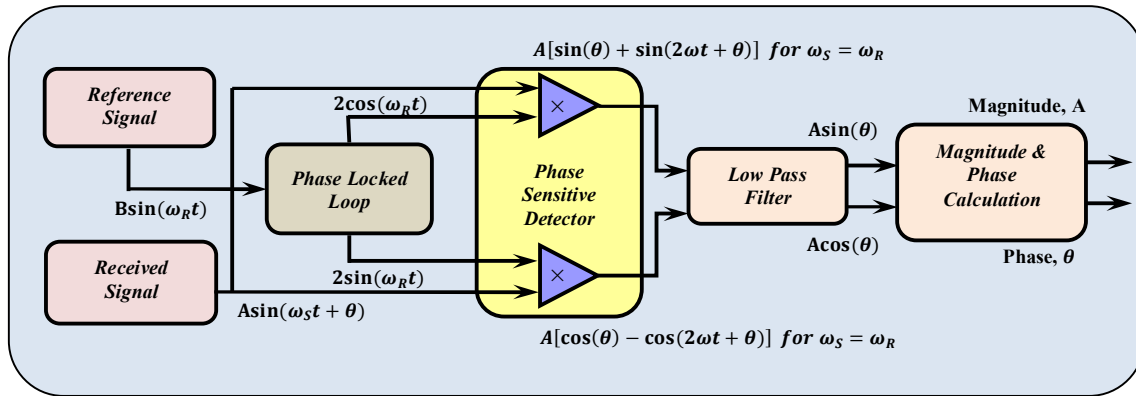


Figure 4.4: Schematic diagram of implementation of lock-in amplifier in LABVIEW development environment.

4.2.3 Data acquisition and probe scanning

In the EC instrument, data acquisition (DAQ) and handing of probe are controlled using the LabVIEW software. EC signals are acquired using a high dynamic range 24-bit analogue-digital converter (ADC) card that operates at a sampling frequency of 500 kHz. Receiver coil signal and reference excitation signal are acquired for processing by the digital lock-in amplifier. The EC instrument is interfaced to an XY scanner for automated scanning of the EC probe over the SS plate surface. The scanner is controlled using a NI PCI-7330 motion control card and LabVIEW software.

A user friendly graphical user interface (GUI) program has been developed using LabVIEW for the lock-in amplifier, DAQ and probe scanning. The GUI consists of processing and display modules. The processing module contains the digital lock-in amplifier for precise measurement of the EC response. The display module contains the real-time display of complex plane as well as time domain phase and magnitude signals. Before probe scanning, step size and distance are defined to control the movement of the EC probe. Figure 4.5 and Figure 4.6 show the block diagram and the front panel of the LabVIEW based GUI program respectively.

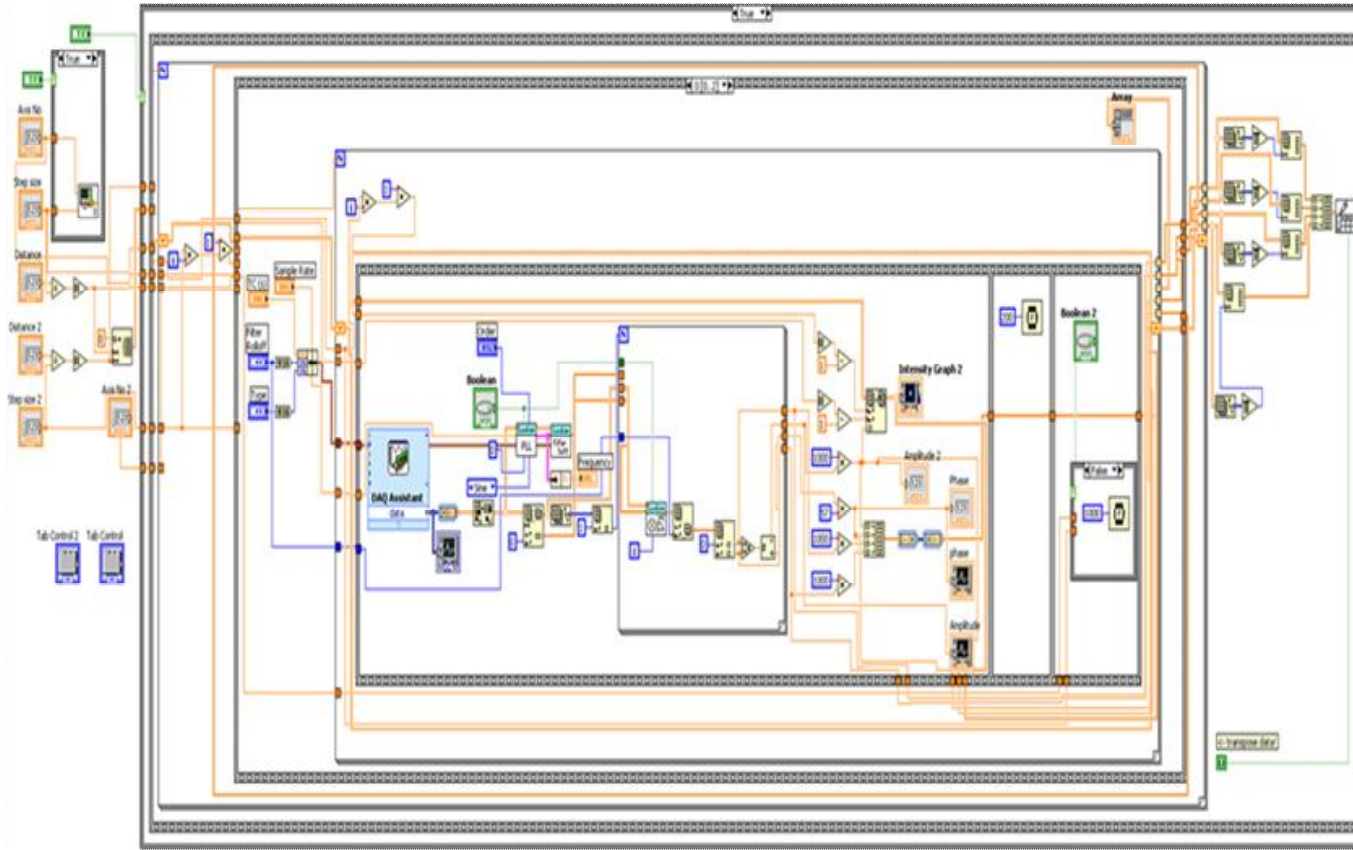


Figure 4.5: Block diagram of the lock-in amplifier based phase measurement.

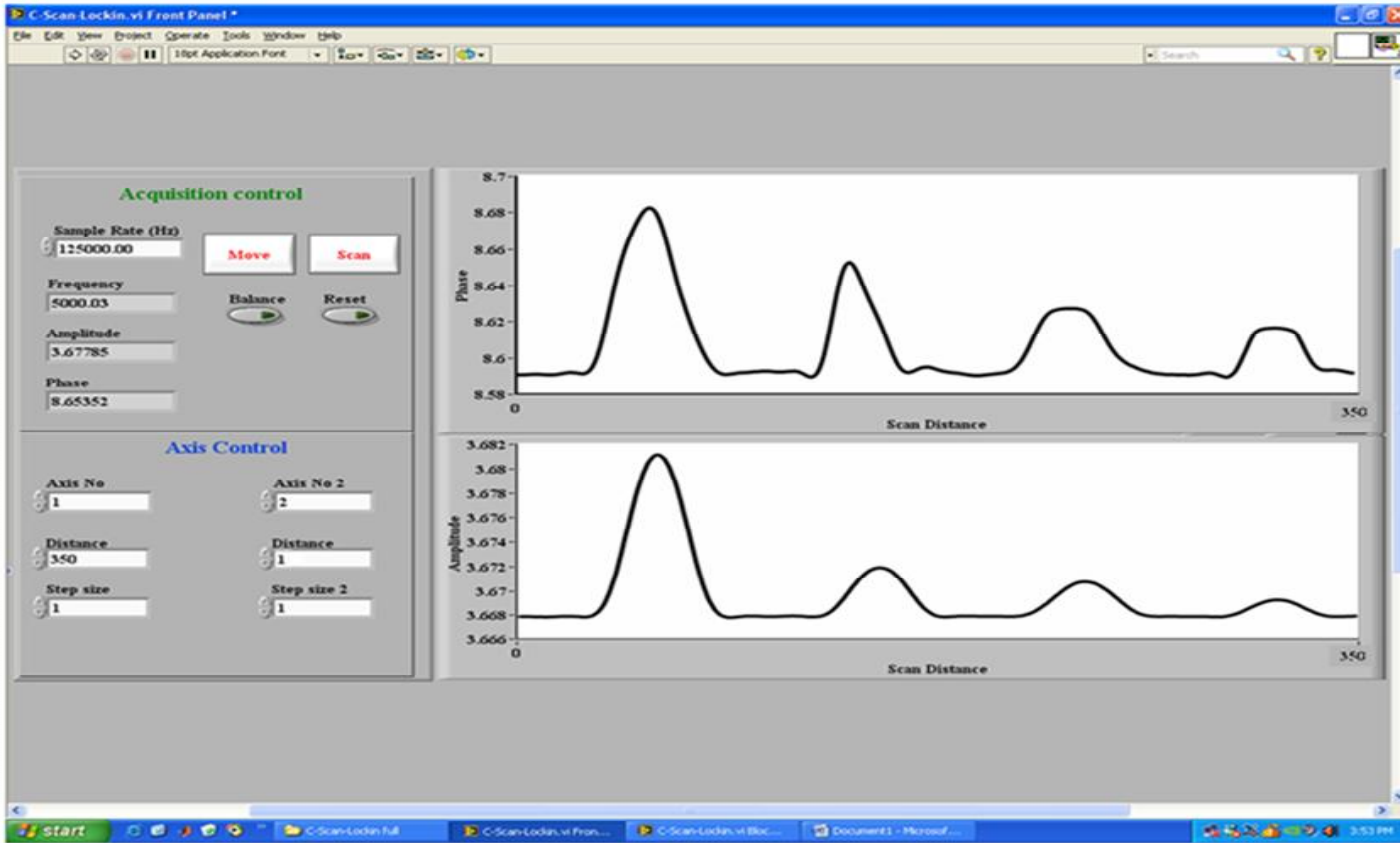


Figure 4.6: Front panel GUI of the lock-in amplifier based phase measurement.

4.3 Test specimens for experiments

The test specimens of size $350.0 \times 70.0 \times 12.0 \text{ mm}^3$ plate made of AISI type 304L stainless steel are used for verifying the performance of EC probe and instrument developed. For evaluation of the instrument, flat bottom holes and notches are introduced in three 12.0 mm thick SS plates by electro discharge machining. A schematic of three plates is shown in Figure 4.7. Four numbers of flat bottom holes of diameter 3.0 mm at different depths in the range of 5.0 mm to 8.0 mm are used to simulate sub-surface localized corrosion and they are fabricated in a plate as shown in Figure 4.7 (a). A set of four notches of length 30.0 mm and width 2.5 mm at different depths in the range of 5.0 mm to 8.0 mm and another set of three notches of length 20.0 mm and width 1.0 mm at different depths i.e. 4.0 mm, 6.0 mm and 8.0 mm are fabricated in two plates and their details are shown in Figure 4.7 (b-c). For studies related to surface flaws, experiments are performed on opposite side of the plate i.e. by flipping the plate. The dimensions of the flat bottom holes and machined notches introduced in the 12.0 mm thick SS plates are given in Table 4.1 and Table 4.2.

Table 4.1: Dimensions of machined notches in SS 304L plate.

S. No	Flaw	Length, mm	Width, mm	Flaw depth (d), mm	Depth below the surface (D), mm
1.	Notch 1 (D1)	30.0	2.5	7.0	5.0
2.	Notch 2 (D2))	30.0	2.5	6.0	6.0
3.	Notch 3 (D3)	30.0	2.5	5.0	7.0
4.	Notch 4 (D4)	30.0	2.5	4.0	8.0
5.	Notch 5 (D5)	20.0	1.0	8.0	4.0
6.	Notch 6 (D6))	20.0	1.0	6.0	6.0
7.	Notch 7 (D7)	20.0	1.0	4.0	8.0
8.	Notch 4 (S1)	20.0	1.0	8.0	0.0
9.	Notch 5 (S2)	20.0	1.0	6.0	0.0
10.	Notch 6 (S3)	20.0	1.0	4.0	0.0

Table 4.2: Dimensions of flat bottom holes in SS 304L plate.

S. No.	Flaw	Diameter, mm	Flaw depth (d), mm	Depth below the surface (D), mm
1.	FBH1(F1)	3.0	7.0	5.0
2.	FBH2(F2)	3.0	6.0	6.0
3.	FBH3(F3)	3.0	5.0	7.0
4.	FBH4(F4)	3.0	4.0	8.0

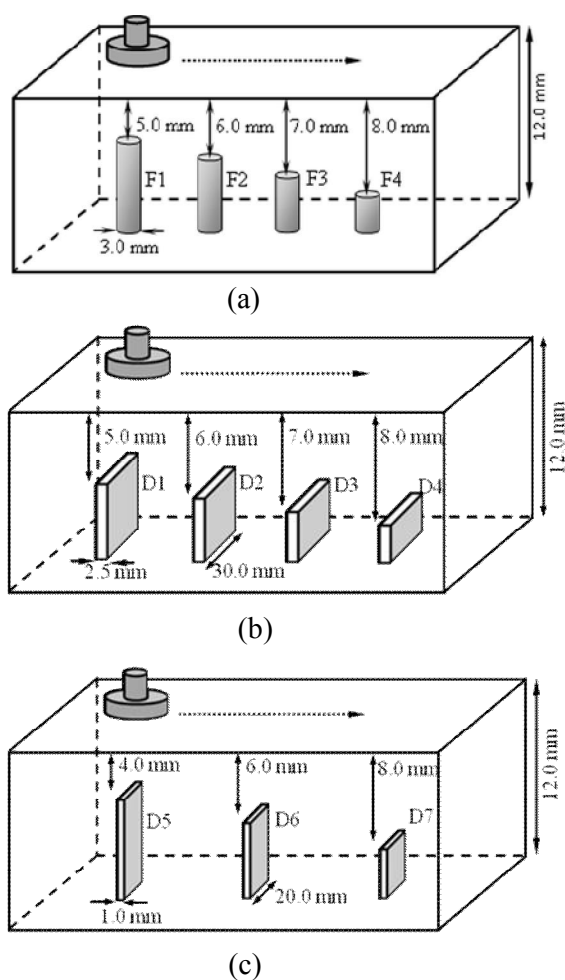


Figure 4.7: Schematic of stainless steel plates with machined (a) flat bottom holes (b) notches (width 2.5 mm) and (c) notches (width 1.0 mm).

4.4 Performance assessment of eddy current instrument

Photo graph of a developed instrument is shown in Figure 4.8. Systematic studies have been carried out to assess the performance of the developed EC instrument as well as the cup-core probe. For assessment of the instrument, the signal resolution and the detection sensitivity for sub-surface flaws have been studied.

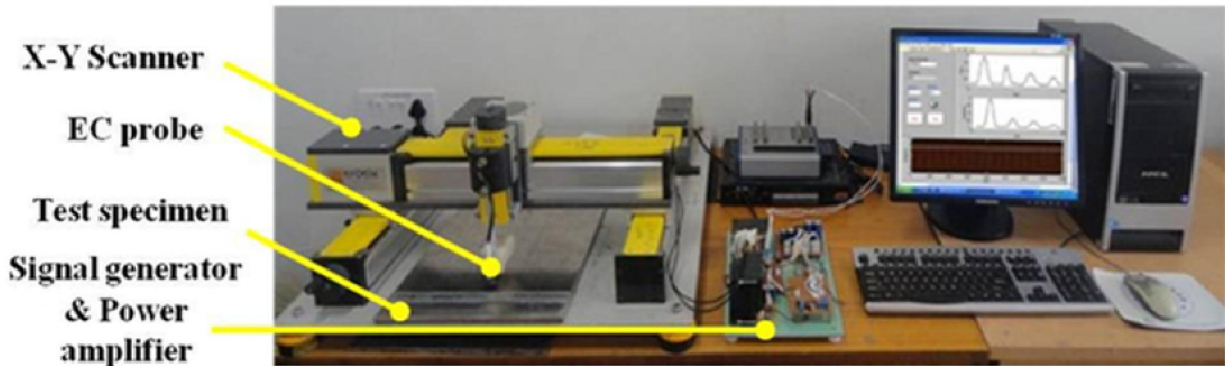


Figure 4.8: Photograph of the developed ECT instrument.

4.4.1 Influence of excitation current

First the influence of the excitation current on the performance of the developed instrument and the cup-core probe has been studied. For this the excitation current has been increased and the temperature of the excitation coil has been measured. Figure 4.9 shows the measured coil temperature as a function of the excitation current. From the Figure 4.9 it is clearly seen that as the excitation current increases temperature of the coil increases exponentially. For the excitation current upto 750 mA, the increase in temperature of the excitation coil is moderate and afterwards the rise is found to be high. Because of the higher change in temperature, excitation coil is found to starts heating. Hence, the use of very high excitation current i.e. > 750 mA is not suitable, as it may damage the enamel insulation on the copper winding.

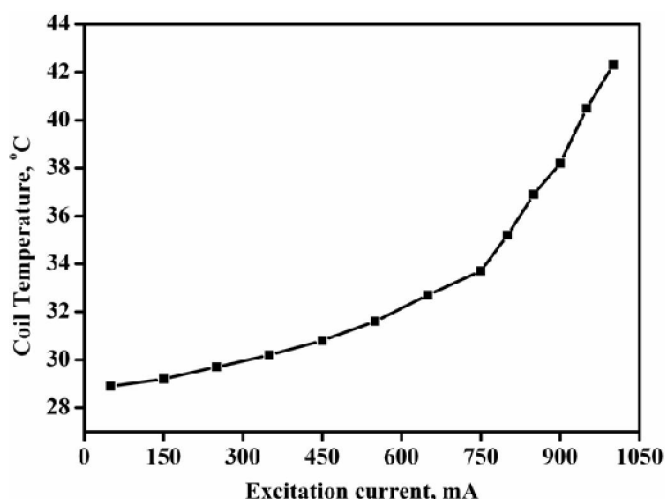


Figure 4.9: Measured coil temperature as function of the excitation current in ECT probe.

The influence of excitation current on the capability for detection of sub-surface notches has been studied. For this study, the excitation current has been varied in the range of 250 – 750 mA. For each current, the EC magnitude and phase responses for notches D3 and D4 have been observed. Figure 4.10 (a-b) shows the magnitude and the change in phase angle response for notches D3 and D4 respectively, as a function of the excitation current. As can be seen from Figure 4.10 (a), the magnitude increases monotonically with increasing in the excitation current. This is due to fact that the increase in excitation current increases the eddy current density in the material which, results in, higher magnetic flux density interacting with the receiver coil.

As can be noted from Figure 4.10 (b), an increase in the change in phase angle (difference between phase angle in notch free and notch regions) is observed for both the notches only up to an excitation current of 550 mA. Further increase in current did not show any increase in the phase angle. The measurements have been repeated 5 times and the deviation in the measurements has been shown in Figure 4.10 (a-b). This study clearly indicates that higher excitation current increases the sensitivity of phase measurement of eddy current sinusoids, thereby, enabling detection of sub-surface flaws. Hence, by excitation current selection capability of the developed instrument, detection sensitivity for deep sub-surface flaws can be enhanced. For further studies on sub-surface flaws in 12.0 mm

thick SS plate, excitation current 550 mA is chosen as there is no improvement in phase response at higher excitation currents and the temperature rise is within 30°C

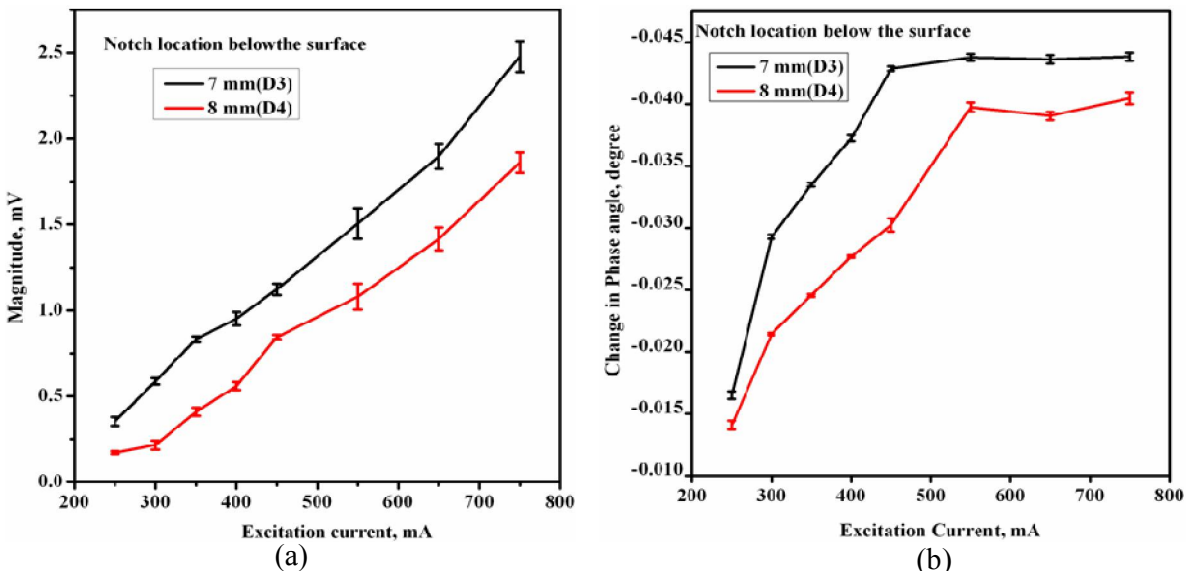


Figure 4.10: (a) Magnitude (b) change in phase angle response of the cup-core probe at different excitation currents for sub-surface notches D3 and D4.

4.4.2 Phase angle resolution

Phase angle resolution of the developed instrument has been determined using a line scan over the notch D4 at a step size of 2.0 mm. Table 4.3 shows the change in phase angle at different scan points. From the Table 4.3 it is found that the minimum difference of change in phase angle between two adjacent scan points is 0.001 degree. This clearly shows the higher phase sensitivity of the developed instrument for minimum shift in location.

The phase angle resolution of the developed instrument has also been verified by the measurement function described by Clarkson [59]. Details of the measurement function are given in Appendix A. For this purpose the input parameter used by the developed instrument are 16-bit of quantization level, 125 kHz sampling frequency and 0.25 s time constant. It is found that the developed instrument has achieved a phase angle resolution same as the calculated phase resolution i.e. 0.001 degree.

Table 4.3: Change in phase angle for five line scan points (step size 2.0 mm).

S. No.	Line scan points	Change in phase angle, degree
1.	0 mm	-0.0311
2.	2 mm	-0.0324
3.	4 mm	-0.0336
4.	6 mm	-0.0345
5.	8 mm	-0.0353

4.4.3 Drift

The drift of the developed instrument has been analysed for long time inspections. For this the instrument has been kept 'ON' for 6 hours and the phase angle response for a notch D4 as well as the temperature of the excitation coil have been measured for every half hour under controlled conditions. From the Figure 4.11 it is found that for 6 hour duration the increase in temperature of the coil is approximately 1° and change in phase angle is observed to be 0.004 degree (decreases). This shows the stability of the developed instrument.

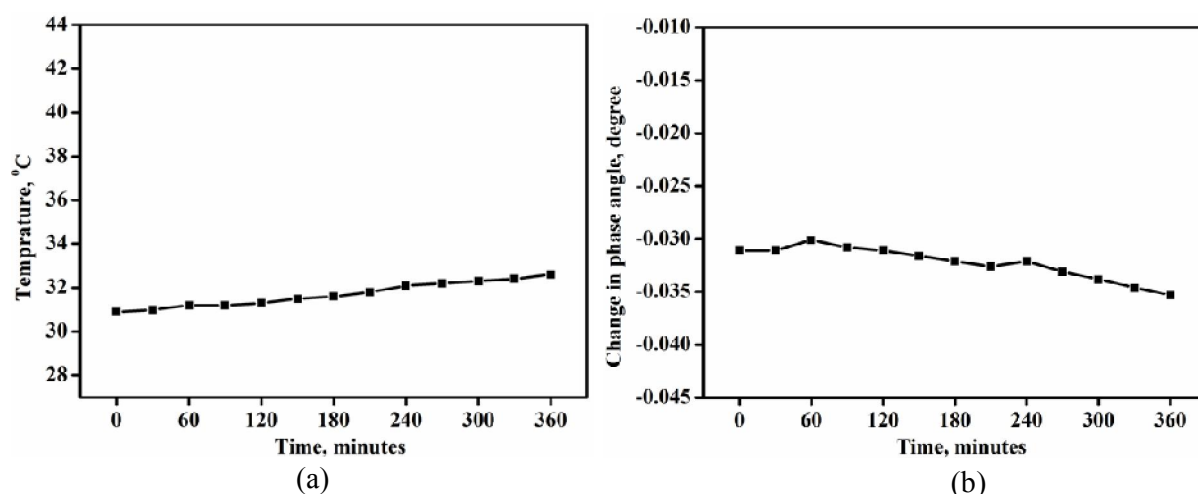


Figure 4.11: (a) Temperature of the excitation coil and (b) change in phase angle as function of time.

4.4.4 Response of eddy current instrument

4.4.4.1 Response for sub-surface flaws

The response of the developed instrument for the sub-surface flaws line scan of EDM notches (details given as D1, D2, D3 and D4 in Table 4.1 and Figure 4.7 (b)) located at different depths below the surface (5.0 mm to 8.0 mm) are obtained. The response for the EDM notches is shown in Figure 4.12 as time-domain in-phase, quadrature components and Figure 4.13 as impedance plane signals. It is evident from Figure 4.12 that the notch located 8.0 mm below surface could be reliably detected by the EC instrument and cup-core probe. From impedance plane signal shown in Figure 4.13, a clear change in phase angle and magnitude of the EDM notches are observed and this shows the better detection sensitivity to sub surface flaws.

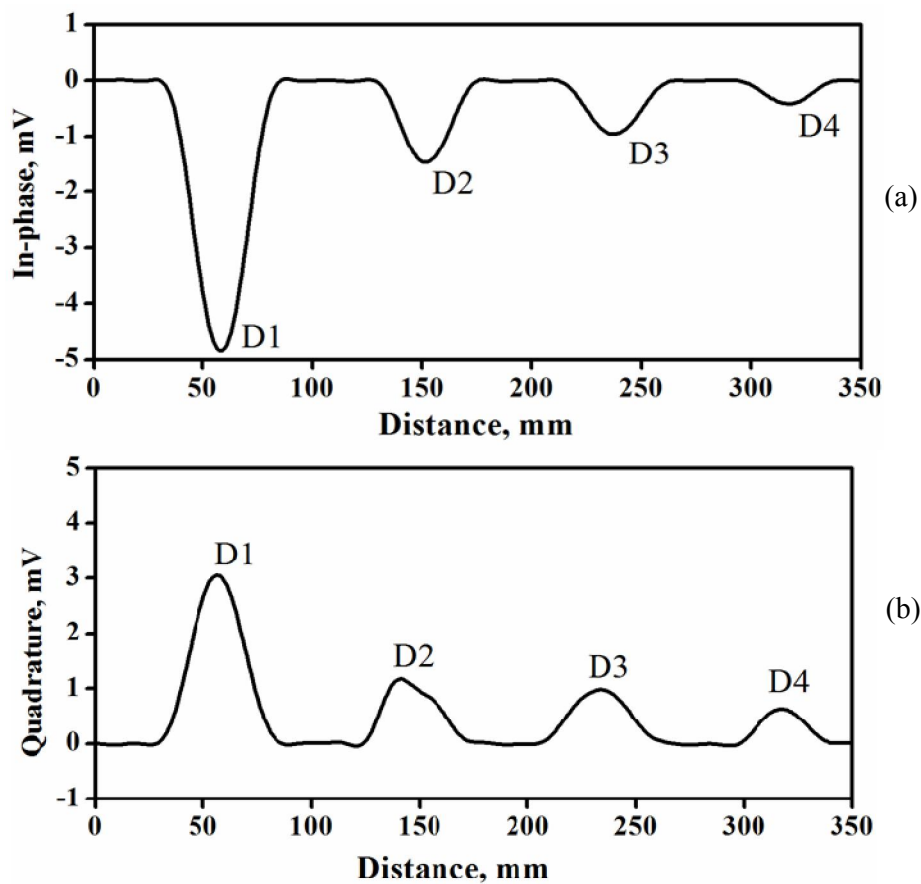


Figure 4.12: Time domain (a) in-phase and (b) quadrature components signals obtained for sub-surface notches.

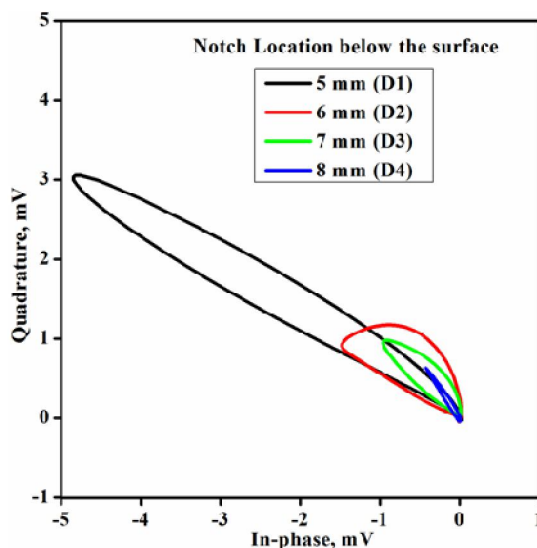


Figure 4.13: Impedance plane signals obtained for sub-surface notches.

The peak magnitude and phase angle as a function of notch depth (location below the surface) is calculated and shown in Figure 4.14. The peak magnitude shows a saturation behaviour after 6.0 mm depth. This is due to the exponential decay of the eddy currents. On the contrary, change in phase angle shows a near linear trend with increase in flaw depth. This linear sensitivity of the developed instrument and cup-core probe facilitates improvement in detection and sizing of sub-surface flaws with better resolution in depth direction. The linear fit and experimental data of the notch is shown in Figure 4.15 as a function of change in phase angle. From Figure 4.15 the relation between change in phase angle ($\Delta\theta$, degree) and notch location below the surface (D , mm) is derived for the notch of length 30.0 mm and width 2.5 mm in 12.0 mm thick SS plate and equation is:

$$D = 8.73 + 29.59 \times \Delta\theta \quad (4.3)$$

From the proposed equation 4.3, the notch location below the surface can be calculated for a given change in phase angle with an accuracy of 96% (deviation 0.19 mm).

The measurements on the EDM notches have been repeated 5 times to check the repeatability of the instrument. As shown in Figure 4.14, the developed instrument has shown capability to generate the same signal with a marginal change of 0.003 degree.

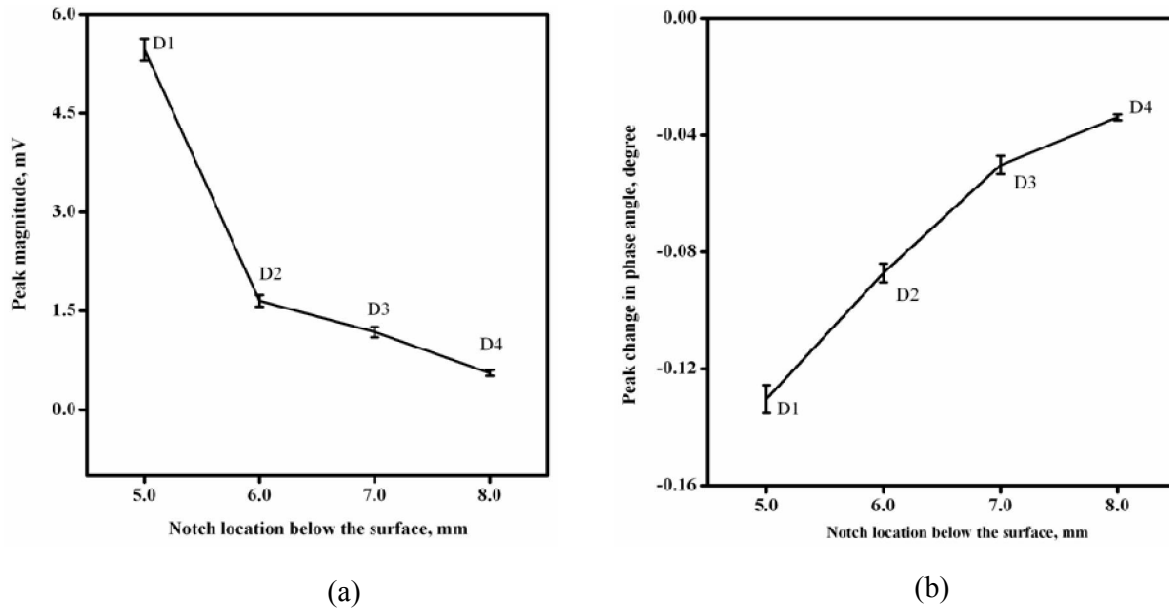


Figure 4.14: (a) Peak magnitude and (b) peak of change in phase angle of sub-surface notches.

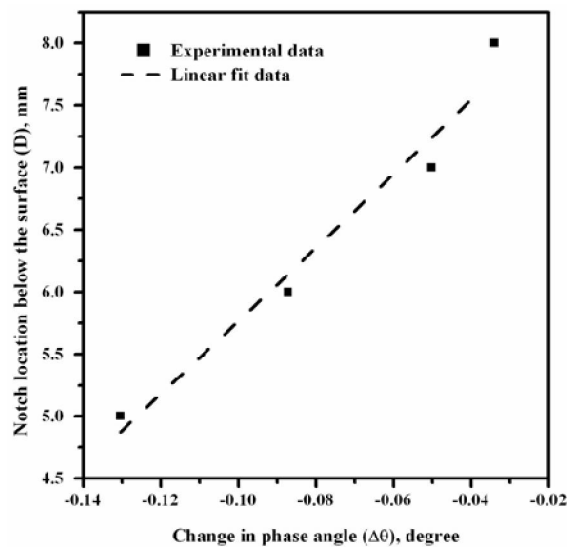


Figure 4.15: Linear behavior of notch location below the surface (D) as function of change in phase angle ($\Delta\theta$).

4.4.4.2 Comparison with commercial instrument

Response of the developed instrument has been compared with a commercial general purpose ECT instrument (TECHNOFOUR INSIS EX-4). This is a constant current instrument (300 mA). As the commercial instrument is not capable of measuring the absolute phase lag of the receiver coil

sinusoids, the magnitude signals have been compared. Figure 4.16 shows the change in phase angle of the developed instrument and the commercial instrument for sub-surface EDM notches shown in Figure 4.7 (b). As can be seen, the developed instrument could detect the notches up to a depth of 8.0 mm below the surface. On the contrary, only notch D1 could be detected by the commercial instrument. This enhanced sensitivity of the developed EC instrument is attributed to the higher excitation current of 550 mA and the accurate phase measurement capability using the lock-in based I/Q detection method.

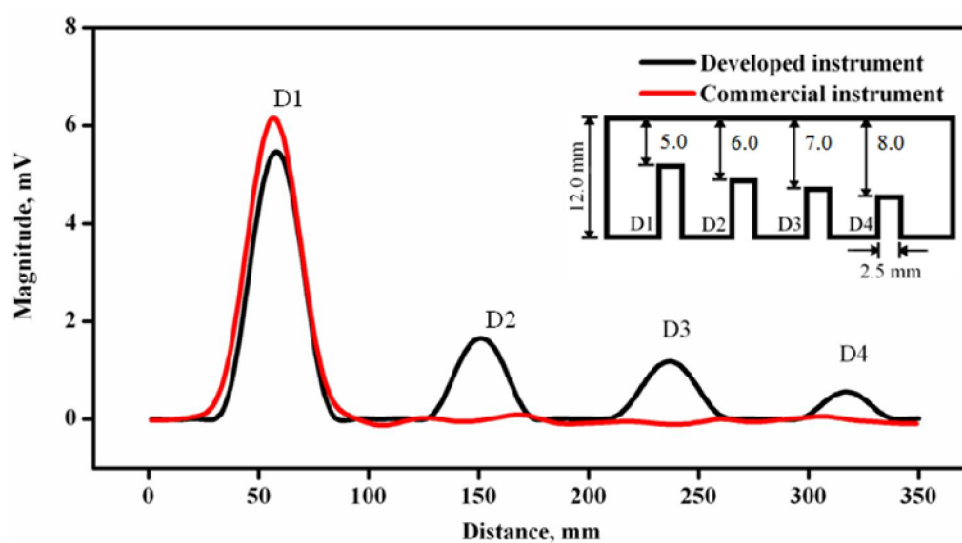


Figure 4.16: Comparison of detection performance of the proposed EC instrument with a commercial instrument.

4.5 Results and discussion

In order to demonstrate the performance of the developed instrument and cup-core probe for practical application, flat bottom holes (simulating sub-surface localised corrosion) and smaller notches (simulating sub-surface crack) are considered.

4.5.1 Sub-surface flat bottom holes

For simulating sub-surface localised corrosion on inside surface of storage vessel, four FBH are machined in a 12.0 mm thick SS plate and dimensions of the flat bottom holes are given in Table 4.2 and Figure 4.7 (a). Using the developed instrument and cup-core probe testing is performed at 5 kHz. Figure 4.17 shows the change in phase angle (difference of phase angle between flaw and flaw-free locations) for FBHs. From Figure 4.17 it is observed that the developed instrument and cup-core probe could detect the FBH located 8.0 mm below the surface with a vary good SNR and also exhibited a the linear change in phase angle with flaw depth. The result confirms the detection sensitivity of the developed instrument and EC probe for detection of simulated sub-surface localized corrosion. In the phase angle signals, the widths of all four FBHs are observed around 25.0 mm due to the convolution of point spread function of the EC probe with the FHBs.

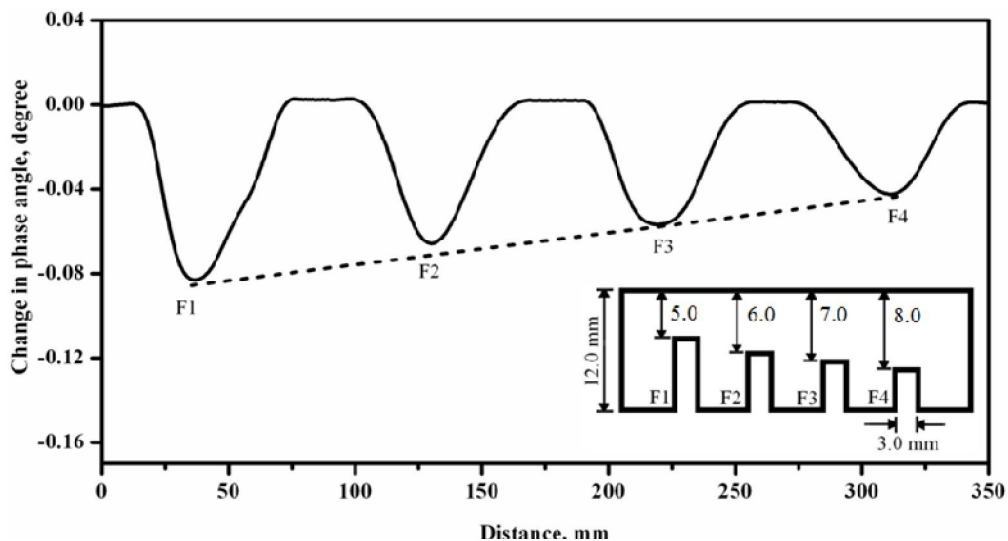


Figure 4.17: EC signal obtained for 3.0 mm diameter FBHs located at different depths (D) below the surface in a 12.0 mm thick SS plate.

4.5.2 Sub-surface notches

The response evaluation of the developed instrument and cup-core probe for detection of sub-surface cracks on the inner surface of the storage vessels smaller size artificial notches (width 1.0 mm,

length 20.0 mm) located at depths 4.0, 6.0 and 8.0 mm below the surface (detail given as D5, D6 and D7 in Table 4.1 and Figure 4.7 (c)) have been machined. The change in phase angle response is measured for these notches and the results are shown in Figure 4.18. As can be seen, the developed instrument and probe showed better detection sensitivity for smaller notches located at 8.0 mm below the surface i.e. D7 and can be used for detection of smaller simulated sub-surface cracks. From the Figure 4.18, it is also observed that, as depth (D) below the surface increases, the change in phase angle decreases linearly. This linear sensitivity and better detection sensitivity clearly ensure that the proposed instrument and cup-core probe can be employed for detection of inside corrosion and crack damage in 12.0 mm thick stainless steel storage vessels by scanning the probe on the outer surface. It should be noted that the SNR requirement of 3:1 would not be met for flaws which are buried deeper than 8.0 mm. In such situations it is essential to apply signal or image processing algorithms to improve the SNR.

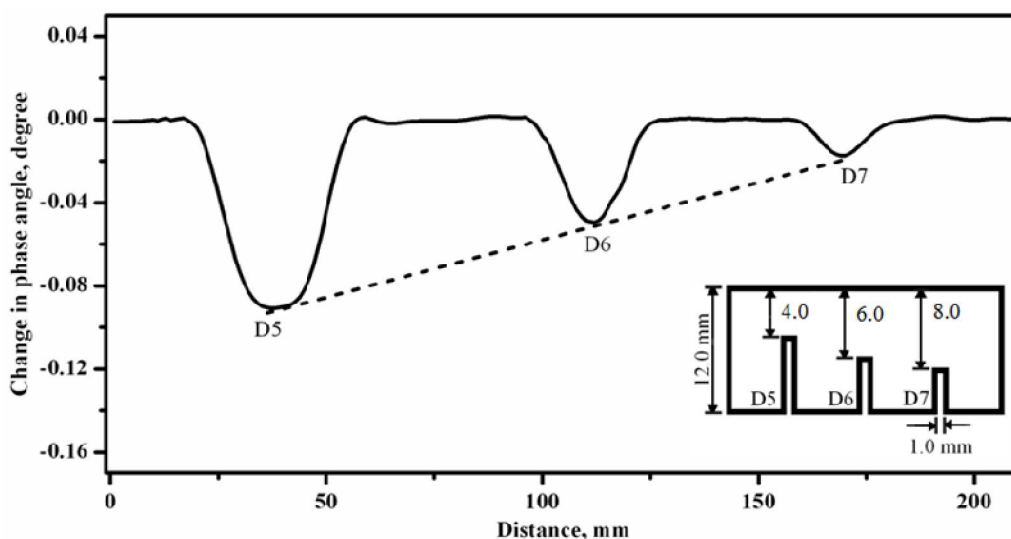


Figure 4.18: The EC signal obtained for sub-surface notches located at different depths (D) below the surface.

4.5.3 Surface flaws

In order to check the performance of the developed instrument and cup-core probe for detection of surface flaws, EDM notches of varying depths (4.0 mm, 6.0 mm and 8.0 mm, as given S3, S2 and S1

in Table 4.1) have been considered. Signals have been obtained by a line-scan of the probe over the flipped surface of the plate shown in Figure 4.7 (c). The measured phase angle response of the probe for the notches is shown in Figure 4.19. The instrument and probe detected all the three surface notches and change in phase angle is found to vary linearly with the notch depth. From Figure 4.18 and Figure 4.19, it is also evident that surface and sub-surface flaws are clearly distinguishable from the phase angle value, with a clear change in sign. This is highly beneficial in field applications, as it enables quick identification of surface and sub-surface flaws using a single probe.

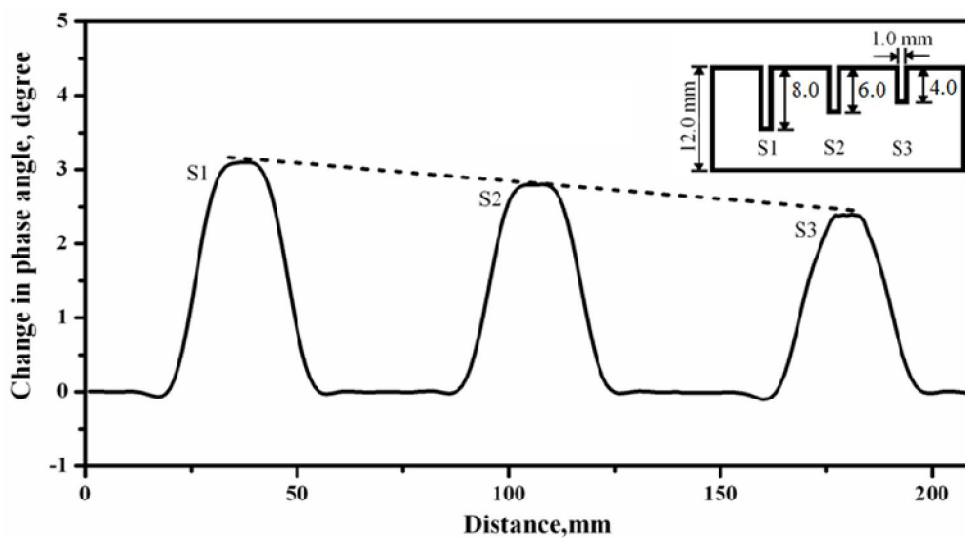


Figure 4.19: The EC signal is obtained for surface notches of varying depths ($d = 4.0, 6.0$ and 8.0 mm) notches.

These experimental results clearly reveal that the developed high sensitive instrument and cup-core probe are capable of detecting deep sub-surface flaws as well as surface breaking flaws in thick metallic materials. This enhanced detection sensitivity is due to the cup-core probe ensuring high intensity primary magnetic fields into the material and the precise phase angle measurement possibility using the lock-in amplifier approach.

4.6 Imaging of sub-surface flaws

In order to study the spatial extent of flaws, imaging of flaws has been carried out by raster scanning of the EC probe over the SS plate surface. For imaging of flaws, test specimen with four notches (as given D1, D2, D3 and D4 in Table 4.1) located at 5.0, 6.0, 7.0 and 8.0 mm below the surface are used. An automated scanning by using the developed instrument and XY scanner is performed and the magnitude and change in phase angle images of the notches are obtained by automated raster scanning. Figure 4.20 shows the magnitude and the phase angle images obtained for notches D1, D2, D3 and D4. From figure it is confirmed that the developed instrument has capability to detect the deep flaw located at 8.0 mm below the surface. The SNR of the images is found to be 5dB.

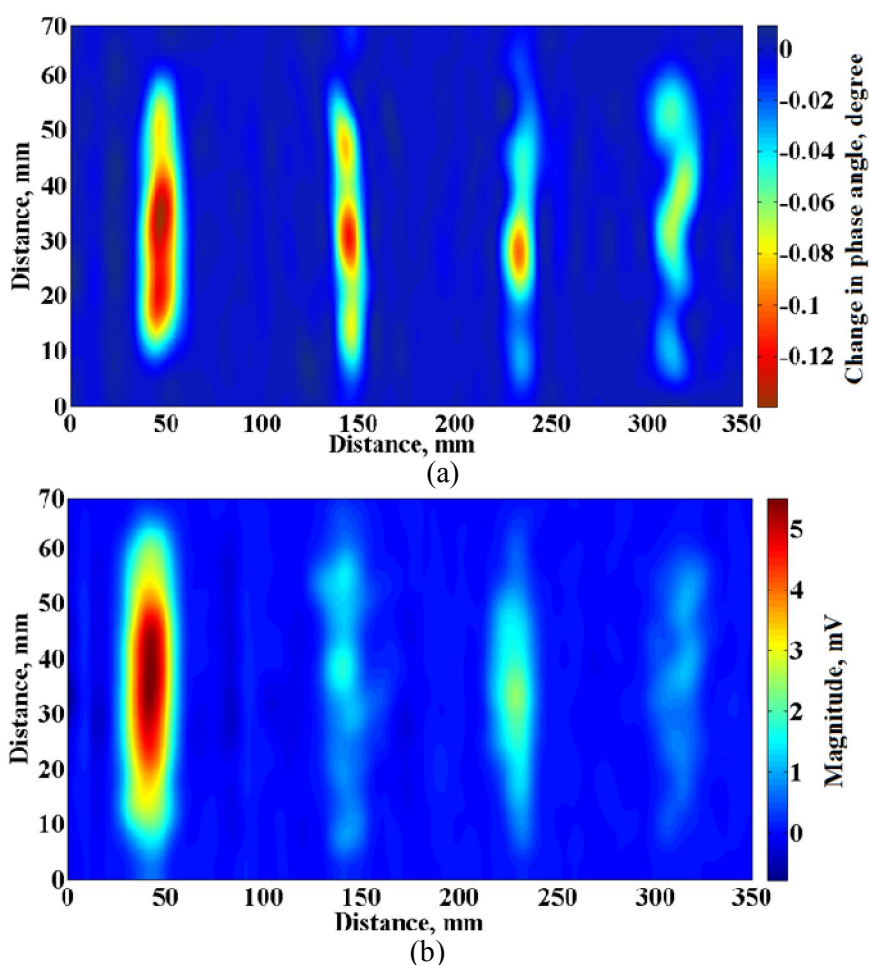


Figure 4.20: EC image of 4 sub-surface notches in SS plate (a) change in phase angle (b) magnitude.

From the EC images shown in Figure 4.20 presence of flaws can be observed. However, for reliable detection and sizing of flaws, this is a need to enhance the SNR and resolution in the EC images. For this purpose fusion of the images has been attempted and the details are discussed in Chapter 5.0.

4.7 Summary

A high sensitive eddy current instrument has been developed for detection of sub-surface flaws in 12.0 mm thick stainless steel plate. Systematic studies using the instrument reveal a definite improvement in the detection sensitivity, as a result of increase in the excitation current and by the use of precise phase angle measurement. The observed results are the following:

- For AISI 304L stainless steel plate of thickness 12.0 mm, an excitation current of 550 mA has ensured unambiguous detection of sub-surface notch located at 8.0 mm below the surface.
- The higher current driving capacity complied with the high dynamic range of the lock-in based I/Q detection method enabled detection of the sub-surface notches in 12.0 mm thick AISI 304L stainless steel plate.
- The developed instrument and probe resulted in a linear relationship between the depth below the surface and change in phase angle. This linear sensitivity facilitates accurate detection and sizing of deep sub-surface flaws with better resolution in the depth direction (thickness).
- This study established, for the first time, that it is possible to distinguish surface and sub-surface flaws from the change in the phase angle signals, as they are well separated in sign.
- The high sensitive eddy current instrument and cup-core type send-receive probe promise better sensitivity for detection of simulated sub-surface localized corrosion as well as simulated sub-surface crack.

Development of image fusion methodology

5

5.1 Preamble

This chapter presents a novel image fusion methodology for enhancing the detection capability of the proposed instrument and optimized probe. The methodology is based on the combined advantages of wavelet transform (time-frequency) and Bayesian (statistical) methodologies. The performance of the proposed fusion methodology has been compared with other existing fusion methodologies such as Laplacian pyramid, wavelet transform, PCA and Bayesian, based on image metrics such as standard deviation, SNR, entropy and fusion mutual information.

5.2 Image fusion

As explained in Section 1.3.7 wavelet transform fusion methodology is based on multi-resolution analysis, where the source images are decomposed into a set of sub-sampled images in spatial frequency. These sub-sampled images represent unique information at different frequency as well as resolution level and provide the information about edges of flaws in EC images (source image). These edges of flaw define the extent of flaw, which is essential for detection and characterization. Hence, application of wavelet transform based methodology is beneficial when the image contains reasonably well delineated frequency components between the desired features (flaw) and noise. Studies reveal that wavelet transform based fusion methodology when applied to EC images resulted in better localization of the flaws. However the improvement in SNR is not significant [33]. This is due to the fact that the noise does not have well defined frequency components. Statistical methodologies are attractive in this context.

The statistical inference based Bayesian fusion methodology provides a probability of hypothesis being true for given evidence or prior probability. The prior probability which is the prior information of the likelihood of the flaw and noise information in the images and is derived mostly based on expert knowledge. Determination of the prior probability is a key issue in the Bayesian methodology.

It should be noted that the EC images of sub-surface flaws are influenced by disturbing noise from various sources such as lift-off, material property and instrumentation. It is understood that the noise due to lift-off variations has well defined frequency components that are different from the flaw. On the other hand, the noise due to material property variations and instrument are random in nature. In addition to the noise having well defined frequency components, there exist randomness of the noise in EC images. Hence, the fusion methodology adopted should derive the mutual benefits of the time-frequency methods and statistical based methods towards enhancing the SNR of the EC images of sub-surface flaws. In this context, a new Bayesian and wavelet transformed (BayWT) based image fusion methodology that utilizes the advantages of the wavelet transform methodology as well as Bayesian based fusion methodology.

5.3 Proposed BayWT based image fusion methodology

The schematic block diagram of the proposed BayWT image fusion methodology is shown in Figure 5.1. In this methodology the source images are first decomposed into sub-sampled images by discrete wavelet transform (by using equation 1.14) as the sub-sampled images. These sub-sampled images provide the spectral information about the flaw location. This information is used for formulation the prior probability for the Bayesian based image fusion. For this purpose, a zero mean and unit standard deviation Gaussian function has been correlated with each sub-sampled wavelet images and correlated Gaussian function matrix is formulated as prior knowledge. This process would maximize the probabilities of detection of flaws, as a typical shape of flaw image is Gaussian

function. Subsequently, the sub-sampled images of corresponding decomposition levels are used as independent events with the likelihood of the images which is explained in the Section 1.3.7.3. These likelihood sub-sampled images are fused by the Bayesian methodology (by using equation 1.17) based on the formulated prior probability. Finally, the fused sub-sampled images are reconstructed using the inverse wavelet transform (by using equation 1.15). The steps involved in the implementation of the BayWT based fusion methodology are given in Table 5.1.

Table 5.1: Steps involved in the implementation of the BayWT based fusion methodology.

1. Generate the input EC images of flaws using two different frequencies.
2. **Wavelet transform:** Decompose the input images into the sub-sampled images at different levels using wavelet transform.
3. **Prior probability generation:** Predict the prior probability from the decomposed sub-sampled images of the flaws using normal Gaussian distribution with zero mean and unit standard deviation.
4. **Bayesian based fusion:** Perform Bayesian based fusion in sub-sampled images using the generated prior probability images.
5. **Inverse wavelet transform:** Perform the inverse wavelet transformed in the decomposed fused images to generate the fused images.

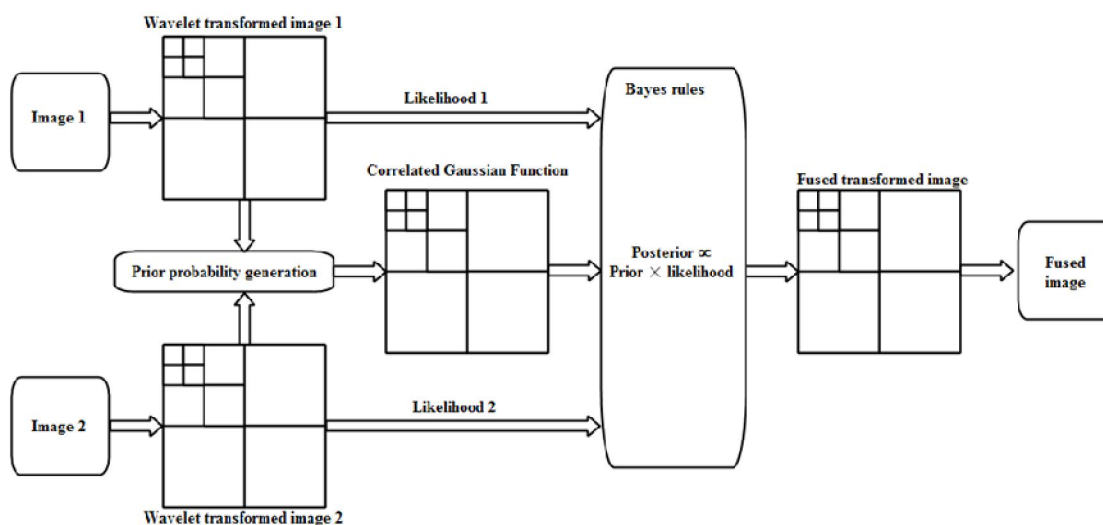


Figure 5.1: Block diagram of the proposed BayWT based image fusion methodology.

5.4 Input eddy current images

Image fusion studies have been carried out by using numerical model generated EC images of sub-surface flaws. The proposed image fusion methodology has been validated for one case, using experimentally generated EC images of a flaw.

CIVA software which is benchmarked numerical modeling software for NDE techniques has been used for generation of EC images of sub-surface flaws [93]. Using CIVA software, EC images of sub-surface notch of length 30.0 mm and width 2.5 mm with depths ranging from 5.0 mm to 8.0 mm below the surface of a 12.0 mm thick stainless steel plate have been predicted at 5 kHz and 7 kHz frequency for the optimized cup-core probe. Further, phase angle images of a sub-surface notch (D4) located 8.0 mm below the surface (as given in Figure 4.7 (b)) at frequency 5 kHz and 7 kHz have been generated using the developed ECT instrument and cup-core probe. These generated images have been used for evaluation of the proposed image fusion methodology. In order to simulate experimental noise, white Gaussian noise (noise level is 30% of the maximum amplitude) has been added to the model predicted images according to a predefined SNR.

5.5 Performance evaluation of BayWT image fusion

Performance evaluation of fusion methodologies are usually carried out based on two classes. First is the subjective evaluation metric, which depends on the human vision system (HVS). In this class, a qualitative assessment of the fused image based on the visibility of the features is made by human. Second class is the objective evaluation metrics. Objective metrics are quantitatively measure of the human perception. There are several metrics presents for assessments of the images objectively and they classified in to two categories, first one required a reference image while other do not [70,29]. For objective evaluation of the fused image, the following metrics have been used.

- 1) Standard deviation

- 2) Entropy
- 3) Signal-to-noise ratio (SNR)
- 4) Fusion mutual information (FMI).

Standard deviation, entropy and SNR metrics do not use reference image. But the Fusion mutual information metric use source images as reference.

5.5.1 Standard deviation

Standard deviation is a statistical quantity, which is used to measure the amount of variability or dispersion around the mean of the image. It is a measure of the image contrast and is defined as the square root of the variance as given in equation 5.1 below:

$$\text{Standard deviation } (\sigma) = \sqrt{\sum_{i=0}^M \sum_{j=0}^N \frac{(I(i,j) - \mu)^2}{MN}} \quad (5.1)$$

where

$$\mu = \frac{1}{MN} \sum_{i=0}^M \sum_{j=0}^N I(i,j) \quad (5.2)$$

where I is the image, μ is the mean of the image, M and N refers to the maximum number of pixels in the image in horizontal and vertical direction respectively and i and j are the indices which refers to the individual pixels of the image. Image contrast depends on the range of the data. An image with high contrast would have a high standard deviation, because of the higher dispersion (higher range of data) around the mean of the image.

5.5.2 Entropy

The entropy of an image describes the amount of information present in the image. The entropy (H) of the image is defined as

$$H = - \sum_{i=1}^M \sum_{j=1}^N P(i, j) \log_2 P(i, j) \quad (5.3)$$

where P is the probability of intensity at pixel level of image. Entropy is sensitive to noise and other unwanted rapid fluctuations in the image. Low entropy images have very little contrast and large number of redundant data. But the higher value of entropy shows the contrast in images and higher information content.

5.5.3 Signal-to-noise ratio

Definition of SNR generally depends on the application. In the present study, the SNR is defined as the ratio of mean or expected value of flaw signal (μ_{Signal}) to the standard deviation of the noise (σ_{noise}) in the image and define as:

$$SNR = 10 \log_{10} \frac{\mu_{Signal}}{\sigma_{noise}} \quad (5.4)$$

The SNR will tend to infinity when the flaw image is free from noise. Image with high SNR provides the better quality image. Hence, the image with high SNR value is preferred.

5.5.4 Fusion mutual information

Mutual information (MI) is a metric which is used to measure the degree of dependency of the two images A and B by measuring the distance between the joint distribution $P_{A,B}$ and the distribution associated with the case of complete independence $P_A P_B$. The amount of information corresponding to these features, calculated from the source images to the fused image, can be a suitable to evaluate the performance of the fusion methodology. The MI of two images A and B can define as:

$$MI(A, B) = \sum_{i=1}^M \sum_{j=1}^N P_{A,B}(i, j) \log_2 \left(\frac{P_{A,B}(i, j)}{P_A(i, j)P_B(i, j)} \right) \quad (5.5)$$

By this, dependency between the fused image and the source image can be measured independently. In this study, the mutual information of the fused image with source images A and B has been

computed independently and summed up to obtain the fusion mutual information (FMI) as shown in equation 5.6:

$$FMI(F, A, B) = MI(F, A) + MI(F, B) \quad (5.6)$$

where $MI(F, A)$ and $MI(F, B)$ are the individual mutual information between the fused image and the source image. Higher value of the FMI implies better quality of the fused image.

5.5.5 Results and discussion

Figure 5.2 shows the two model predicted noisy phase angle images of sub-surface flaws located at 8.0 mm below the surface in a 12.0 mm thick SS plate obtained at the excitation frequencies of 5 kHz and 7 kHz. White Gaussian noise has been added to the model predicted images (noise level is 30% of maximum phase angle), in order to represent the practical eddy current testing. The initial SNR of the images is computed to be 5.0 dB. The fused image is obtained as outlined in Section 5.3. Subsequently, two experimental images of the sub-surface flaw have also been generated at 5 kHz and 7 kHz frequency using developed high sensitive instrument and shown in Figure 5.3.

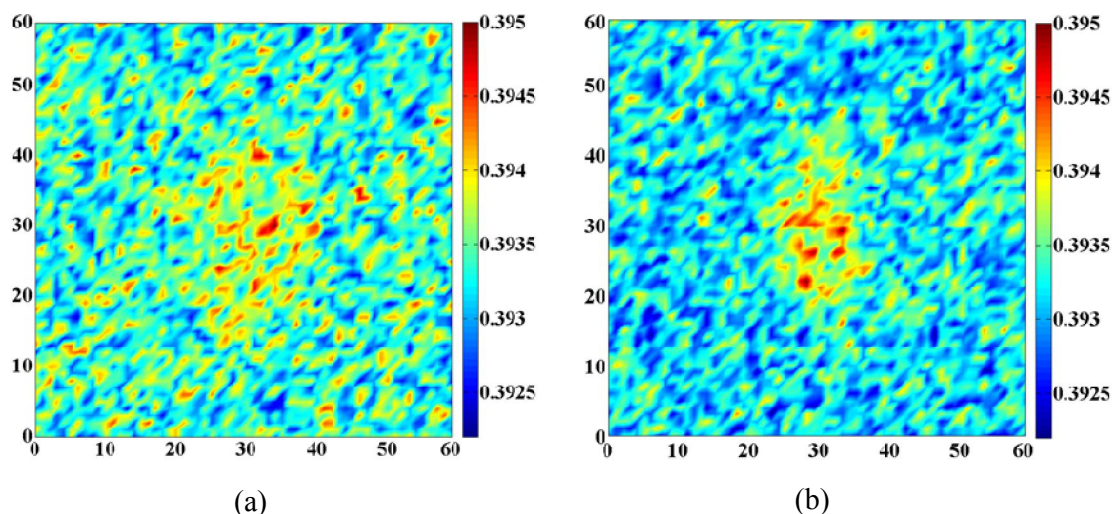


Figure 5.2: CIVA model predicted phase angle images of a sub-surface flaw located at 8.0 mm below the surface at frequency (a) 5 kHz and (b) 7 kHz with additive noise of 30% of maximum phase and SNR of 5 dB.

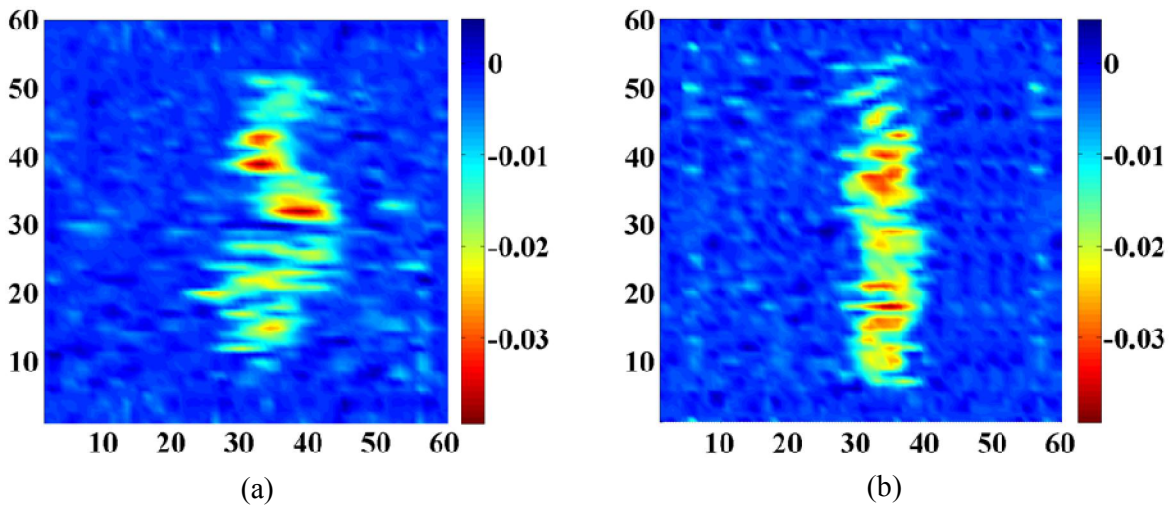


Figure 5.3: Experimentally obtained phase angle images of a sub-surface notch located at 8.0 mm below the surface at frequency (a) 5 kHz and (b) 7 kHz.

Figure 5.4 shows the fused model predicted and fused experimentally generated images of sub-surface flaw. From the results significant improvement in quality is evident in the fused image, this fused image is useful for flaw characterization and sizing. Further, for quality assessment of the proposed fusion methodology SNR, entropy and standard deviation of fused images have been determined and given in Table 5.2 and Table 5.3 for the model predicted and experimental images respectively. From the results it is noted that the BayWT based fusion methodology has shown significant improvement in all the three metrics. Three times enhancement has been observed in the SNR as compared to the input images. This enhancement of SNR shows the noise reduction capability of the proposed fusion methodology. The enhancement in entropy as well as standard deviation is also found to be higher for the fused image as compared to the input images. This shows the higher information about the sub-surface flaws in the fused image as compared to any of the input images.

Table 5.2: Assessment metrics of fused model predicted phase angle image.

S. No.	Image	SNR, dB	Standard deviation	Entropy
1.	Input image at 5 kHz	5.0	0.124	0.514
2.	Input image at 7 kHz	5.0	0.139	0.580
3.	Fused image	17.39	0.219	0.784

Table 5.3: Assessment metrics of fused experimental generated phase angle image.

S. No.	Image	SNR, dB	Standard deviation	Entropy
1.	Input image at 5 kHz	5.62	0.224	0.114
2.	Input image at 7 kHz	5.36	0.289	0.110
3.	Fused image	17.63	0.398	0.135

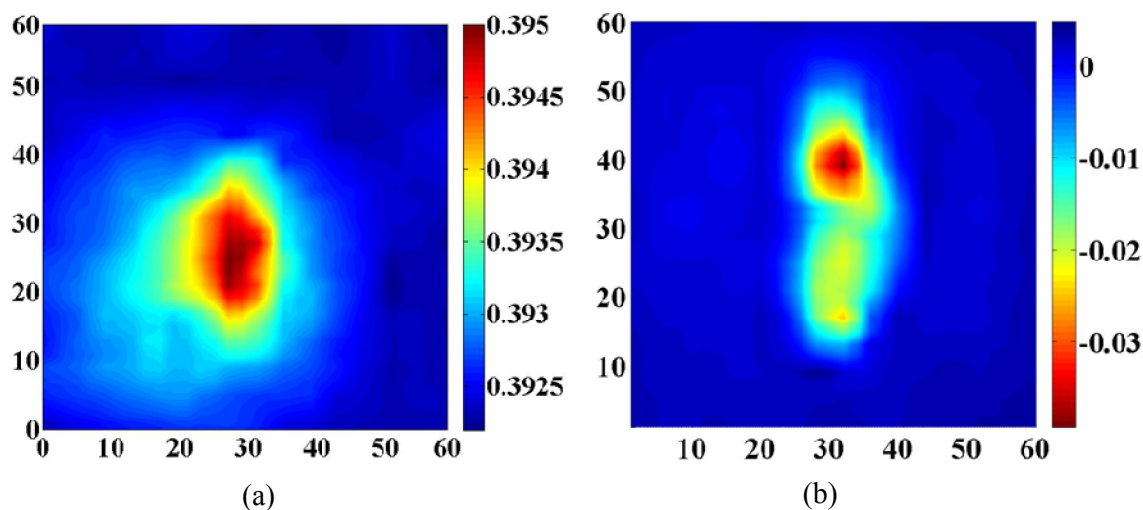


Figure 5.4: Fused phase angle images of sub-surface flaw located at 8.0 mm below the surface of (a) model predicted and (b) experimentally generated.

5.6 Comparison of performance of different fusion methodologies

The proposed BayWT methodology has been compared with the widely used fusion methodologies in ECT i.e. Laplacian pyramid, wavelet transformed, principal component analysis and Bayesian based fusion. For comparison of the performance of fusion methodologies, CIVA model predicted phase angle images of a sub-surface flaw shown in Figure 5.2 are fused using the four fusion methodologies. The results are shown in Figure 5.5. A good improvement in the quality of the images is observed after fusion by all the fusion methodologies. Table 5.4 shows the estimated evaluation metrics (i.e. SNR, entropy, standard deviation and fusion mutual information) of the model predicted fused images by different fusion methodologies. From Table 5.4 it is noted that the proposed BayWT based fusion methodology has shown significant improvement in all metrics as compared to the other fusion methodologies. Laplacian pyramid based fusion methodology has smoothened the effect of noise while decrease in noise has been found after wavelet fusion methodology. A SNR of 17.39 dB improvement is achieved by the proposed BayWT based fusion methodology. This is approximately three times the SNR of the input images (5.0 dB). The Bayesian, principal component analysis and wavelet transformed based fusion methodologies achieved SNR of 10.68, 8.48 and 6.74 dB respectively.

Table 5.4: Comparative performance of different fusion methodologies using model predicted phase angle images of a sub-surface flaw located 8.0 mm below the surface.

S. No.	Fusion Methodologies	SNR, dB	Standard deviation	Entropy	Fusion mutual information
1.	Laplacian pyramid	5.82	0.157	0.779	0.734
2.	Wavelet transform	6.74	0.192	0.755	0.771
3.	Principal components analysis	8.48	0.190	0.739	0.731
4.	Bayesian method	10.68	0.145	0.200	0.691
5.	BayWT method	17.39	0.219	0.784	0.808

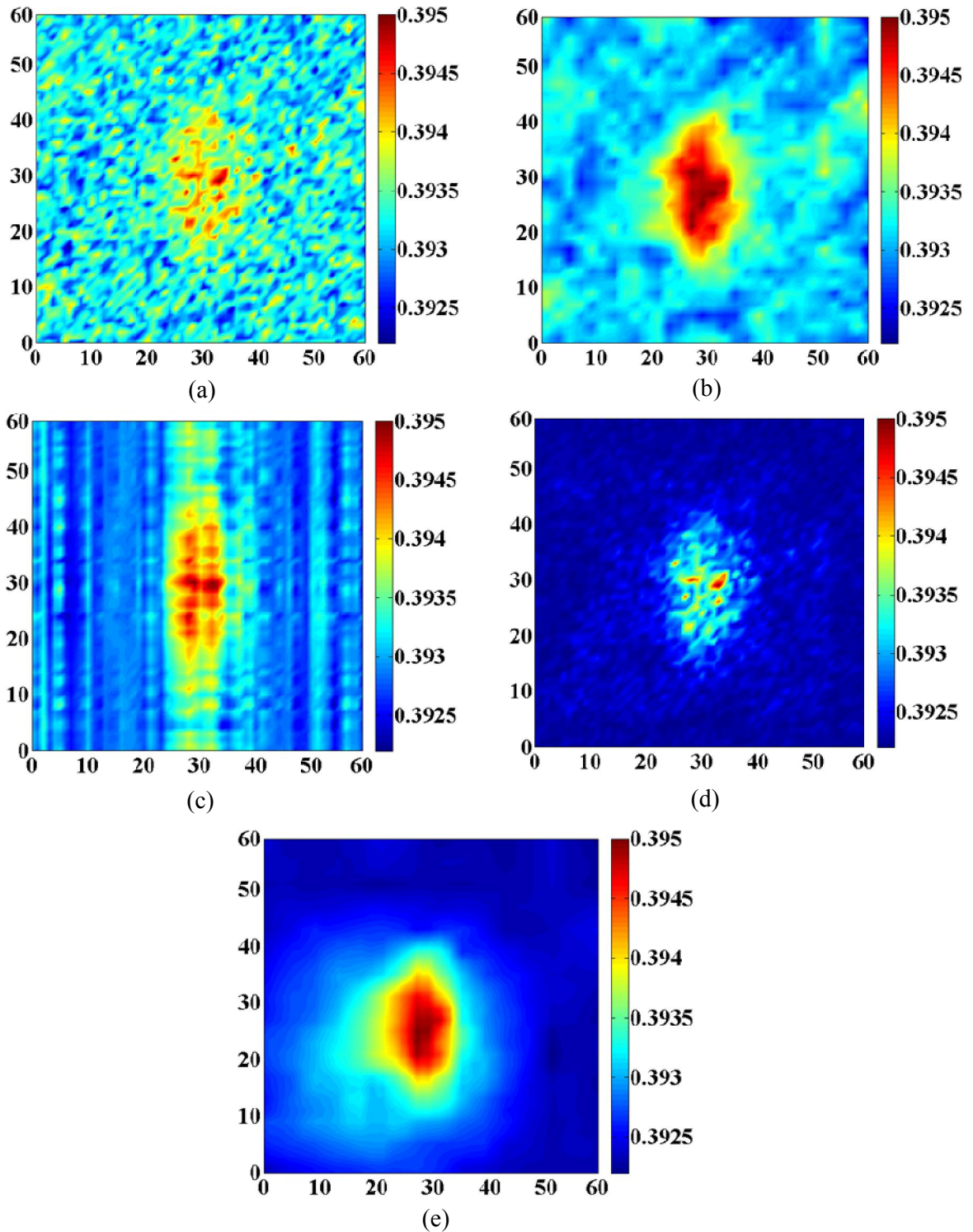


Figure 5.5: Fused phase angle images of different fusion methodologies (a) Laplacian pyramid (b) wavelet transform (c) principal component analysis (d) Bayesian method (e) BayWT method.

Further, the performance of image fusion methodologies have been studied for the experimental phase angle images generated by the developed instrument as shown in Figure 5.3. Figure 5.6 shows the results of different fusion methodologies. Table 5.5 shows the estimated evaluation metrics of the fused images by different fusion methodologies. The results clearly reveal that fusion of images shows significant enhancement than the raw experimental phase angle images. Like the model predicted images, 3 times enhancement in SNR is found for the BayWT based fusion methodology. A good improvement in standard deviation, entropy and fusion mutual information is found for the BayWT based image fusion methodology, as compared to the other fusion methodologies.

Table 5.5: Comparative performance of different fusion methodologies using experimental generated phase angle images of a sub-surface flaw located 8.0 mm below the surface.

S. No.	Fusion Methodologies	SNR, dB	Standard deviation	Entropy	Fusion mutual information
1.	Laplacian pyramid	6.02	0.324	0.123	0.802
2.	Wavelet transform	11.32	0.369	0.131	0.805
3.	Principal components analysis	10.43	0.384	0.119	0.797
4.	Bayesian method	12.51	0.125	0.116	0.814
5.	BayWT method	17.63	0.398	0.135	0.836

5.7 Summary

- A new fusion methodology that uses the mutual advantages of wavelet transform based time-frequency methodology and Bayesian statistical methodology has been proposed for the first time.
- The proposed BayWT image fusion methodology has shown significant improvement in the image quality metrics such as standard deviation, entropy, SNR and FMI.

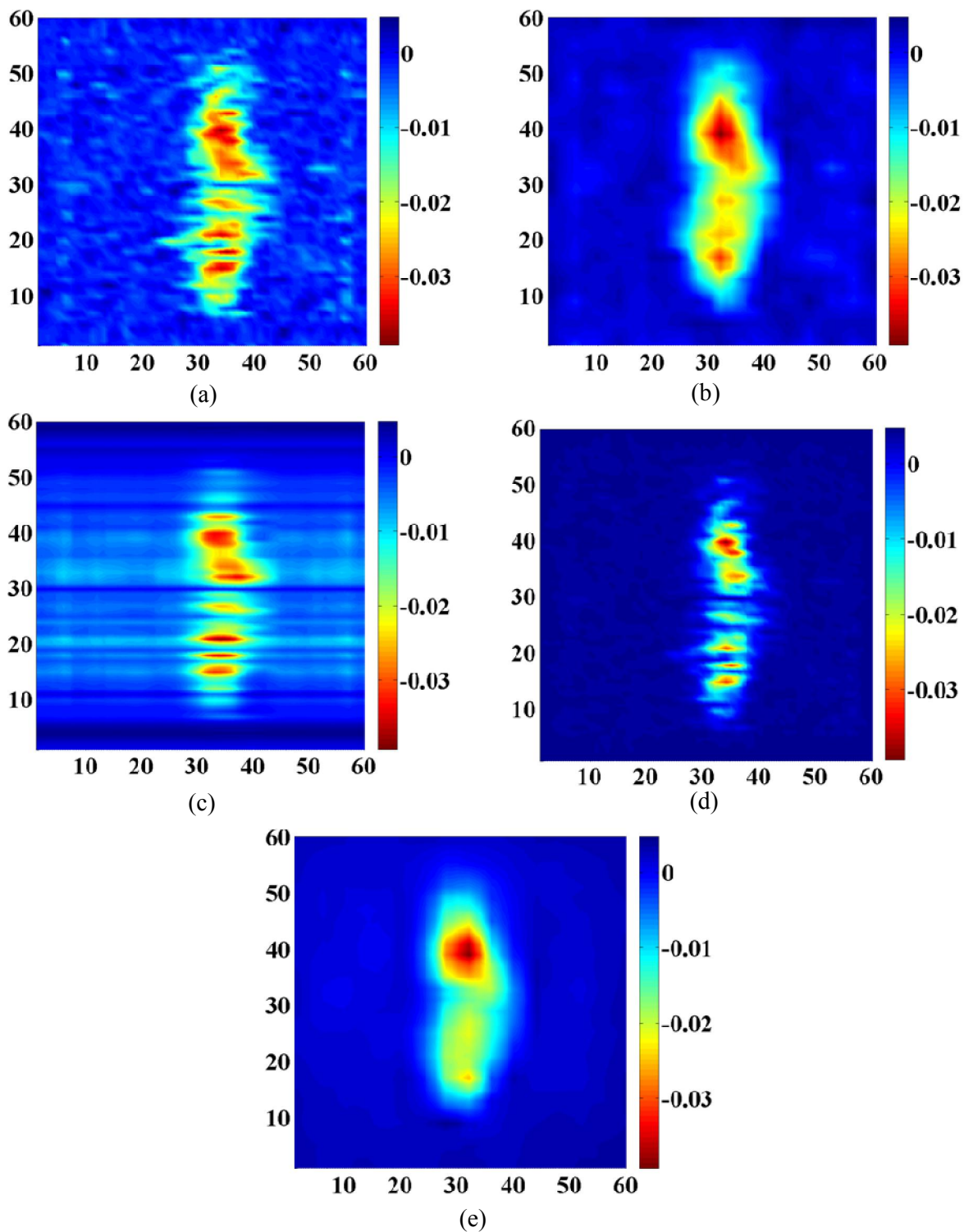


Figure 5.6: Fused phase angle images of different fusion methodologies (a) Laplacian pyramid (b) wavelet transform (c) principal component analysis (d) Bayesian method (e) Proposed BayWT method.

- In this methodology a new way to compute the prior probability has been proposed.
- The proposed BayWT based fusion methodology achieved a SNR of 17.63 dB, which is three times the SNR of the input images (5.0 dB).
- The image enhancement achieved through the proposed BayWT methodology has been found to be higher than that of the individual fusion methodologies viz. Laplace, wavelet, Bayesian and PCA.

6

Novel scan methodology for rapid detection and imaging of flaws

6.1 Preamble

This chapter elucidates the results of the studies made by comparing different scan plans viz. raster, diagonal raster, spiral, Lissajous, and billiard scan plans, towards identifying efficient and rapid scan plan for detecting and imaging of flaws in austenitic stainless steel plates. Numerical model based and experimental based studies carried out in this regard are also presented in this chapter.

It has been discussed in Section 1.2 and Section 1.4.4 imaging of larger area of the material is time taking process which is a harmful for inspection personnel in radioactive environment. Hence, rapid detection and imaging of flaw is preferred. As seen from the literature, in ECT raster scanning using single ECT probe and line scanning using array type ECT probe are used for detection and imaging. Although there are a few advantages of using raster scan plan or array ECT probe for detection and imaging, a few drawbacks limit its wide spread use. Rapid detection and imaging of flaws is also possible by scanning with single ECT probe but using different scan plans. This is employed in this chapter.

6.2 Parameters for rapid scan plans

Any scan plan using a single ECT probe is expected to meet the following criteria for fast and effective detection of flaws:

1. **Complete coverage:** the scan plan should cover the entire surface area.
2. **Rapidness:** the scan plan should cover the entire surface area in minimal possible time.

3. **Probability of detection:** the scan plan should detect all the flaws present in the scan area with good repeatability.
4. **Variable step size (Δ):** By increasing the step size, time for scanning decreases but probability of detection (POD) also decreases. Hence, a scan plan should use optimal step size without compromising the POD.

In this study, four different scan plans viz., 1) diagonal raster, 2) spiral, 3) Lissajous, and 4) billiard have been studied , for the first time, and their performances for a rectangular scan area have been analysed and compared with the conventional raster scan plan.

6.3 Description of the scan plans

6.3.1 Raster scan

Raster scan plan is commonly used in ECT to image flaws in plates. The raster scan can be either horizontal or vertical. In raster scan, the scan area contains N number of line segments (referred as scan lines) which are equally spaced with a constant step size (Δ) as shown in Figure 6.1. Raster scan is defined by the number of line segments and the number of steps in a line segment. For example, for a rectangular-shaped area of length (l) and width (w) with equal step size of Δ (i.e. $\Delta = \Delta_x = \Delta_y$) in both orthogonal directions can be described as

$$\text{Number of scan lines } (N) = \frac{l}{\Delta} \quad (6.1)$$

$$\text{Number of steps in one scan line } (S) = \frac{w}{\Delta} \quad (6.2)$$

$$\text{Total number of steps} = \frac{l \times w}{\Delta^2} \quad (6.3)$$

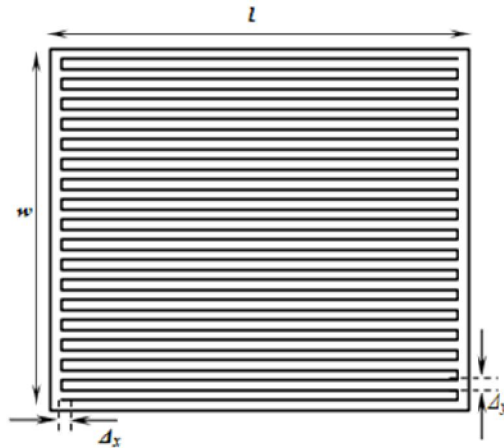


Figure 6.1: Raster scan pattern on the surface of a plate.

6.3.2 Diagonal raster scan

In a diagonal raster scan, the probe is moved along a diagonal line. When the probe hits the boundary of the scan area, it changes the orthogonal scan step by Δ and then moves along another diagonal line in the opposite direction, however, at same angle. In the diagonal raster scan, entire scan area of size $(l \times w)$ is divided into equally spaced elevation by Δ as shown in Figure 6.2. Diagonal raster scan is defined with the number of diagonal scan lines and the number of steps described as

$$\text{Number of diagonal scan lines } (N) = \frac{l + w}{\Delta\sqrt{2}} - 3 \quad (6.4)$$

$$\text{Total number of steps } (S) = \begin{cases} 2 \left[\left(\frac{N}{2} \right) \right]^2 + 4 \left[\left(\frac{N}{2} \right) \right] + N + 1, & \text{if } N \text{ is odd} \\ 2 \left[\left(\frac{N}{2} \right) \right]^2 + 2 \left[\left(\frac{N}{2} \right) \right] + N + 1, & \text{if } N \text{ is even} \end{cases} \quad (6.5)$$

6.3.3 Spiral scan

A spiral scan, also known as expanding square search, starts on either at the centre (outward spiral), or at a corner (inward spiral) of the rectangular scan area. Similar to the diagonal raster scan, entire scan area of size $(l \times w)$ is divided into equally spaced scan step, Δ . This generates different sizes of scan lines and shells (square) as shown in Figure 6.3. Like raster scan, in spiral scan plan the ECT

probe moves along a straight line, changes the scan direction by 90° clockwise (for inward spiral) or counter clockwise (for outward spiral) and then moves in another line with an increment of Δ . In spiral scan, the number of shells and number of scan lines can be determined for equal increment of Δ in both orthogonal directions by

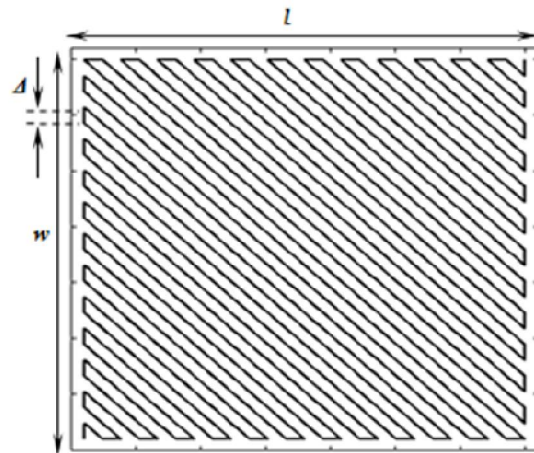


Figure 6.2: Diagonal raster scan plan on the surface of a plate.

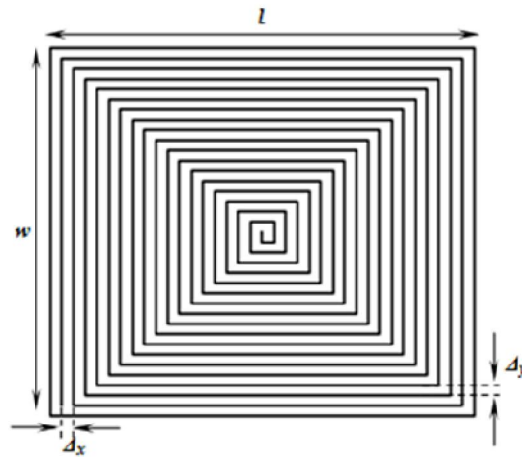


Figure 6.3: Spiral scan plan on the surface of a plate.

$$\text{Number of shells} = \begin{cases} l/2\Delta, & \text{if } l < w \\ w/2\Delta, & \text{if } l > w \\ l/2\Delta \text{ or } w/2\Delta, & \text{if } l = w \end{cases} \quad (6.6)$$

$$\text{Number of scan lines } (N) = \begin{cases} 2l/\Delta, & l < w \\ 2w/\Delta, & l > w \\ (l/\Delta + w/\Delta) - 1, & l = w \end{cases} \quad (6.7)$$

$$\text{Total number of steps } (S) = \frac{l \times w}{\Delta^2} \quad (6.8)$$

6.3.4 Lissajous scan

Lissajous scan is a non-linear smooth curve scan, investigated by Nathaniel Bowditch in 1815, and later in more detail by Jules Antoine Lissajous in 1857. Lissajous scan can be generated by independent oscillatory cosine function [94] defined as:

$$X(t) = X_0 \cos(\omega_x t) \quad (6.9)$$

$$Y(t) = Y_0 \cos(\omega_y t) \quad (6.10)$$

where $\omega_x = 2\pi f_x$, $\omega_y = 2\pi f_y$, is angular frequency and X_0, Y_0 are positive constant amplitude of the cosine signal. In Lissajous scan, the shape and probe coverage in a rectangular scan area $2X_0 \times 2Y_0$ is determined by the ratio of angular frequencies ω_x/ω_y in X and Y directions. Irrational ratios are preferred for non-repeating patterns with a perfect coverage over long time scales, as they provide same scanning speeds in X and Y directions and typical Lissajous scan plan on a surface is shown in Figure 6.4. Moves (step size, Δ) across the complete scan path are constant and this is defined by [83]:

$$\Delta = \frac{1}{2f_y} - \frac{1}{2f_x} \quad (6.11)$$

6.3.5 Billiard scan

Billiard scan discovered by C. Borys and C. D. Dowell, covers large fields in astronomy and is also known as ‘box scan’ [82]. In billiard scan, the probe movement starts at an angle (θ) inclined with respect to an edge and the move continues until the probe hits a boundary of the scan area. At the

boundary, change in direction takes place such that the angle of incidence is equal to the angle of reflection and the move continues back along the reflection line as shown in Figure 6.5. In billiard scan, coverage of the scan area is based on the angle of incidence and the move follows different paths for different θ . When θ is 45° , the billiard scan follows a repetitive path for a perfectly square scan area. Like the Lissajous scan, the billiard scan can also be generated using the co-ordinates determined by equations 6.9 and 6.10 with constant frequency as given by

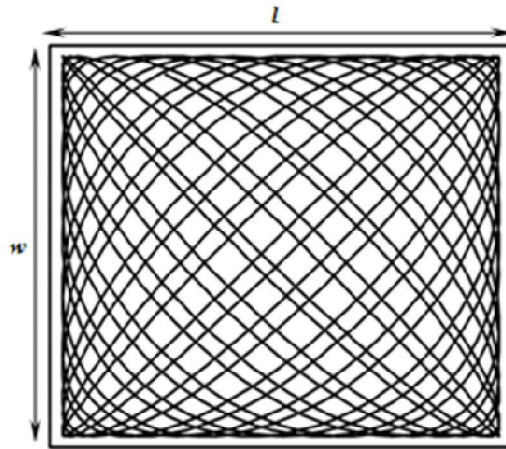


Figure 6.4: Lissajous scan plan on the surface of a plate.

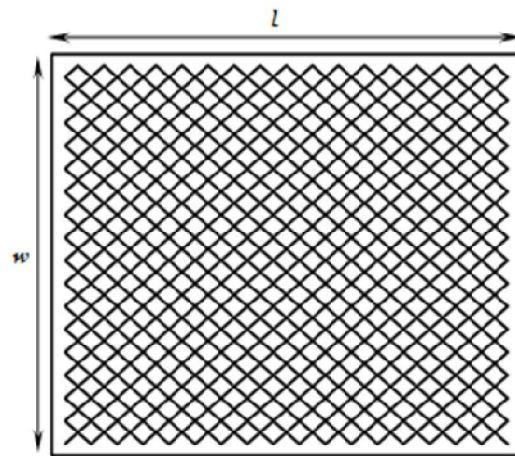


Figure 6.5: Billiard scan plan on the surface of a plate.

$$f_x = \frac{2a}{v \cos \theta} \quad (6.12)$$

$$f_y = \frac{2b}{v \sin \theta} \quad (6.13)$$

where a, b are the box sides, v is velocity and θ is angle [82].

6.4 Implementation of scan plans

6.4.1 Numerical investigations

Experimental studies on different scan plans for imaging of several numbers of flaws in different locations are time consuming and cumbersome. Hence, numerical investigations have been performed. EC images of flaws are a result of convolution of probe point spread function (PSF) with the flaw geometry [33]. In this study, the PSF of a cup-core probe has been obtained by using the CIVA simulation software [93]. In order to evaluate the scan plans considered in this study, a rectangular notch (length 30.0 mm and width 3.0 mm) is assumed to be present in an AISI type 304L stainless steel plate (360.0×360.0 mm²). Figure 6.6 shows the typical PSF of the 22.0 mm diameter cup-core probe optimised earlier and the EC image of the notch obtained using this probe.

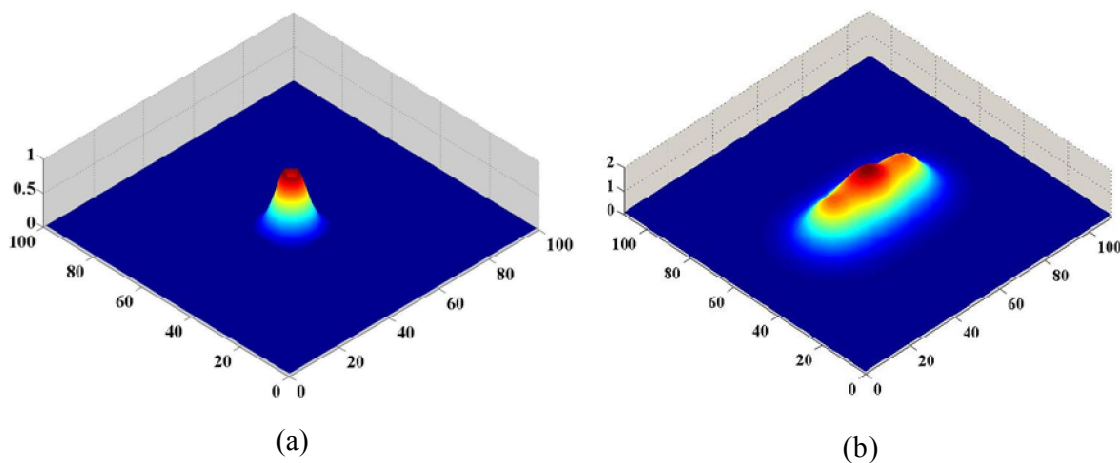


Figure 6.6: (a) Point spread function of eddy current probe and (b) image of a notch in test specimen.

EC image of the notch is obtained for the five scan plans. For the chosen probe, maximum probe response (impedance magnitude) is obtained when probe is located centrally over the notch. 10% of maximum probe response is considered as the threshold and detection of notch is confirmed when

the probe response is greater than the threshold. The complete coverage, rapidness, probability of detection and variable step size metrics have been evaluated for this notch located randomly at 1000 different locations on the plate surface. Figure 6.7 shows the 1000 random locations of the notch in either 0° or 90° orientations in the scanning area of $360.0 \times 360.0 \text{ mm}^2$

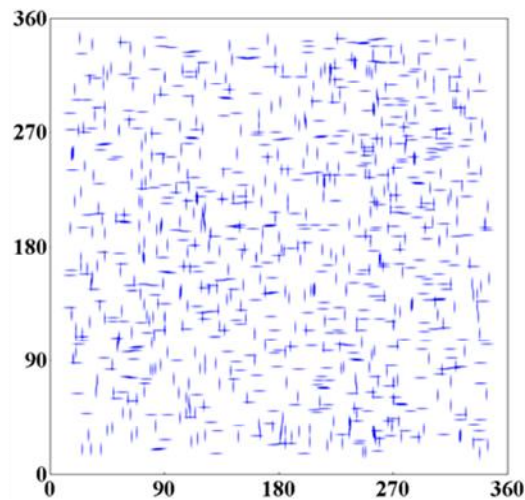


Figure 6.7: Scan region showing 1000 random locations of image of a modelled notch in SS plate.

6.4.2 Experimental verification

The experimental verification and comparison of the five scan plans have been carried out using the developed EC instrument and cup-core probe. For experiments automated scanning of the probe, for a specified scan plan and step size over the SS plate has been implemented in LabVIEW software and performance of all five scan plans has been evaluated. The flow graph of the automated scanning program is shown in Figure 6.8.

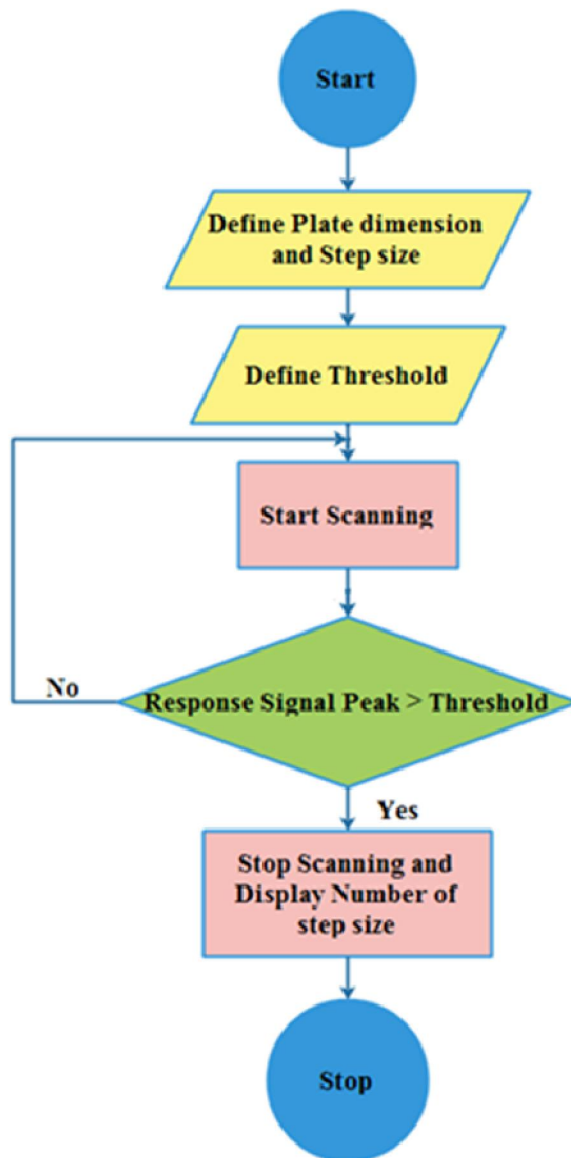


Figure 6.8: Flow graph of automated scanning program for detection of flaw.

For experimental evaluation of the rapid scan plans, two test specimen made of AISI type 304L SS plate of size $120.0 \times 120.0 \times 5.0 \text{ mm}^3$ with 13 artificial notches (length 10.0 mm and width 1.0 mm) in first plate and one notch at center in second plate are introduced by electro discharge machining as shown Figure 6.9.

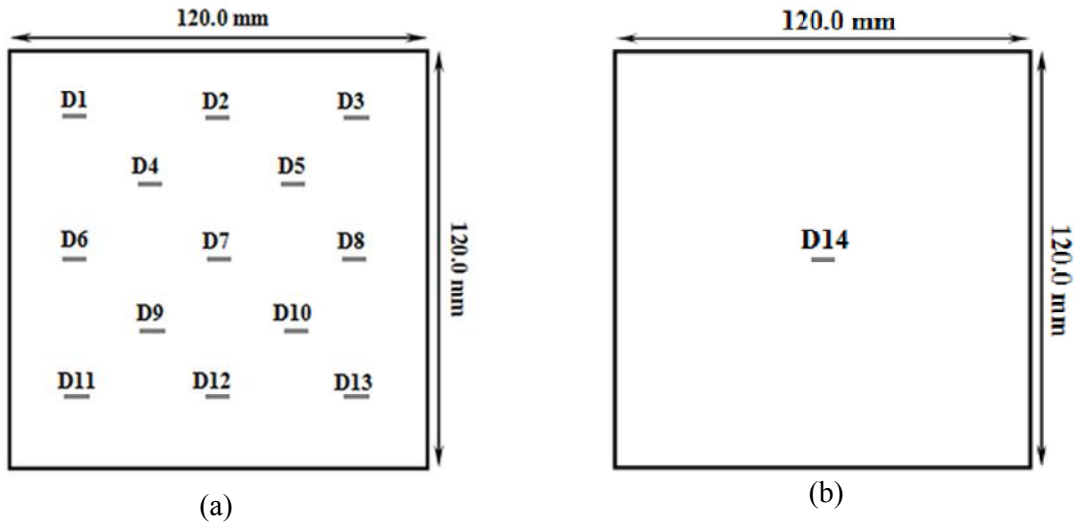


Figure 6.9: Schematic of the test specimen with notches for (a) rapidness analysis (b) imaging.

6.5 Assessment of rapid scan plans

6.5.1 Rapid detection of a flaw

For analysis of the rapidness of the scan plans, scanning is performed on 1000 random location of a notch at 5.0 mm step size which is the limiting step size [28] for the chosen cup-core probe. The number of steps required for the first-time detection (hit) of the notch is predicted. Table 6.1 shows the maximum number of steps required to detect all the 1000 notches by the five scan plans. Table 6.1 also shows the mean number of steps required for the first-time detection of 1000 notches. As can be seen, the billiard scan plan takes the least number of steps (maximum steps of 3406 and mean steps of 808) for detection of all the 1000 modelled notches, as compared to the other scan plans. Subsequently, the scatter plot of the number of steps required for detecting all 1000 modelled notches for the entire five scan plans are shown in Figure 6.10 and dotted line shows the average number of steps. It is clearly seen that, for raster, diagonal raster, and spiral scan plans, the number of steps required to detect all the 1000 modelled notches are randomly distributed in a range up to 4750 steps. However, most of the notches are detected within 3000 and 2000 steps for Lissajous and billiard scan plans respectively.

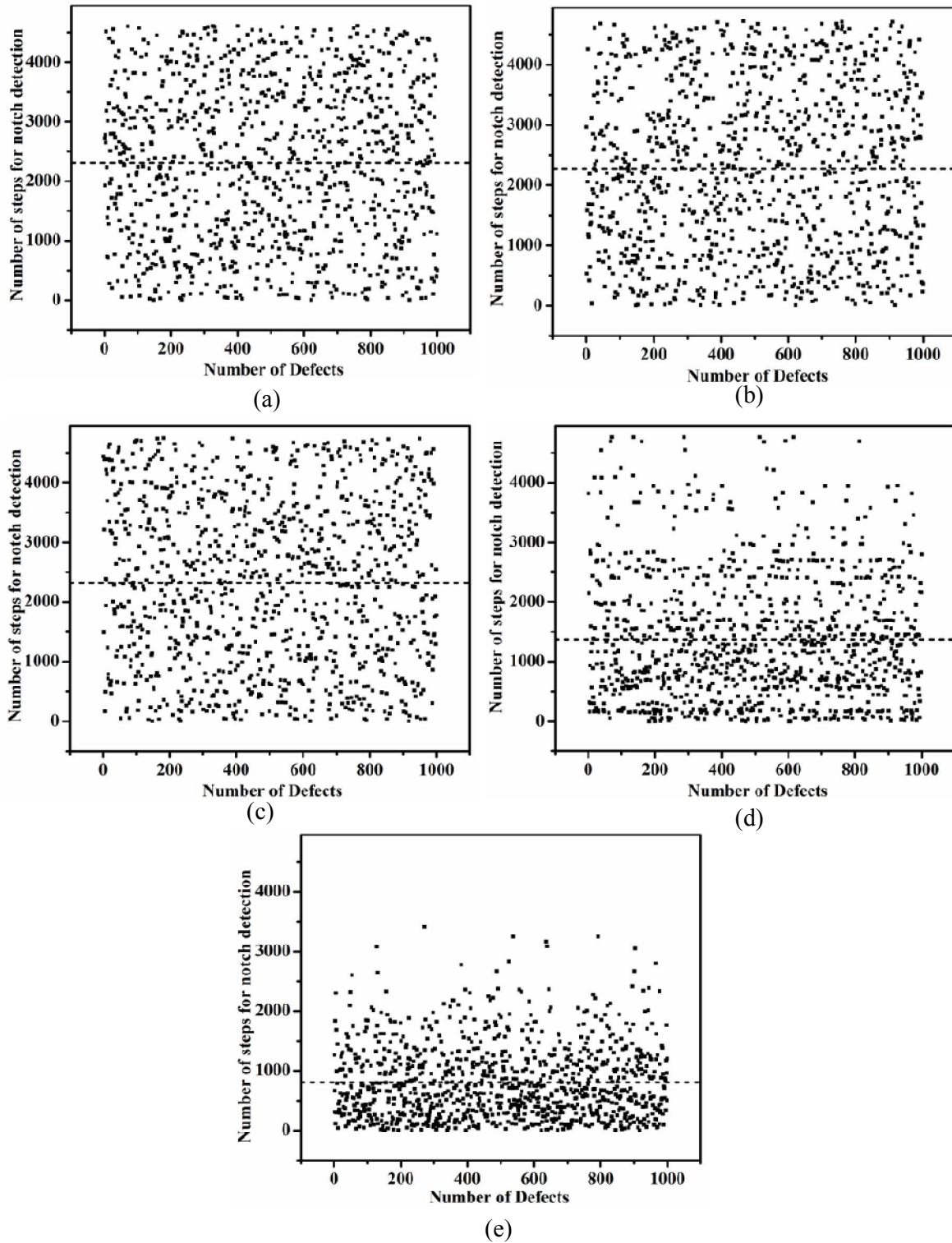


Figure 6.10: Scattering point of the number of steps required to detect all 1000 modelled notches using (a) raster (b) diagonal zigzag (c) spiral (d) Lissajous (e) billiard scan plans.

Table 6.1: Maximum and mean number of steps required by different scan plans for the first-time detection of 1000 notches at 5.0 mm step size.

S. No.	Scan Plan	Number of Steps Required	
		Maximum	Mean
1.	Raster	4710	2306
2.	Diagonal raster	4723	2277
3.	Spiral	4743	2315
4.	Lissajous	4661	1391
5.	Billiard	3406	808

To study the distribution of the steps required for detection of notches, box plot is plotted for all the five scan plans for all the 1000 modelled notches as shown in Figure 6.11. The Box plot represents the distribution of the number of steps required to detect all the 1000 modelled notches. In a box plot, central line in the box shows the median and circle shows the mean of the data. The box contains the distribution of data (number of steps) which comes in the range of $\pm\sigma$ (standard deviation), lower and upper boundary lines indicate the $\pm 1.5 \sigma$ value of the data and stars are the remaining data (outliers). Figure 6.11 reaffirms that, the distribution of the number of steps is random for raster, diagonal raster and spiral scan plans and more number of steps are required for detection of the notches. However, the σ value for Lissajous and billiard scan plans is small i.e. 1050.50 and 622.57 respectively as compared to the raster, diagonal raster and spiral scan plans i.e. 1319.9, 1356.1 and 1370.0 respectively. This indicates that the distribution of number of steps required to detect a notch is near to the mean. This study demonstrates that the billiard scan plan takes the least number of steps for detection of all the 1000 modelled notches as compared to the other scan plans.

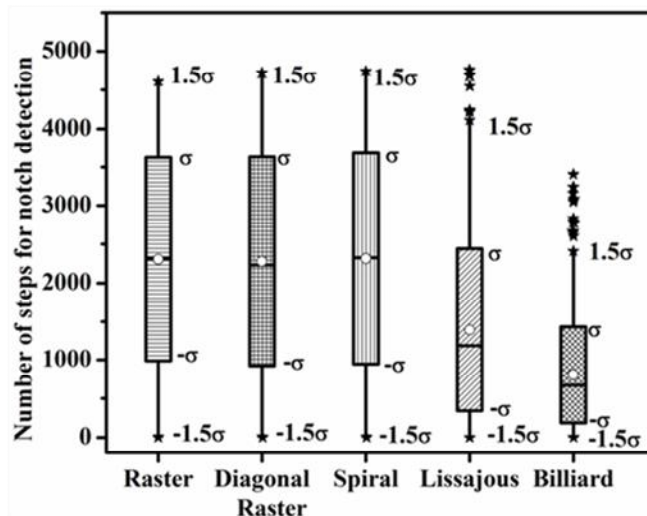


Figure 6.11: Box plot of the number of steps required to detect all 1000 modelled notches using all the five scan plans.

6.5.2 Complete coverage of scanning area

The scatter plots in Figure 6.10 show a uniform distribution of the notches with variation in the density depending on the scan plan. It is to be noted that the notches are detected when the number of steps are increased. Hence, the number of notches detected in every 50 steps (with a step size of 5.0 mm) is taken as a single bin and a bar plot is made for all the five scan plans and the results are shown in Figure 6.12 (a-e). It is clearly seen from Figure 6.12 that number of notches detected for raster, spiral and diagonal raster scan plans are equally distributed but for Lissajous and billiard scan plans, the number of notch detections are high for the initial bins and rapidly decrease as the number of steps increase. The percentage of the detection for the first 47 bins (mid point of total steps, shown in Figure 6.12 as dotted line) is calculated to check the area covered by the scan plans. The Raster, diagonal raster and spiral scan plans achieved around 50.0% notch detections for the first 47 bins i.e. (47×50) steps. The Lissajous scan plan achieved 79.8% notch detected at the half way mark, while the billiard scan plan achieved 98.0% notch detections at the same point.

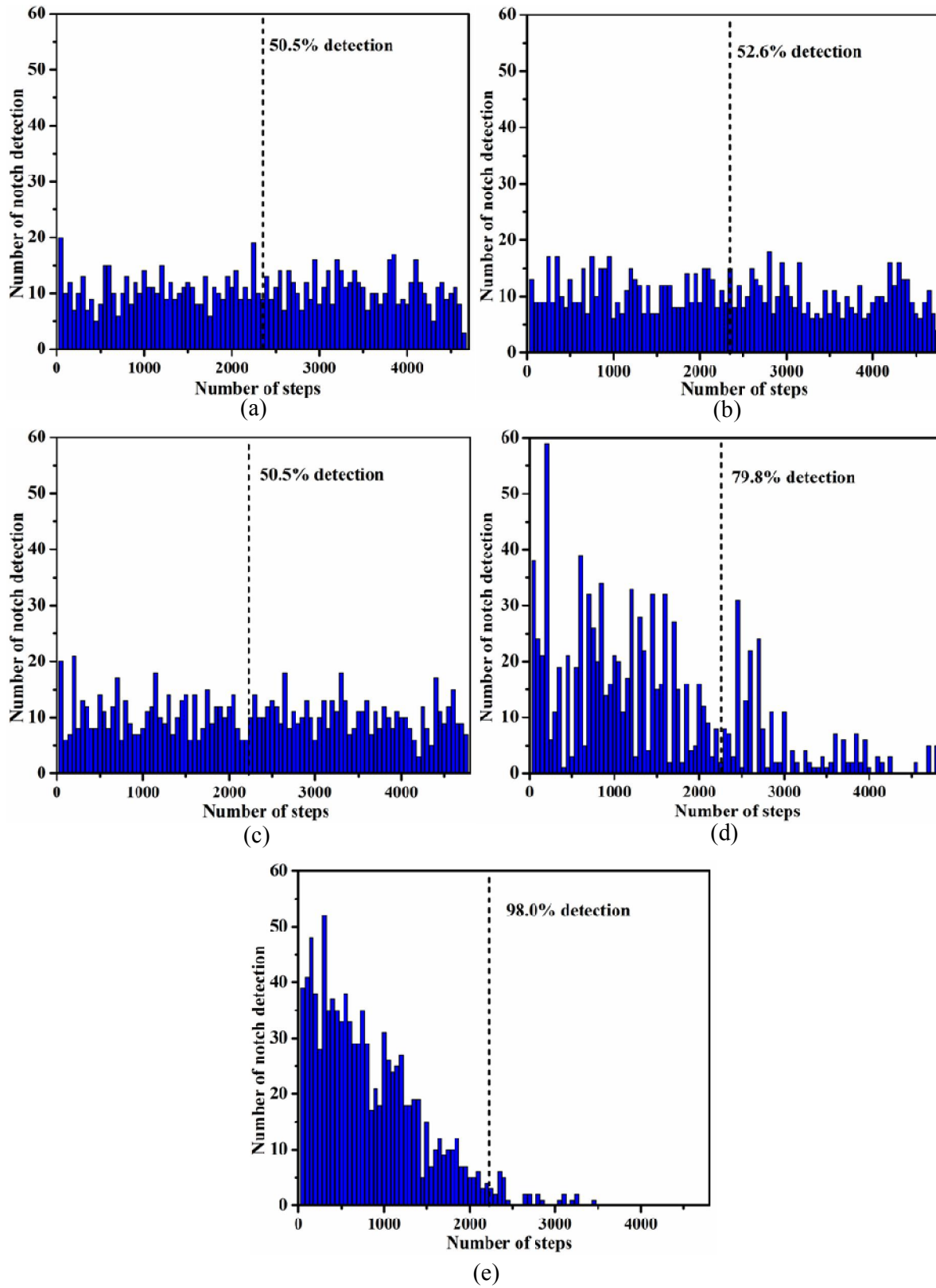


Figure 6.12: Number of notch detections by (a) raster (b) diagonal zigzag (c) spiral (d) Lissajous and (e) billiard scan plans.

Further, the percentage of notches detected as a function of the number of steps is estimated for all the five scan plans at 5.0 mm step size and the results are shown in Figure 6.13. As can be seen, the percentage of notches detected for raster, spiral, and diagonal raster scan plans increases linearly. However, for the Lissajous and billiard scan plans the percentage of notches detected increases exponentially and becomes near 100% and then, saturates. In Figure 6.13, X and Y are shown as the saturation points for the billiard and the Lissajous scan plans respectively and Z as the final point for the raster, diagonal raster, and spiral scan plans. It is observed that raster, diagonal raster, and spiral scan plans take longer time for attaining the Z point. While Lissajous scan plan reached the Y point at 3840 number of steps and the billiard scan plan reached the X point at 2400 number of steps. Subsequently, the percentage of notches detected is calculated at 2400 number of steps shown by vertical dotted line in Figure 6.13 for all the 5 scan plans and found that the raster, diagonal raster and spiral scan plans achieved only 50.0% detection at 2400 steps. While the Lissajous scan plan achieved 80.1% detection, the billiard scan plan recorded 98.5% detection. From the results, it is clear that the billiard and the Lissajous scan plans ensure rapid detection of flaws.

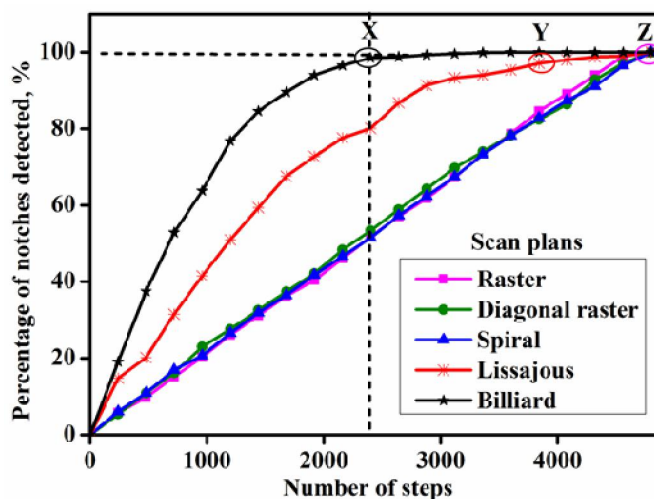


Figure 6.13: Percentage of notches detected by different scan plans.

6.5.3 Step size for detection of flaw

Systematic studies have been performed to investigate the influence of step size on flaw detection for all the five scan plans. For this study, step sizes of 3.0 mm, 5.0 mm, 7.0 mm and 10.0 mm are considered and the number of steps required for notch detection is calculated for all the five scan plans. The resulting box plot is shown in Figure 6.14 (a-d). Table 6.2 and Table 6.3 show the mean and standard deviation of the box plot for steps required for first time detection of notches respectively. From the result, it is observed that the mean and standard deviation value for billiard and Lissajous scan plans is less as compared to the raster, diagonal raster and spiral scan plans for all step size i.e. 3.0, 5.0, 7.0 and 10.0 mm. However, as the step size increases the performance of billiard and Lissajous scan plans decreases. However, the lower value of standard deviation shows that the distribution of number of steps required to detect the notches is near to the mean. Hence, from the result it is inferred that billiard and Lissajous scan plans perform faster as compared to the raster, diagonal raster and spiral scan plans. In view of this, billiard and Lissajous scan plans are selected for further investigations.

Table 6.2: Mean value of the number of steps required for first time detection of notches at different step sizes.

Step size, mm	Raster	Diagonal raster	Spiral	Lissajous	Billiard
3.0	6210	6276	5894	3935	3538
5.0	2306	2277	2315	1391	808
7.0	1249	1228	1284	747	605
10.0	599	591	644	479	421

Table 6.3: Standard deviation value of the number of steps required for first time detection of notches at different step sizes.

Step size, mm	Raster	Diagonal raster	Spiral	Lissajous	Billiard
3.0	3684	3789	3940	3057	2683
5.0	1319	1356	1370	1050	622
7.0	681	699	681	586	474
10.0	335	340	333	356	304

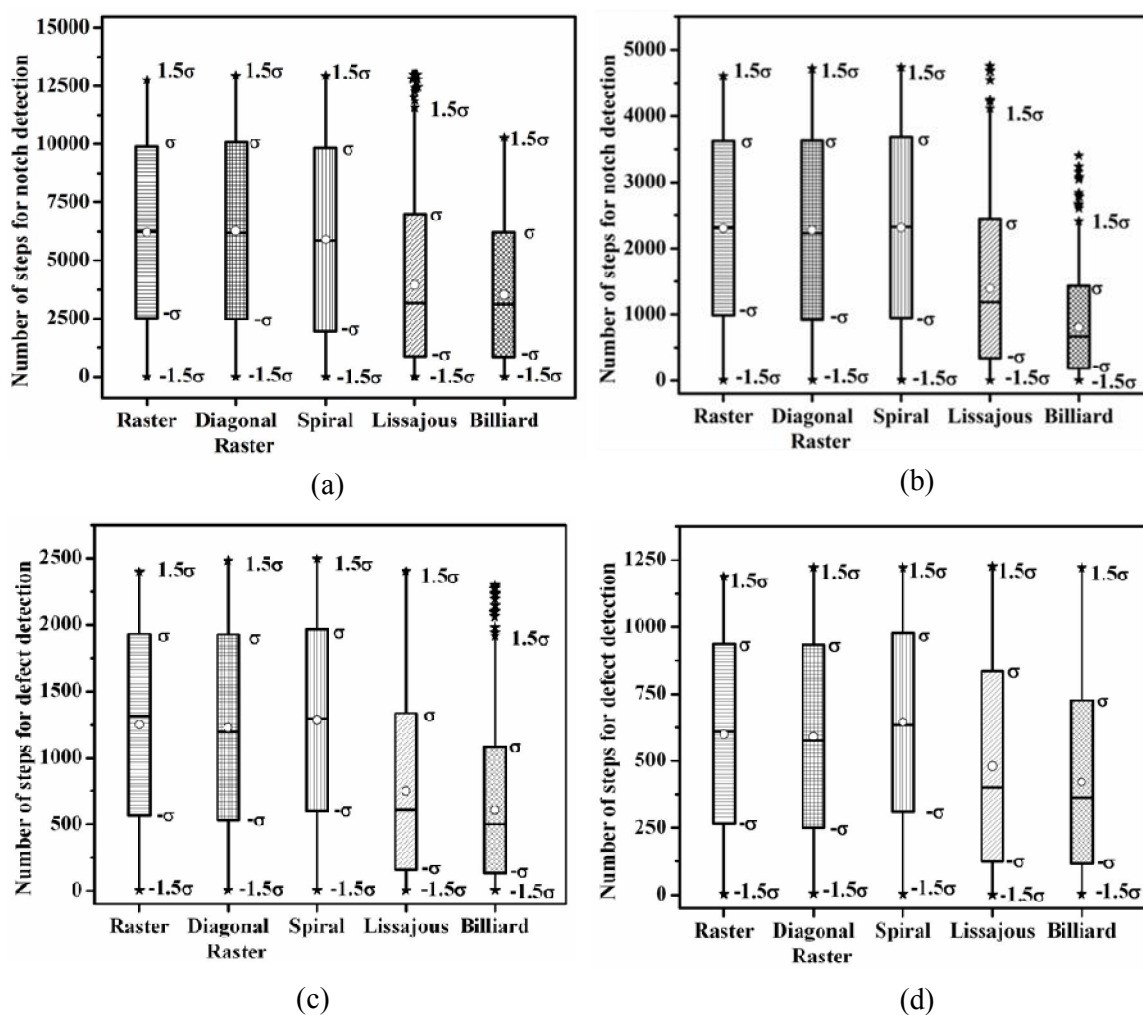


Figure 6.14: Box plot of the number of steps required to detect all the 1000 modelled notches by different scan plans at a step size of (a) 3.0 mm (b) 5.0 mm (c) 7.0 mm and (c) 10.0 mm.

6.6 Billiard scan plan

6.6.1 Influence of notch location

For understanding the area coverage and notches missed during the scan, studies are carried out using Lissajous and the billiard scan plans. Figure 6.15 (a) shows the Lissajous scan plan with an overlay of location of undetected notches. As can be seen, the Lissajous scan plan spends longer time on the edges relative to the center of the pattern. However, the billiard scan plan covers uniformly across the entire scan area as shown in Figure 6.15 (b) and detects the notches including those missed by the Lissajous scan plan. This study demonstrates that although the Lissajous scan plan is rapid, there is a possibility that some of flaws present in the central regions of object would be missed. This reaffirms that the billiard scan plan ensures full uniform coverage with rapidness and 100% POD.

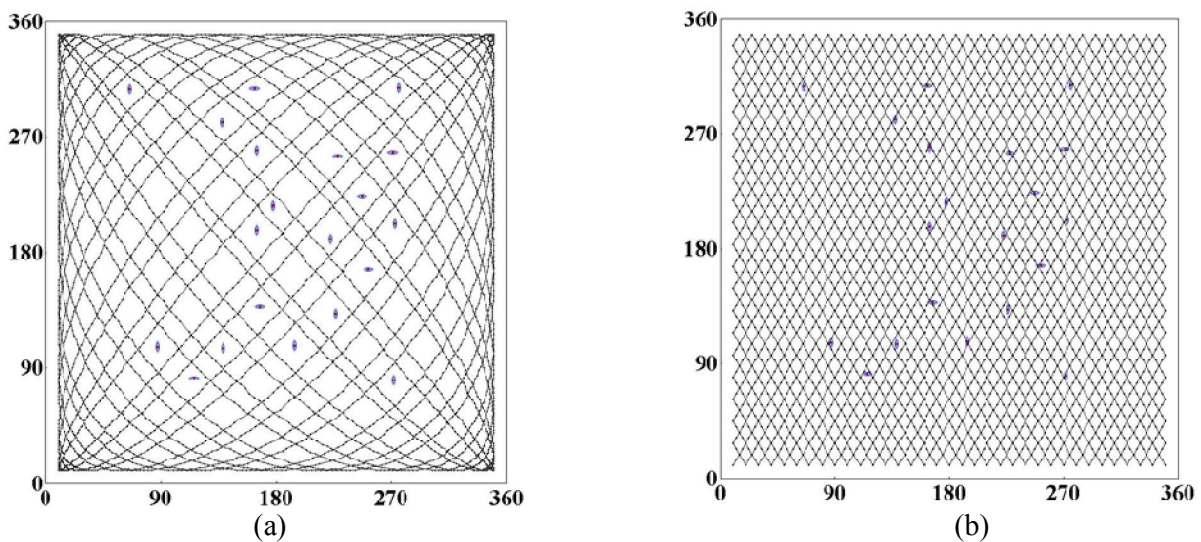


Figure 6.15: Missing location of notches in modelled test specimen and coverage of the scan plans (a) Lissajous (b) billiard.

6.6.2 Influence of notch dimensions

The length of notch is important for detection by ECT technique. To study the effect of notch length on billiard and Lissajous scan plans, three notches of different lengths 10.0, 20.0 and 30.0 mm are

modelled and percentage of notches detected is estimated at 5.0 mm step size. As seen in Figure 6.16, as the notch length increases the percentage of notches detected for 1000 random notch location increases for both the Lissajous and the billiard scan plans. Points X, Y and Z are the saturation points for notch lengths 10.0, 20.0 and 30.0 mm respectively for the billiard scan plan. The number of steps for saturation decreases with increase in notch length for the billiard scan plan. The percentage of notches detected is higher for the billiard scan plan as compared to the Lissajous scan plan for all the three lengths. Hence, the billiard scan plan is suitable for detection of short length notches i.e. 10.0 mm length.

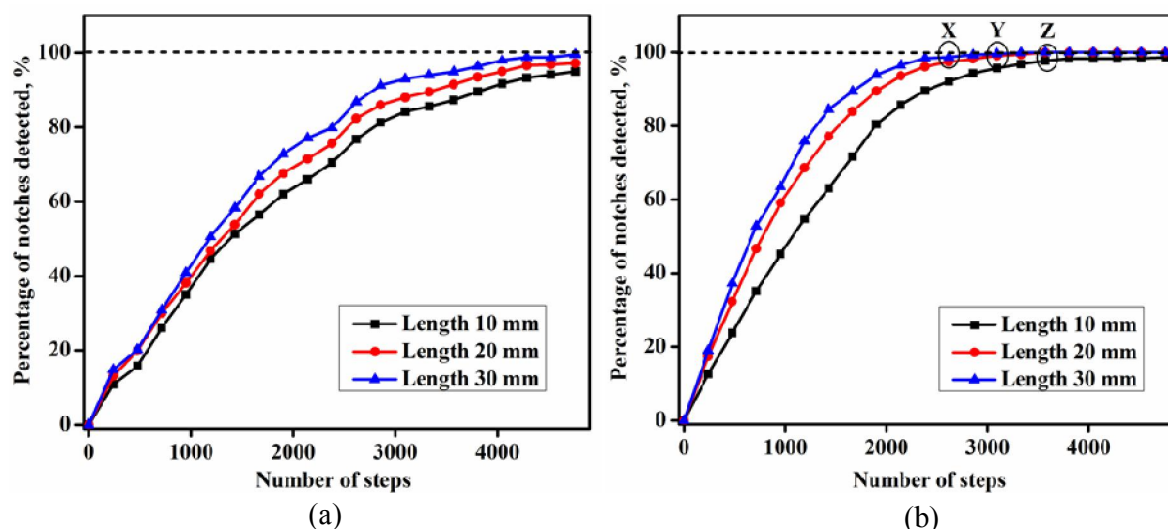


Figure 6.16: Detection of notches with different length of notches for (a) Lissajous scan plan (b) billiard scan plan.

6.6.3 Influence of angle of incidence

Initial angle of incidence (θ) is important for the billiard scan plan. A systematic study has been carried out to analyse this. For selection of the optimum angle of incidence for the billiard scan plan, different angle viz. 5° , 15° , 25° , 35° and 44° are chosen and analysis is performed by scanning the 1000 modelled location of notches at 5.0 mm step size. Percentage of notches detected for these angles are calculated and the results are shown in Figure 6.17. It is clearly seen that for 2400 scan steps (dotted line shown in Figure 6.17), the percentage of notch detection is 80.0%, 93.0%, 95.0% ,

99% and 85.0% for 5°, 15°, 25°, 35° and 44° of incidence angle respectively. Clearly seen that 35° degree incidence angle showed faster detection of notches. Hence, 35° incidence angle is chosen as the optimum angle of incidence for the billiard scan plan.

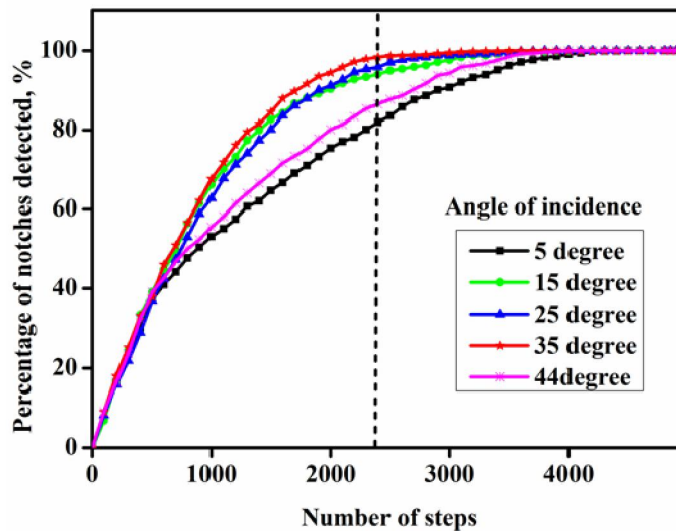


Figure 6.17: Percentage of notch detection for the billiard scan plan at different angles of incidence.

6.6.4 Step size for the billiard scan plan

Systematic studies have also been performed to study the effect of step size on flaw detection, rapidness, and area coverage. For this study, step sizes of 5.0 mm, 7.0 mm and 10.0 mm are considered and the distance travelled to detect a notch (product of number of steps and step size) is calculated. The number of notches detected in every 200.0 mm distance is counted as a single bin and the results are presented as a bar plot as shown in Figure 6.18(a-c) for step sizes of 5.0 mm, 7.0 mm and 10.0 mm. It is clearly seen from the Figure 6.18(a-c) that the number of notches detected is high for the initial bins and later it decreases rapidly. The percentage detection for the first 60 bins is calculated to compare the area covered by the billiard scan at different step sizes. For the step sizes 5.0 mm and 7.0 mm, the percentage detection is found to be 98.6% and 97.0% respectively while it is 100% for the scan step size of 10.0 mm.

The box plot of all the three step sizes is plotted as shown in Figure 6.19. Box plots represent the distribution of the number of steps required to detect all the 1000 modelled notches. The box plots confirm that the billiard scan plan with 10.0 mm step size is able to detect all the notches rapidly as compared to other step sizes. However, step size of 5.0 mm or less is preferred for imaging flaws with high resolution and to detect smaller flaws. Numerical investigations have clearly revealed that the billiard scan plan is superior in terms of rapidness, area coverage and variable step size metrics. Hence, it is advantages to use billiard scan plan for large area inspection of metallic plates in a rapid and reliable manner.

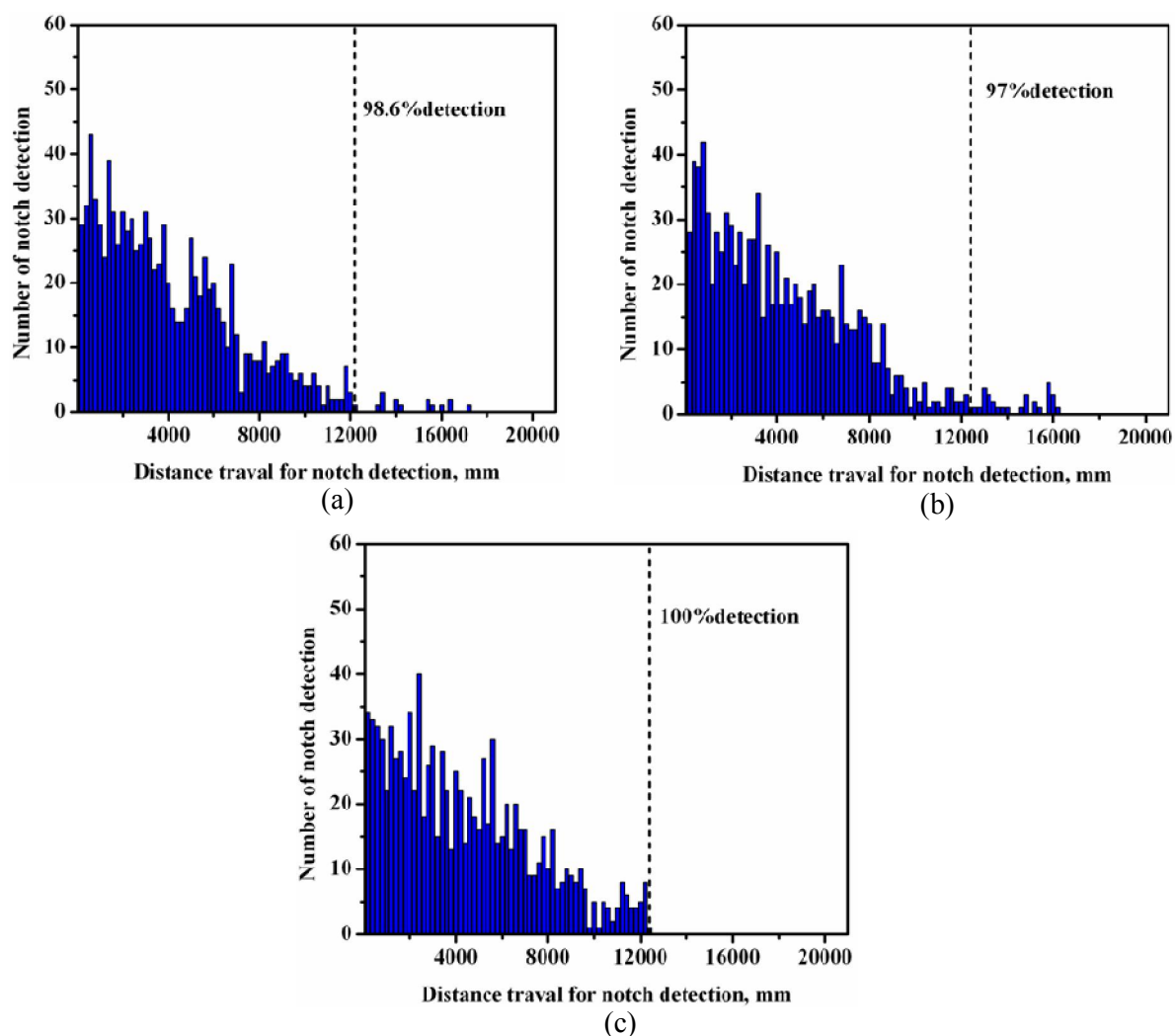


Figure 6.18: Bar plot for distance travelled to detect the notch at a step size of (a) 5.0 mm (b) 7.0 mm (c) 10.0 mm for the billiard scan plan.

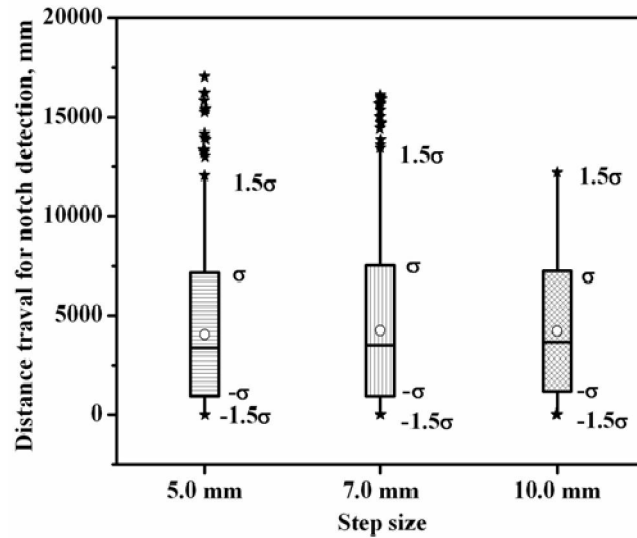


Figure 6.19: The box plot for distance travelled to detect the notch at different step sizes by the billiard scan plan.

6.7 Experimental verification of the Billiard scan plan

In order to check the performance of the scan plans, a series of experiments are carried out on two test specimens shown in Figure 6.9. The number of steps required to detect all the 13 notches (as given in Figure 6.9 (a)) for the first time is calculated for all the five scan plans. Figure 6.20 shows the box plot of steps required to detect all the 13 notches. From the figure it is clearly seen that for the billiard scan plan, distribution of number of steps required to detect the notches is near to the mean, due to the small value of σ (38.6) as compared to the raster, diagonal raster, spiral and Lissajous (128.5, 126.1, 126.8 and 52.1 respectively) scan plans. The details of number of steps required to detect the notches are shown in Table 6.4. From the result, it is clear that the number of steps required to detect the notches depends on the notch location for all the five scan plans. However, billiard scan plan performed faster as compared to other scan plans. It takes a maximum of 122 steps to detect all the 13 notches present in the SS plate. A very good agreement is seen between the numerical and experimental results.

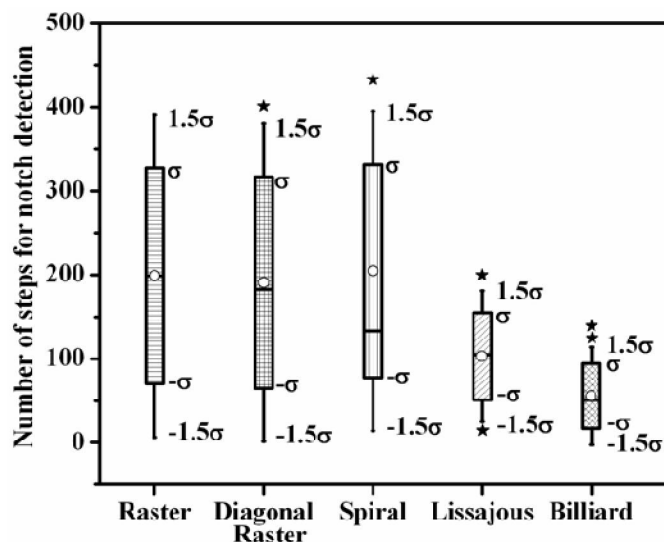


Figure 6.20: Number of steps required to detects all the 13 notches by different scan plans.

Table 6.4: Number of steps required for first time detection of all the 13 notches.

Notch	Raster	Diagonal Raster	Spiral	Lissajous	Billiard
D1	23	171	97	170	65
D2	191	324	107	101	21
D3	359	401	115	15	116
D4	111	177	329	105	58
D5	279	330	339	78	28
D6	31	51	89	109	77
D7	199	183	433	74	122
D8	367	336	125	127	34
D9	119	57	321	70	9
D10	287	188	349	200	98
D11	39	7	81	26	3
D12	207	62	143	121	51
D13	375	194	133	142	43

EC imaging is performed for notch D14 of Figure 6.9 (b) using billiard scan plan and the resulting amplitude image is shown in Figure 6.21. A very good SNR of 10 dB has been achieved with this scan plan.

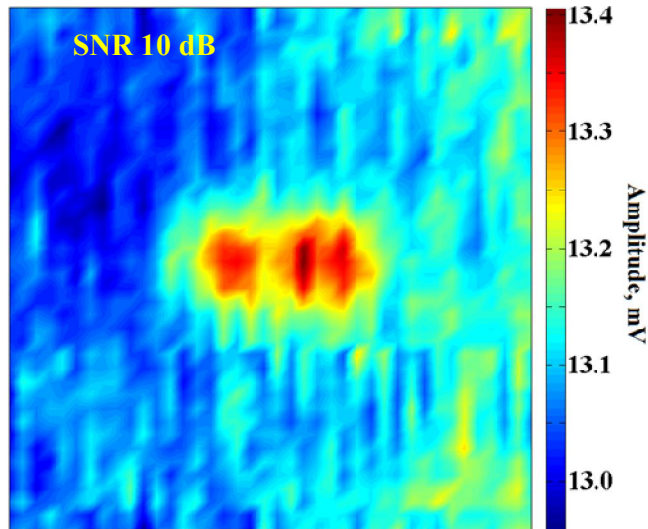


Figure 6.21: Amplitude image of notch D14 resulted by billiard scan plan.

These numerical and experimental results clearly reveal that the billiard scan plan is better for rapid detection and imaging of flaws in metallic plates. This superior performance of the billiard scan plan is achieved because of fast coverage of entire surface area due to the random movement of ECT probe along the diagonal lines and compatibility with different scan step sizes.

6.8 Summary

Raster, diagonal raster, spiral, Lissajous, and billiard scan plans have been critically analyzed in ECT for rapid detection and imaging of flaws and their comparative performance has been studied, for the first time, based on rapidness, area coverage and step size for detection of 1000 random located notches in a stainless steel plate. The following are the major observations:

- Numerical investigations have revealed that the billiard scan plan showed superior performance as compared to the other scan plans. The Billiard scan plan detected 98.5% notches in a saturation point of 2400 number of steps while other scan plans detected only around 50.0 % notches for the same number of steps.

- Studies revealed that 35° is optimum angle of incidence for the billiard scan plan for rapid detection of notches in a square region of imaging. The billiard scan plan performance did not degrade when the step size was doubled to 10.0 mm.
- The study establishes, for the first time, that the billiard scan plan is an alternate scan plan to raster scan for rapid and reliable inspection of large surfaces of electrically conducting materials by ECT.
- The performance of the billiard scan plan has also been experimentally verified on a 5.0 mm thick stainless steel plate having a notch. The EC image obtained by billiard scan plan was found to have an SNR of 10 dB.
- The study proposes the use of billiard scan plan for rapid and reliable inspection of large surfaces of electrically conducting material surfaces during ECT either during quality assurance or in-service inspection.

Conclusion and Future works

7.1 Conclusion

The thesis has focused on the development of eddy current methodologies for rapid and reliable detection and imaging of sub-surface flaws in metallic materials. The thesis has extensively demonstrated the possible methodologies for detection of sub-surface flaws in austenitic stainless steel.

Developmental studies on the enhancement of sub-surface flaws detection have been carried out to overcome the limitation of the conventional ECT. The conventional ECT is, in general, confined to detection of sub-surface flaws within 5.0 mm depth in stainless steel plates. Detection of flaws in thicker plate in range of 8.0 mm to 12.0 mm, such as storage tanks in nuclear reprocessing plants made by the 304L austenitic stainless steel is essential. Hence, for reliable and rapid detection and imaging of sub-surface flaws in 12.0 mm thick austenitic stainless steel, the thesis has proposed for the first time four effective eddy current methodologies. These methodologies include development of a high throughput probe, a high sensitive instrument, a novel fusion methodology and rapid imaging scan plan. The major conclusions of the thesis and future work are given below.

- Finite element modelling studies have been carried out using COMSOL multi-physics software for selection of optimum coil probe configuration among send-receive type air core, ferrite core, ferrite core with outer shielding and cup-core probes. The performance of these four types of probe has been analysed based on predicted parameters viz., magnetic flux density (indicative of low reluctance path), eddy current density (indicative of flux concentration at flaw location) and change in phase angle (indicative of detection sensitivity in depth direction). Model predictions reveal that cup-core probe produces higher magnetic flux density, eddy current density and

change in phase angle for flaws located at more than 5.0 mm below the surface as compared to other probe configurations. Model prediction and experimental studies confirm that the optimum diameter and excitation frequency are 22.0 mm and 5 kHz for detection of sub-surface flaw in 12.0 mm thick austenitic stainless steel plates.

- A high sensitive eddy current instrument consisting of a high current sinusoidal driving unit and a digital lock-in amplifier based precise measurement unit has been designed and developed. The digital lock-in amplifier is capable of precisely measuring the phase lag (sensitivity, 0.001 degree) of the sinusoid from flaw regions using I/Q detection technique which is implemented using LabVIEW software. Systematic studies using this instrument revealed a definite improvement in the detection sensitivity with increase in excitation current and by use of precise phase angle measurement. For AISI 304L stainless steel plate of thickness 12.0 mm, an increase in phase angle is observed with increase in the excitation current up to 550 mA and ensured reliable detection of a sub-surface notch located 8.0 mm below the surface.
- From the experimental results it is also observed that, the cup-core probe and instrument produce a linear relationship between the flaw location below the surface and change in phase angle. This linear relationship facilitates improvement in detection and sizing of deep sub-surface flaws with better resolution in depth direction. It is found that the instrument and cup-core type send-receive probe enable identification of surface and sub-surface flaws because the change in sign of the phase angle signals.
- A novel BayWT based image fusion methodology is proposed to further enhance the capability of the instrument and optimised probe to image sub-surface flaws. BayWT based image fusion is an integrated fusion methodology of wavelet transform and Bayesian fusion method. BayWT based fusion method has shown significant improvement in SNR as compared to the other fusion method viz. Laplacian pyramid, wavelet transformed, principal component analysis and Bayesian method. BayWT based fusion method achieved an SNR of 17.63 dB, which is three

times the SNR of the input images (5.36 dB) and a 7.0 dB more than achieved by other fusion methods (10.0 dB).

- For automated ECT of large size austenitic stainless steel components in radioactive environment, different type of scan plans such as raster, diagonal raster, spiral, Lissajous and billiard have been studied, for the first time. The comparative performance has been studied based on rapidness, area coverage and variable step size metrics for selection of rapid scan plan, after scanning of 1000 random located notch in a stainless steel plate. The billiard scan plan has been found to be 2 times faster than that of the other scan plans and showed superior performance as compared to other scan plans. Studies revealed that 35 degree is optimum angle of incidence for the billiard scan plan for rapid detection of notches. The performance of the billiard scan plan did not degrade when the step size was doubled to 10.0 mm. Thus, the study establishes, for the first time, that the billiard scan plan is an alternate scan plan to the traditional raster scan for rapid and reliable detection and imaging of large surface of electrically conducting materials by eddy current testing.

7.1.1 Technical and scientific contributions

The major contributions of this thesis for detection of sub-surface flaws in metallic materials are the following:

- A high throughput send-receive type cup-core coil probe has been designed and developed for ensuring deeper penetration of eddy currents into the material. This probe has shown higher sensitivity for surface as well sub-surface flaws in 12.0 mm thick austenitic stainless steel plates.
- An eddy current instrument capable for generation of high excitation current and precisely measuring the phase using a digital lock-in amplifier implemented in LabVIEW software has

been designed and developed. This instrument can be used for detection of sub-surface flaws as well as surface flaws in any metallic material.

- For enhancement of the eddy current images of sub-surface flaws, a novel BayWT image fusion methodology has been developed combining the capabilities of wavelet transform and Bayesian method. This fusion method has resulted in a very high SNR of 17.63 dB. This methodology can be readily extended to ultrasonic, radiography and thermography images for enhanced detection of flaws and for their accurate sizing.
- For reduction of radiation dose to the inspection personnel, billiard scan plan has been proposed for the first time as a rapid scan plan for eddy current imaging of flaws. The proposed scan plan is expected to change the way ECT imaging is carried out in future.
- The methodologies developed in the thesis are expected to ensure faster eddy current imaging inspection of storage tanks of reprocessing plants of FBR.

7.2 Future works

The works presented in this thesis has significantly improved the capability for detection of deep sub-surface flaws in thick stainless steel components. In this thesis, high sensitive eddy current instrument, high throughput send-receive type cup-core coil probe and BayWT based fusion have been developed and they demonstrated better detection sensitivity for sub-surface flaws located 8.0 mm below the surface. Embedded flaws are not considered in the present study. It may be worth exploring the instrument and probe developed for detection of corrosion in second and third layer of aircraft structures.

In the FE model, relative permeability μ_r is assumed to be constant for ferrite core and shielding as the excitation frequency are < 100 kHz. However at higher frequency, it is essential to consider non-linear magnetisation components in the model for obtaining accurate results.

In the present study, flaw depth and location are considered for selection of the probe configuration. However, more information can be obtained by detailed modelling studies at varying surface conditions, probe tilt and varying lift-off, towards fine tuning the instrument and probe performance and to explore other possible signal and image processing methods.

For optimisation of the probe configuration, a 2D-axi-symmetric model is used. These model predictions are sufficient to optimise probe and frequency, does not consider the flaw orientation. For this purpose and also to model other 3-dimensional situations such as non-uniform electromagnetic coupling three dimensional (3D) model investigation is essential.

In this thesis, an optimum probe diameter has been found as 22.0 mm for AISI 304L stainless steel plate of thickness 12.0 mm. For other thicknesses, optimum diameter and excitation frequency will change. Hence, it may be beneficial to investigate further and establish a relationship among probe diameter, frequency and thickness for better applicability of the cup-core type send-receive probe for various applications and for generalisation purpose.

In this thesis, the synergistic combination of probe and instrument clearly ensured detection of inside corrosion damage upto 12.0 mm thick stainless steel storage tanks by scanning the probe on the outer surface. Further works may be interesting to use the instrument and probe to detect corrosion damage present in actual storage tanks or through accelerated corrosion studies. It will also be beneficial to evaluate the sensitivity of the instrument and probe for different object geometries and in different materials. Detection of flaws of length 30.0 mm has been studied in this thesis. It may be worth studying the instrument sensitivity and capability to detect shorter flaws.

In this study curvature surface of the vessels is analysed as plate due to the large diameter of the vessels (~10 m) curvature effect are ignored. It will be useful to test the probe on actual components and design suitable curved front face to minimize coupling issues.

For the envisaged detection of inside surface corrosion electromagnetic acoustic transducers (EMATs) probes, capable of performing both ultrasonic and eddy current testing, may be studied for detection of sub-surface flaws.

The optical images are usually sharp as the optical sources possess point delta function. While the eddy current images are blurred (oversized) as the probes are of finite size and have a point spread function that is circular and like a 2D-Gaussian function. When a fusion methodology is applied, more enhancements are likely for the optical images as compared to eddy current images. However, more detailed studies are required to compare and make a quantitative assessment.

Flaws orientation of 0 and 90 degree is used for evaluation of the rapid scan plans. Studies on detection of notches at different orientations are worth to check the performance of the billiard scan plan. This work can be extended by studying the performance of the scan plans using different types of probes such as absolute, differential etc towards identifying much better probe type and configuration for detection of flaws in thick material.

References

- [1] D. E. Bray and R. K. Stanley, *Non-destructive evaluation: a tool for design, manufacturing, and service.*: McGraw-Hill, 1989.
- [2] Charles J. Hellier, *Handbook of non-destructive evaluation.*: McGraw-Hill, 2013.
- [3] B. P. C. Rao, *Practical eddy current testing.* New Delhi: Narosa Publishing House, 2007.
- [4] Farhad Tovassoli, *Advances in stainless steel*, Baldev Raj, Ed.: Universities Press, 2010.
- [5] Baldev Raj, T. Jayakumar, and M. Thavasimuthu, *Practical non-destructive testing*, 3rd ed. New Delhi: Narosa Publishing House, 2007.
- [6] P. J. Shull, *Non-destructive evaluation: theory, techniques and applications.* New York: Marcel Dekkar Inc., 2002.
- [7] H. L. Libby, *Introduction to electromagnetic NDT methods.* New York: Wiley Interscience, 1971.
- [8] B. P. C. Rao, "Eddy Current Testing: Basics," *Journal of Non Destructive Testing & Evaluation*, vol. 10, pp. 7-16, 2011.
- [9] S. S. Udpa and Patrick O Moore, *Nondestructive Testing Handbook Third Edition. Volume 5 Electromagnetic.*: Testing, American Society of Nondestructive Testing, 2004.
- [10] N. Ida, *Numerical modeling for electromagnetic Non-destructive evaluation.*: Chapman and Hall, 1995.
- [11] Lalita Udpa, "Imaging of electromagnetic NDT phenomena," Colorado State University, Ph.D. dissertation 1986.
- [12] R. McCary, D. Oliver, K. Silverstein, and J. Young, "Eddy current imaging," *IEEE Transactions on Magnetics*, vol. 20, no. 5, pp. 1986-1988, 1984.
- [13] R. Joynson, R. McCary, D. Oliver, K. Silverstein-Hedengren, and L. Thumhart, "Eddy current imaging of surface-breaking structures," *IEEE Transactions on Magnetics*, vol. 22, no. 5, pp. 1260-1262, 1986.
- [14] Baldev Raj, U. Kamachi Mudali, T. Jayakumar, K. V. Kashiviswanathan, and R. Natarajan, "Meeting the challenges related to material issues in chemical industries," *Sadhana*, vol. 25, no. 6, pp. 519-559, December 2000.
- [15] Baldev Raj and U. Kamachi Mudali, "Materials development and corrosion problems in nuclear fuel reprocessing plants," *Progress in Nuclear Energy*, vol. 48, no. 4, pp. 283-313, 2006.
- [16] C. V. Dodd and W. E. Deeds, "Analytical Solutions to Eddy-Current Probe-Coil Problems," *Journal of Applied Physics*, vol. 39, no. 6, pp. 2829-2838, May 1968.
- [17] Z. Mottl, "The quantitative relations between true and standard depth of penetration for air-cored probe coils in eddy current testing," *NDT International*, vol. 23, no. 1, pp. 11-18, 1990.

- [18] G. Mook, O. Hesse, and V. Uchanin, "Deep Penetrating Eddy Currents and Probes," *MP Materials Testing*, vol. 49, pp. 258-264, 2007.
- [19] (2001-2012) NDT Education Resource Center, The collaboration for NDT education. [Online]. <http://www.ndt-ed.org>
- [20] S. Thirunavukkarasu, B. P. C. Rao, T. Jayakumar, and Baldev Raj, "Techniques for processing remote field eddy current signals from bend regions of steam generator tubes of prototype fast breeder reactor," *Annals of Nuclear Energy*, vol. 38, pp. 817-824, 2011.
- [21] P. Xiang, S. Ramakrishnan, X. Cai, P. Ramuhalli, R. Polikar, S. S. Udpa, and L. Udpa, "Automated analysis of rotating probe multi-frequency eddy current data from steam generator tubes," *International Journal of Applied Electromagnetics and Mechanics*, vol. 12, pp. 151-164, 2000.
- [22] B. Sasi, Cacciola Matteo, C. Babu Rao, T. Jayakumar, and Baldev Raj, "Hybrid Signal Processing Approach for Enhanced Detection of Defects in EC-NDE," *Research in Nondestructive Evaluation*, vol. 24, pp. 51-61, 2013.
- [23] B. P. C. Rao, Baldev Raj, T. Jayakumar, and P. Kalyanasundaram, "An intelligent imaging scheme for automated eddy current testing," *Nondestructive Testing and Evaluation*, vol. 17, no. 1, pp. 41-57, 2001.
- [24] B. Sasi, Matteo Cacciola, Lalita Udpa, B. P. C. Rao, T. Jayakumar, and Baldev Raj, "Development of image fusion methodology using discrete wavelet transform for eddy current images," *NDT & E International*, vol. 51, pp. 51-57, 2012.
- [25] X. E. Gros, P. Strachan, D. W. Lowden, and I. Edwards, "NDT data fusion," in *in Proc. 6th Eur. Conf. Nondestructive Testing*, 1994, pp. 355-359.
- [26] R. Prachetaa and B. P. C. Rao, "Image Processing for NDT images," in *IEEE International Conference on Signal and Image Processing (ICSIP)*, 2010, pp. 169-174.
- [27] P. J. Burt and E.H. Adelson, "The Laplacian pyramid as a compact image code," *IEEE Transactions on Communications*, vol. 31, no. 4, pp. 432-540, 1983.
- [28] S. Shuaib Ahmed, "Machine learning based inversion studies in eddy current non-destructive evaluation," HBNI Mumbai, PhD dissertation 2014.
- [29] V.P.S. Naidu and J.R. Rao, "Pixel-level Image Fusion using Wavelets and Principal Component Analysis," *Defence Science Journal*, vol. 58, no. 3, pp. 338-352, 2008.
- [30] Patrick J. Van Fleet, *Discrete wavelet transformations: An elementary approach with applications.*: A John wiley & Sons, 2007.
- [31] Ali Mohammad-Djafari, "A Full Bayesian Approach for Inverse Problems," in *Maximum Entropy and Bayesian Methods*, KennethM. and Silver, RichardN. Hanson, Ed.: Springer Netherlands, 1996, pp. 135-144.
- [32] A. M. Djafari, "A Bayesian approach for data and image fusion," in *22nd International Workshop on Bayesian Inference and Maximum Entropy Methods in Science and Engineering. AIP Conference Proceedings*, vol. 659, 2003, pp. 386-408.
- [33] S. Thirunavukkarasu, B. P. C. Rao, Anil Kumar Soni, S. Shuaib Ahmed, and T. Jayakumar, "Comparative performance of image fusion methodologies in eddy current testing,"

Research Journal of Applied Sciences, Engineering and Technology, vol. 4, no. 24, pp. 5548-5551, 2012.

- [34] A. Lopes Ribeiro and H. Geirinhas Ramos, "Inductive probe for flaw detection in non-magnetic metallic plates using eddy currents," , vol. 12, 2008, pp. 1447-1451.
- [35] D. G. Park, C. S. Angani, G. D. Kim, C. G. Kim, and Y. M. Cheong, "Evaluation of Pulsed Eddy Current Response and Detection of the Thickness Variation in the Stainless Steel," *IEEE Transactions on Magnetics*, vol. 45, no. 10, pp. 3893-3896, 2009.
- [36] Y. He, F. Luo, M. Pan, X. Hu, J. Gao, and Bo. Liu, "Defect Classification based on rectangular pulsed eddy current sensor in different directions," *Sensors and Actuators A: Physical*, vol. 157, no. 1, pp. 26-31, 2010.
- [37] D. Roy, R. Chakroborty, and B. K. Kaushik, "Comparative study of E-shaped coil and evolution of new methodology for crack detection using eddy current testing," *Insight- Non-Destructive Testing and Condition Monitoring*, vol. 55, no. 10, pp. 553-557, 2013.
- [38] Eric Vourc'h, Pierre-Yves Joubert, Guillaume Le Gac, and Pascal Iarzal, "Nondestructive evaluation of loose assemblies using multi-frequency eddy currents and artificial neural networks," *Measurement Science and Technology*, vol. 24, p. 125604, 2013.
- [39] D. Placko and I. Dufour, "A focused-field eddy current sensor for nondestructive testing," *IEEE Transactions on Magnetics*, vol. 29, no. 6, pp. 3192-3194, 1993.
- [40] K Arunachalam, L. Udpa, and S. Udpa, "Statistical analysis of array probe eddy current data from steam generator tubes," *Studies in Applied Electromagnetics and Mechanics*, vol. 36, pp. 159-166, 2012.
- [41] J. Xin, L. Udpa, S. Udpa, R. Grimberg, and A Savin, "Rotating field eddy current probe for cylindrical samples," *Studies in Applied Electromagnetics and Mechanics*, vol. 39, pp. 60-74, 2014.
- [42] P. Palanisamy and K. M. Lakin, "Development of EC inspection technique for sleeved engine disk bolt holes," *Review of Progress in Quantitative Non-destructive Evaluation*, vol. 2A, pp. 205-223, 1983.
- [43] H. Hoshikawa, R. M. Li, and N. Ida, "Finite element analysis of eddy current surface probes," *Review of Progress in Quantitative Nondestructive Evaluation*, vol. 3A, pp. 675-682, 1984.
- [44] Shin Young, Kil Choi, and Dong Myung, "Design of a Shielded Reflection Type Pulsed Eddy Current Probe for the Evaluation of Thickness," *Journal of the Korean Society for Nondestructive Testing*, vol. 27, no. 5, pp. 398-408, 2007.
- [45] B. Sasi, B. P. C. Rao, S. Thirunavukkarasu, T. Jayakumar, and Baldev Raj, "Eddy Current-Giant Magneto-Resistive (GMR) Sensor for Nondestructive Detection of Deep-surface Defects," in *Conference Proc. of 12th National seminar on Physics and Technology of Sensors*, vol. 1, 2007.
- [46] C. S. Angani, D. G. Park, C. G. Kim, P. Leela, M. Kishore, and Y. M. Cheong, "Pulsed eddy current differential probe to detect the defects in a stainless steel pipe," *Journal of Applied Physics*, vol. 109, no. 7, p. 07D348, 2011.

- [47] C. Claeys and E. Simon, *Radiation effects in advanced semiconductor materials and devices.*: Springer Series in Material Science, 2002.
- [48] T. P. Theodoulidis, "Model of ferrite-cored probes for eddy current nondestructive evaluation," *Journal of applied physics*, vol. 91, no. 53, pp. 3071-3078, 2003.
- [49] M. Cacciola, G. Megali, D. Pellicanuo, S. Calcagno, M. Versaci, and F. C. Morabito, "Modelling and Validating Ferrite-core Probes for GMR-eddy Current Testing in Metallic Plates," *PIERS online*, vol. 6, no. 3, pp. 237-241, 2010.
- [50] Z. Zeng, Lalita Udpa, and S. S. Udpa, "Finite-Element Model for simulation of ferrite-core eddy-current probe," *IEEE Transactions on Magnetics*, vol. 46, no. 3, pp. 905-909, 2010.
- [51] S.N. Vernon and T.A.O. Gross, "Effects of Shielding on Properties of Eddy Current Probes with Ferrite Cup Cores," in *Review of Progress in Quantitative Nondestructive Evaluation*, Donald O. Thompson and Dale E. Chimenti, Eds.: Springer US, 1987, vol. 6 A, pp. 713-719. [Online]. http://dx.doi.org/10.1007/978-1-4613-1893-4_80
- [52] P. Y. Joubert, E. Vourc'h, Tassin, A. Diraison, and Y. Le, "Source separation techniques applied to the detection of subsurface defects in the eddy current NDT of aeronautical lap-joints," *NDT & E International*, vol. 43, no. 7, pp. 606-614, 2010. [Online]. <http://www.sciencedirect.com/science/article/pii/S096386951000071X>
- [53] A. J. Bahl and D. W. Cooley, "Analysis and Design of Eddy-Current Measurement Systems," *Review of Progress in Quantitative Nondestructive Evaluation*, vol. 2A, pp. 225-244, 1983.
- [54] T. E. Capobianco and F. R. Fickett, "Precision Measurement of Eddy Current Coil Parameters," *Review of Progress in Quantitative Nondestructive Evaluation*, vol. 4A, pp. 491-498, 1985.
- [55] J. Blitz, "Nondestructive testing using electromagnetic instrumentation," *Journal of Physics E: Scientific Instruments*, vol. 16, p. 1135, 1983.
- [56] Dario Pasadas, T. Jorge Rocha, Helena Geirinhas Ramos, and A. Lopes Ribeiro, "Evaluation of portable ECT instruments with positioning capability," *Measurement*, vol. 45, pp. 393-404, 2012.
- [57] Wang Chao, Zhi Ya, and Gao Peng, "GMR based eddy current system for defect detection," in *Proceedings of the 11th IEEE International Conference on Electronic Measurement & Instruments*, 2013.
- [58] Naveen V. Nair, Vikram R. Melapudi, Hector R. Jimenez, Xin Liu, Yiming Deng, Zhiwei Zeng, Lalita Udpa, Thomas J. Moran, and S. S. Udpa, "A GMR-Based Eddy Current System for NDE of Aircraft Structures," *IEEE Transactions on Magnetics*, vol. 42, no. 10, pp. 3312-3314, 2006.
- [59] P. Clarkson, T. J. Esward, P. M. Harris, A. A. Smith, and I. M. Smith, "Software simulation of a lock-in amplifier with application to the evaluation of uncertainties in real measuring systems," *Measurement Science and Technology*, vol. 21, pp. 45106-45116, 2010.
- [60] P. G. Doctor, T. P. Harington, T. J. Davis, C. J. Morris, and D. W. Farley, *Pattern recognition methods for classifying and sizing flaws using eddy current data*, G. Birnbaum and G. Free, Eds.: ASTM STP- 722, 1981.

- [61] S. S. Udpa and W. Lord, "Fourier descriptors classification scheme for differential probe signal," *Material evaluation*, vol. 42, pp. 1136-1141, 1984.
- [62] M. T. Shyamsunder, C. Rajgopalan, Baldev Raj, S. K. Dewangan, B. P. C. Rao, and K. K. Ray, "Pattern recognition approaches for detection and characterization of defects by eddy current testing," *Materials Evaluation*, vol. 51, no. 1, pp. 93-101, 2000.
- [63] P. Kalyanasundaram, S. Thirunavukkarasu, B. P. C. Rao, T. Jayakumar, and Baldev Raj, "Eigen value based approach for enhancement of eddy current images," *Research in Non-destructive Evaluation Journal (Elsevier)*, vol. 18, no. 1, pp. 13-22, 2007.
- [64] T. Chady and P. Lopato, "Flaws Identification Using an Approximation Function and Artificial Neural Networks," *IEEE Transactions on Magnetics*, vol. 43, no. 4, pp. 1769-1772, 2007.
- [65] M. Cacciola, A. Gasparics, F. C. Morabito, M. Versaci, and V. Barrile, "Advances in Signal Processing to Reduce Lift-off Noise in Eddy Current Tests," *PIERS online*, vol. 3, no. 4, pp. 517-521, 2007.
- [66] M. Mina, J. Yim, S. S. Udpa, and Lalita Udpa, "Two dimensional multi-frequency eddy current data fusion," *Review of Progress in QNDE*, vol. 15, pp. 2125-2132, 1996.
- [67] M. Mina, S. S. Udpa, Lalita Udpa, and J. Yim, "A new approach for practical two dimensional data fusion utilizing a single eddy current probe," *Review of Progress in QNDE*, vol. 16D, pp. 749-755, 1997.
- [68] X. E. Gros, Zheng Liu, K. Tsukada, and K. Hanasaki, "Experimenting with Pixel-Level NDT Data Fusion Techniques," *IEEE TRANSACTIONS ON INSTRUMENTATION AND MEASUREMENT*, vol. 49, no. 5, pp. 1083-1090, 2000.
- [69] Zheng Liu, D. S. Forsyth, J. P. Komorowski, K. Hanasaki, and T. Kirubarajan, "Survey: State of the Art in NDE Data Fusion Techniques," *Instrumentation and Measurement, IEEE Transactions on*, vol. 56, no. 6, pp. 2435-2451, 2007.
- [70] Ayed Salman M. Algarni, "Image Fusion Based Enhancement of Electromagnetic Nondestructive Evaluation," King Saud University, PhD Dissertation 2009.
- [71] Lalita Udpa, S.S. Udpa, and A. Tamburrino, "System and Model-Based Approaches to Data Fusion for NDE Applications," in *Multi-Sensor Image Fusion and Its Applications*, Rick S. Blum and Zheng Liu Eds, Eds.: CRC Press Taylor & Francis, 2006, ch. 12, pp. 347-373.
- [72] X. E. Gros, *NDT Data Fusion*. New York: Halsted Press, 1996.
- [73] A. K. Jain, M. P. Dubuisson, and M. S. Madhukar, "Multi-sensor fusion for nondestructive inspection of fiber reinforced composite materials," in *in Proc. 6th Tech. Conf. Amer. Soc. Composites*, 1991, pp. 941-950.
- [74] Z. Liu, F. Abbas, and M. Nezh, "Application of Dempster-Shafer Theory for Fusion of Lap Joints Inspection Data," in *Proceedings of SPIE, the International Society for Optical Engineering*, vol. 6176, 2006, pp. 6176J-6176J.9.
- [75] O. Dupuis, V. Kaftandjian, D. Babot, and Y. Zhu, "Automatic detection and characterization of weld defects: Determination of confidence levels for data fusion of radiosopic and ultrasonic images," *Insight- Non-Destructive Testing and Condition Monitoring*, vol. 41,

no. 3, pp. 170–172, 1999.

- [76] Patricia Cotic, Zvonko Jaglicic, Ernst Niederleithinger, Markus Stoppel, and Vlatko Bosiljkov, "Image Fusion for Improved Detection of Near-Surface Defects in NDT-CE Using Unsupervised Clustering Methods," *Journal of Nondestructive Evaluation*, vol. 33, no. 3, pp. 384-397, 2014.
- [77] A. Habibalahi and M. S. Safizadeh, "Pulsed eddy current and ultrasonic data fusion applied to stress measurement," *Measurement Science Technology*, vol. 25, p. 055601, 2014.
- [78] B. P. C. Rao, T. Jayakumar, S. Thirunavukkarasu, W. Sharatchandra Singh, G.K. Sharma, Anish Kumar, and C. Babu Rao, "Effective Nondestructive Imaging of Defects in Engineering Components," in *18th World Conference on Nondestructive Testing*, South Africa, 2012.
- [79] G. Mook, Fritz Michel, and Jouri Simonin, "Electromagnetic Imaging Using Probe Arrays," *Journal of Mechanical Engineering*, vol. 57, no. 3, pp. 227-236, 2011.
- [80] Jean-François Bureau, Robert C. Ward, and Alexandre Julien, "Application of Eddy Current Array Technology to Surface Inspection," in *18th World Conference on Nondestructive Testing*, Durban, South Africa, 2012.
- [81] S. Yeom, A. Stern, and B. Javidi, "Compression of 3D color integral images," *Optical Express*, vol. 12, pp. 1632-1642, 2004.
- [82] Attila, "Scanning strategies for imaging arrays," , vol. 7020, France, 2008.
- [83] A. Bazaie, Yuen K. Yong, and S. O. Reza Moheimani, "High-speed Lissajous-scan atomic force microscopy: Scan pattern planning and control design issues," *Review of Scientific Instruments*, vol. 83, p. 063701, 2012.
- [84] Meng Joo Er, Weilong Chen, and Shiqian, "High-speed face recognition based on discrete cosine transform and RBF neural networks," *IEEE Transactions on Neural Networks*, vol. 16, no. 3, pp. 679-691, 2005.
- [85] B. P. C. Rao, "An intelligent imaging scheme for automated eddy current testing of austenitic stainless steel plates and welds," Saarland University, Saarbruecken, Ph.D. dissertation 2000.
- [86] J. Jin, *The finite element method in electromagnetic*. New York: John Wiley & Sons, Inc. Publication, 2002.
- [87] M. V. K. Chari and S. J. Salon, *Numerical methods in electromagnetism.*: Academic Press, 2000.
- [88] W. Lord, "Applications of numerical field modeling to electromagnetic methods of nondestructive testing," *IEEE Transactions on Magnetics*, vol. 19, no. 6, pp. 2437-2442, 1983.
- [89] J. P. A. Bastos and N. Sadowski, *Electromagnetic modeling by finite element methods*. New York: Marcel Dekker, Inc. publisher, 2003.
- [90] Lalita Udpa, G. Katragadda, and W. Lord, "Finite element modeling and defect characterization for gas transmission pipelines," in *Proc. of 14th World Conference on Nondestructive Testing, India*, December 1996, pp. 269-274.

- [91] "COMSOL: Multiphysics modeling and simulation, <http://www.comsol.com>."
- [92] Y. Tian, Y. Li, Lalita Udpa, and S. S. Udpa, "Simulation of the world federation's second eddy current benchmark problem," *AIP Conference Proceedings*, vol. 657, no. 1, pp. 1816-1820, 2003.
- [93] C. Reboud, G. Pichenot, D. Premel, and R. Raillon, "Benchmark results: modeling with CIVA of 3D flaws responses in planar and cylindrical work pieces," *Review of progress in QNDE, AIP Conference Proceedings*, vol. 1096, pp. 1915-1921, 2009.
- [94] Hisamoto Moriguchi, Michael Wendt, and Jeffrey L. Duerk, "Applying the Uniform Resampling (URS) Algorithm to a Lissajous Trajectory," *Fast Image Reconstruction With Optimal Gridding Magnetic Resonance in Medicine*, vol. 44, pp. 766-781, 2000.

Appendix A: The measurement function algorithm

The measurement function algorithm described by Clarkson et al [58] for determining the magnitude (A) and phase (θ) is as follows.

1. Calculate:

$$m = f_s T, \quad (\text{A.1})$$

$$t_i = i/f_s, \quad i = 1, 2, \dots, m. \quad (\text{A.2})$$

where f_s is sampling frequency, T is duration of signal and t_i is sampled time.

2. Generate the test signal:

$$V_i^{test} = Q[A_{test} \sin(2\pi f_{test} \tilde{t} + \theta_{test}^r) + \delta V_i], \quad i = 1, 2, \dots, m. \quad (\text{A.3})$$

where V_i^{test} is test signal, Q denotes the operation of quantization (depending on the number of bits, N_b) applied to a sampled analogue signal, A_{test} is test signal amplitude, f_{test} is test signal frequency, θ_{test}^r is test signal phase, $\tilde{t} = t_i + \delta t_i$, δt_i is noise associated with sampled time value and δV_i is noise associated with amplitude value. The superscript ‘r’ notation is used here (and elsewhere) to denote an angle expressed in radians rather than degrees ($^\circ$).

3. Generate the orthogonal phase-shifted signals:

$$V_i^{X,ref} = Q[A_{ref} \sin(2\pi f_{ref} t_i + \theta_{ref}^r + \delta \theta_i^r)], \quad i = 1, 2, \dots, m. \quad (\text{A.4})$$

and

$$V_i^{Y,ref} = Q[A_{ref} \sin(2\pi f_{ref} t_i + \theta_{ref}^r + \delta \theta_i^r + \theta_{ort}^r)], \quad i = 1, 2, \dots, m. \quad (\text{A.5})$$

where A_{ref} is amplitude of reference signal, f_{ref} is frequency of reference signal, θ_{ref}^r is phase of reference $\delta \theta_{ort}^r$ reference signal orthogonality angle. The same number N_b of bits is used for the quantization of the (phase-shifted) reference signals as for the test signal.

4. Apply phase-sensitive detectors to the test signal and the (phase-shifted) reference signals to obtain product signals:

$$V_i^X = V_i^{test} V_i^{X,ref}, \quad i = 1, 2, \dots, m \quad (\text{A.6})$$

and

$$V_i^Y = V_i^{test} V_i^{Y,ref}, \quad i = 1, 2, \dots, m \quad (\text{A.7})$$

5. Apply a low-pass filter based on an RC filter with time constant τ to the product signals:

$$X_1 = \alpha V_1^X \quad (\text{A.8})$$

$$X_i = \alpha V_i^X + (1 - \alpha) X_{i-1}, \quad i = 2, \dots, m \quad (\text{A.9})$$

$$Y_1 = \alpha V_1^Y \quad (\text{A.10})$$

$$Y_i = \alpha V_i^Y + (1 - \alpha) Y_{i-1}, \quad i = 2, \dots, m \quad (\text{A.11})$$

where $\alpha = \Delta t / (\Delta t + \tau)$, $\Delta t = 1/f_s$

6. Evaluate the amplitude and phase difference:

$$A = \text{average} \left\{ \frac{2}{A_{ref}} \sqrt{X_i^2 + Y_i^2}, \quad i = n + 1, \dots, m \right\}, \quad (\text{A.12})$$

and

$$\theta = \text{average} \left\{ \tan^{-1} \left(\frac{Y_i}{X_i} \right), \quad i = n + 1, \dots, m \right\} \quad (\text{A.13})$$

where n is chosen so that $t_i \leq T - \tau$ for all $i \leq n$. Since the outputs of the low-pass filter require some time to stabilize, the estimates A and θ are calculated using a subset of the values corresponding to times after which saturation is expected to have occurred.